Dissertation

submitted to the

Combined Faculties of the Natural Sciences and Mathematics

of the Ruperto-Carola-University of Heidelberg, Germany

for the degree of
Doctor of Natural Sciences

Put forward by

Ioanna Arapoglou

born in: Athens, Greece
Oral examination: 25.07.2019

First measurement of the ground-state g-factor of boronlike argon $^{40}\mathrm{Ar}^{13+}$ in ALPHATRAP

Referees: Prof. Dr. Klaus Blaum

Prof. Dr. Selim Jochim

Abstract

In this thesis, the first high-precision measurement of the ground-state *g*-factor of a boronlike ion, $^{40}Ar^{13+}$, with a fractional uncertainty of 1.4×10^{-9}, is presented. The measurement has been performed on a single boronlike argon ion with the double Penning-trap setup of the newly developed ALPHATRAP experiment. Within this work, the trap tower of the experiment has been developed, assembled and tested prior to commissioning it together with the rest of the ALPHATRAP setup. The resulting measurement presented here corresponds to the most precise *g*-factor determination of a five-electron system to date. Not only does it allow testing the currently available theoretical predictions for the many-electron, QED and nuclear-recoil contributions, but also distinguishes between calculations that are in disagreement. The *g*-factor obtained here is in agreement with the most recent and most precise theoretical prediction, which has a relative uncertainty of 9×10^{-7}. This level of agreement constitutes one of the most accurate tests of many-electron QED contributions in strong fields. The sensitivity of this test will improve in the future with anticipated improvements on the theoretical *g*-factor, which includes higher-order QED contributions. Furthermore, this measurement paves the way towards the independent determination of the fine-structure constant with heavier highly charged ions in ALPHATRAP, where a specific difference of the boron- and hydrogenlike ions' *g*-factors will be used to cancel nuclear structure effects.

Zusammenfassung

In der vorliegenden Arbeit wird die erste Hochpräzisionsmessung des *g*-Faktors im Grundzustand eines borähnlichen Ions, $^{40}Ar^{13+}$, mit einer relativen Genauigkeit von 1.4×10^{-9} präsentiert. Die Messungen wurden an einem einzelnen borähnlichen Argonion in dem Doppel-Penningfallensystem des neu entwickelten ALPHATRAP-Experiments durchgeführt. Im Rahmen dieser Arbeit wurde der Fallenturm entwickelt, aufgebaut und getestet, bevor er gemeinsam mit dem Rest des ALPHATRAP Aufbaus in Betrieb genommen wurde. Dieses Ergebnis stellt die bis jetzt genaueste Bestimmung des *g*-Faktors eines Fünf-Elektronen-Systems dar. Die experimentellen Ergebnisse erlauben nicht nur aktuelle theoretische Vorhersagen von Vielelektronen-, QED- und Kernrückstoßbeiträgen zu testen, sondern auch die Unterscheidung zwischen Berechnungen die nicht miteinander übereinstimmen. Der hier erhaltene *g*-Faktor stimmt mit der neuesten und genauesten theoretischen Vorhersage mit einer relativen Genauigkeit von 9×10^{-7} überein. Dieser Grad an Übereinstimmung stellt einen der genauesten Tests von Vielelektronen-Beiträgen in starken Feldern dar. Die Empfindlichkeit dieses Tests wird sich in Zukunft mit erwarteten Verbesserungen des theoretischen *g*-Faktor, der QED-Beiträge höherer Ordnung beinhalten wird, verbessern. Darüber hinaus bereitet diese Messung den Weg in Richtung einer unabhängigen Bestimmung der Feinstrukturkonstante mit schwereren hochgeladenen Ionen in ALPHATRAP, bei denen eine spezifische Differenz zwischen den *g*-Faktoren von bor- und wasserstoffähnlichen Ionen verwendet wird, um Effekte der Kernstruktur aufzuheben.

Contents

1 Introduction

The interactions of particles are described by means of the four fundamental forces, i.e. the electromagnetic, weak, strong, and the gravitational force. While the electromagnetic, weak and strong interactions are described within the Standard Model by quantum field theories, gravitation is described by the theory of general relativity. Efforts to treat it in a quantum mechanical framework have not been fruitful so far, mostly due to the lack of experimental confirmation of the currently existing theories.

Quantum electrodynamics (QED) is the theory of the interaction between charged particles and the electromagnetic field by the exchange of photons. Ever since the theory was developed, no significant discrepancies between the experimental and theoretical results have been observed. QED is termed as the most successful quantum field theory of the Standard Model because it can predict physical observables in all accessible electric field strength scales. The observables that are typically employed for testing QED are the Lamb shift of energy levels in the hydrogen atom, the hyperfine splitting and the g-factor, as those quantities can be both measured and predicted with high accuracy. The most suitable for preforming high-precision tests of QED in strong fields is the g-factor as it is less sensitive to nuclear properties, and thus can be calculated to high precision.

Even though the theory has been verified with astonishing precision in weak fields, most notably for the case of a free electron [1], the precision of tests in the presence of strong fields has been limited so far. Therefore, the high-field range is marked as an unexplored territory for high-precision tests of QED, which could potentially lead to new physics beyond the Standard Model.

To this end, highly charged ions (HCI) are studied, where a bound electron is exposed to the extreme conditions of the binding field of a heavy nucleus, which leads to the strongest electric fields achievable in the laboratory of up to $10^{16}\,\mathrm{V/cm}$ for the $1s$ electron in hydrogenlike $^{208}\mathrm{Pb}^{81+}$. Due to the strong scaling of the transition frequencies, from ground to excited states, with the nuclear charge Z, most orbital transitions are no longer in the optical regime[1] for heavy HCI which limits the experimental and theoretical precision. A series of experiments have been performed with the experimental storage ring (ESR) at the GSI Helmholtz center of research, with heavy HCI up to hydrogenlike uranium [3]. There, the ground-state Lamb shift in hydrogenlike uranium has been measured with an accuracy of 1%, with the studied transitions being in the X-ray regime. The hyperfine splitting in the ground state of hydrogenlike holmium as a test of QED has been measured in an

[1] Bismuth constitutes one of the exceptions. The HFS in hydrogenlike and lithiumlike bismuth has been recently measured in the ESR storage ring [2].

electron beam ion trap (EBIT) [4] via spontaneous emission spectroscopy, as well as hydrogenlike rhenium and thallium [5, 6].

The goal of ALPHATRAP, which is a Penning-trap setup for high-precision g-factor determination, is to investigate the validity of the theory in the presence of strong electric fields where nonlinear effects (such as photon-photon interactions) might be present, by performing high-precision measurements with an intended relative uncertainty of 10^{-11} or better.

The ion's magnetic moment in terms of Bohr magnetons is related with its spin via the g-factor which can be predicted to very high precision within the Standard Model. Measuring this gyromagnetic proportionality constant g not only permits high-precision tests of bound-state QED (BS-QED) in the strong-field regime, but also allows the determination of fundamental constants, e.g. the electron mass [7, 8] and the fine-structure constant α [9, 10, 11]. With an appropriate choice of the element and charge state, different contributions to the theoretical prediction can be individually addressed.

Currently, the most stringent test of QED in strong fields has been performed using hydrogenlike silicon [12, 13] at the Mainz g-factor experiment. Measuring the isotope shift of the g-factor of lithiumlike calcium [14] gave access to the relativistic nuclear recoil effect, which represents a stringent test of BS-QED beyond the external-field approximation in strong fields [15]. Finally, relativistic many-electron contributions to the g-factor of the $1s^2 2s$ state and the interplay of QED and interelectronic interaction effects have been investigated using lithiumlike silicon [16, 17].

The experimental determination of the g-factor of a boronlike ion allows for high-precision tests of BS-QED for the $1s^2 2s^2 2p_{1/2}$ state (with the subscript 1/2 denoting the total angular momentum of the $2p$ valence electron) where the bound electron has a non-vanishing orbital angular momentum. Also, it permits scrutinising more sophisticated many-electron corrections to the g-factor. Additionally, the g-factor of heavy boronlike ions can be used for an independent determination of the fine-structure constant. For this, instead of a comparison between absolute g-factor values, which would be unfavourable due to the uncertainty of the nuclear structure contributions, one may compare specific g-factor differences between hydrogen- and boronlike ions [9, 10] of the same element. Thus, nuclear contributions can be isolated and cancelled, leading to an improved theoretical prediction which can be used for an independent determination of α, being competitive in precision to the presently best literature value [18]. In this determination, the extracted value of α will largely depend on the theoretical calculations. Therefore, it is of utmost importance that the theory is tested in a broad range of atomic numbers. For the presented work a boronlike argon ion has been used, which belongs to the low-/medium-Z regime. This system enables testing the methods to calculate electron-electron interaction effects more rigorously than in heavy ions, where

the strong central nuclear Coulomb field and the large QED effects suppress the importance of electron-correlation effects.

ALPHATRAP is a follow-up experiment to the Mainz *g*-factor experiment on HCI. This experiment was limited due to its in-trap ion production to low- and medium-Z ions up to lithiumlike calcium. A significant advantage of ALPHATRAP is the access to externally produced ions. Coupling the high-precision experimental setup to independent ion sources such as the Heidelberg EBIT will allow extending the experiment to the range of extremely strong electric fields of high-Z HCI up to $^{208}Pb^{81+}$.

During the course of this thesis, the ALPHATRAP group has successfully constructed, assembled and commissioned the full experimental setup located at the Max Planck Institute for Nuclear Physics in Heidelberg. The main focus of the present work has been the development of ALPHATRAP's Penning-traps. That involved the physical construction, assembly and testing of the traps, followed by developing the control system and commissioning of the trap tower. Finally, the first measurement campaign of the experiment was performed, which was dedicated to the ground-state *g*-factor of boronlike argon $^{40}Ar^{13+}$. Besides the confirmation of the successful implementation of the ALPHATRAP apparatus, this measurement corresponds to the most precise *g*-factor measurement of a five-electron system. Moreover, the obtained result distinguishes between different theoretical predictions currently in the literature, which show a discrepancy in the order of 85σ, and paves the way towards the independent determination of α with heavy HCI in ALPHATRAP.

The next chapter of this thesis, chapter 2, is dedicated to a brief introduction of the theoretical *g*-factor predictions, mainly focusing on the different contributions of the *g*-factor of $^{40}Ar^{13+}$. In chapter 3 the working principles of the Penning trap are introduced. In chapter 4, the ion detection is discussed as well as the techniques employed within this thesis for frequency measurements. The last section of this chapter is introducing the magnetic-moment dynamics and the adiabatic rapid passage technique, that has been implemented for the fist time in this kind of a Penning-trap setup. The experimental setup is discussed in chapter 5, with the main focus on the double-trap setup. In chapter 6 the preparatory measurements, which are essential for preforming a *g*-factor experiment, are presented. The *g*-factor measurement of $^{40}Ar^{13+}$ is presented in chapter 7, including the measurement procedure, the final experimental result along with the analysis of the corresponding statistical and systematic uncertainties, and the comparison between the experimental and the theoretical result. The final chapter of this thesis, chapter 8, briefly summarises the presented work and gives an outlook into the fascinating future prospectives of this unique experiment.

Theoretical g-factor

2

Quantum electrodynamics (QED) is considered to be the most successful of the quantum field theories within the Standard Model. In order to test the validity of the theory, different observables of various systems can be experimentally determined and compared to their corresponding predicted value. One of those observables is the g-factor, which is the subject matter of this thesis.

The theoretical calculation of the g-factor is addressed in this chapter starting with the free-electron g-factor in section 2.1. Afterwards, the bound-state g-factor is introduced in section 2.2 followed by the g-factor of boronlike ions. Finally, the basic principle of the experimental determination of the g-factor is discussed in section 2.4.

2.1 Free-electron g-factor

The gyromagnetic proportionality constant g relates the electron's magnetic moment to its spin in the following way:

$$\vec{\mu} = -g_\mathrm{s}\mu_\mathrm{B}\frac{\vec{S}}{\hbar}, \tag{2.1}$$

where g_s is the g-factor, $\mu_\mathrm{B} = e\hbar/2m_\mathrm{e}$ is the Bohr magneton, e is the elementary charge, m_e is the electron mass, $\vec{S}$ is the spin and $\hbar = h/2\pi$ is the Planck constant. Because the g-factor describes the magnetic moment of an electron in an external magnetic field, it serves as one of the observables in quantum physics together with the hyperfine splitting and the Lamb shift. Those observables can be both measured and predicted within QED to high precision. Therefore, by carrying out a high-precision measurement of the g-factor and comparing it to the predicted value, a test of the validity of QED, and consequently the Standard Model, is performed.

Dirac's relativistic quantum theory [19] predicts a value of $g = 2$ for a free electron. However, the experimentally determined free-electron g-factor demonstrated a deviation from the expected value of 2. This discovery, which was termed as the anomalous magnetic moment, together with the observation of the Lamb shift formed the basis of the modern QED development. The QED contributions to the g-factor are expressed as a power series in terms of α/π:

$$g - 2 = \sum_{n=1}^{\infty} C_{2n}\left(\frac{\alpha}{\pi}\right)^n, \tag{2.2}$$

where $\alpha = \frac{e^2}{4\pi\varepsilon_0\hbar c} \approx \frac{1}{137}$ is the fine-structure constant with e being the elementary charge, ε_0 the vacuum permittivity and c the speed of light. The leading order contribution shown in Fig. 2.1, the so-called Schwinger term, yielding $C_2 = 1$ [20]

describes the self-energy interaction of the electron with the electromagnetic field via emission and reabsorption of a virtual photon.

To date, the coefficients up to C_{10}, i.e. five-loop terms, which corresponds to 12672 Feynman diagrams, have been calculated [21, 22]. The theoretical calculation depends on the value of α and its precision is limited by the uncertainty of the independent experimental determination of the fine-structure constant. Inserting the independently determined α using caesium atoms [18] into the series expansion and comparing the calculated with the measured value of $g-2$ [1] allowed for a high-precision test of QED.

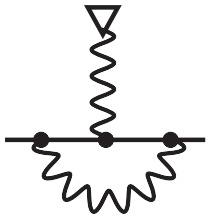

Fig. 2.1: Feynman diagram for the Schwinger correction for the free electron. The free electron and the photon are depicted by a straight and a curly line, respectively. The magnetic field is shown with a triangle. Before the electron interacts with the external magnetic field, it emits a virtual photon, which it reabsorbs later in order to conserve total energy.

2.2 Bound-electron g-factor

Even though QED has been tested to high precision in the case of a free particle, the validity of the theory has not been verified in the strong-field regime where non-linear effects might be of importance. In order to introduce the required strong fields we use highly charged ions (HCI), where the electron is exposed to the strong binding potential of the nucleus. For heavy HCI the electric field strength is in the order of $10^{16}\,\mathrm{V/cm}$, as can be seen in Fig. 2.2.

Since the electron is no longer a free particle but bound to a nucleus, it is described by the hydrogenic wave functions instead of the plane-wave solution to the Dirac equation. As a result, the g-factor of the bound electron is altered with respect to the free-electron case. The lowest-order relativistic correction to the 1s-state g-factor in α has been calculated by Breit [23]:

$$g_{1\mathrm{s}} = \frac{2}{3}\left(1+2\sqrt{1-(\alpha Z)^2}\right), \tag{2.3}$$

where for heavy ions with $\alpha Z \approx 1$ the α-dependence becomes significant, a fact that could be exploited for an independent determination of the fine-structure constant. Additionally, the QED contributions of a bound system differ from the free-electron case. The corresponding theory of bound-state QED (BS-QED) accounts for the

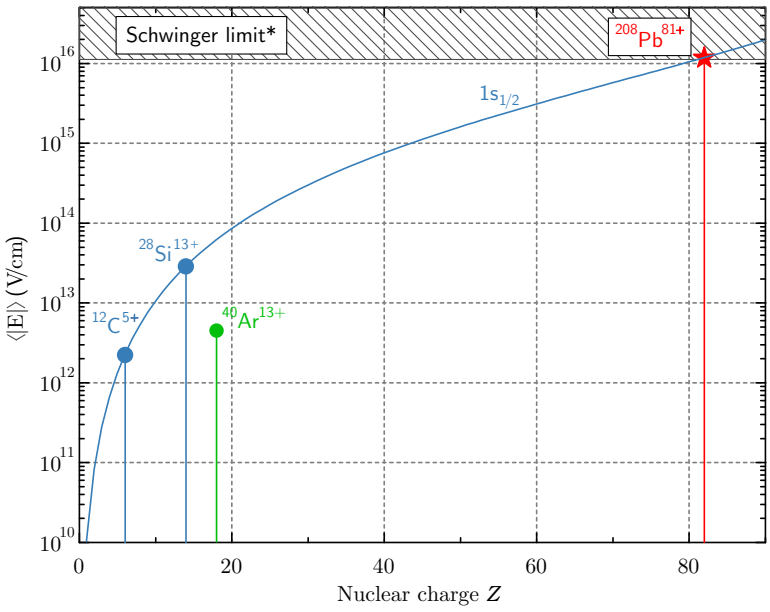

Fig. 2.2: The electric field strength in hydrogenlike ions with respect to the nuclear charge Z. In the high-Z regime the bound electron is exposed to the strongest field available in the laboratory for precision experiments on stable systems. Some of the hydrogenlike systems that have been measured already at the Mainz HCI experiment and their respective field strength regime are displayed (blue circles) for reference, as well as hydrogenlike lead $^{208}Pb^{81+}$ (red circle), the heaviest system to be targeted by ALPHATRAP. The field-strength of boronlike argon is indicated with a green circle. (*) The Schwinger limit is also displayed here.

interaction of the electron with the Coulomb potential of the nucleus in two different ways:

- Using two series expansions in orders of α and αZ, one for calculating the loop interactions of the electron with the quantised electromagnetic field or the Dirac electron-positron field, and a second one accounting for the interaction with the Coulomb potential.
- Calculating all Feynman diagrams using the eigenfunctions from the solution of the Dirac equation in the QED propagator. This leads to a solution in all orders in αZ.

The first approach is not favourable for heavy systems, as the expansion in αZ no longer converges sufficiently fast preventing a high-precision calculation of the g-factor. Using the second approach, the six Feynman diagrams shown in Fig 2.3 which correspond to the one-loop correction for the hydrogenlike system have been calculated to all orders in αZ [24]. In second order, most of the 50 Feynman diagrams have not been yet been calculated to all orders in αZ.

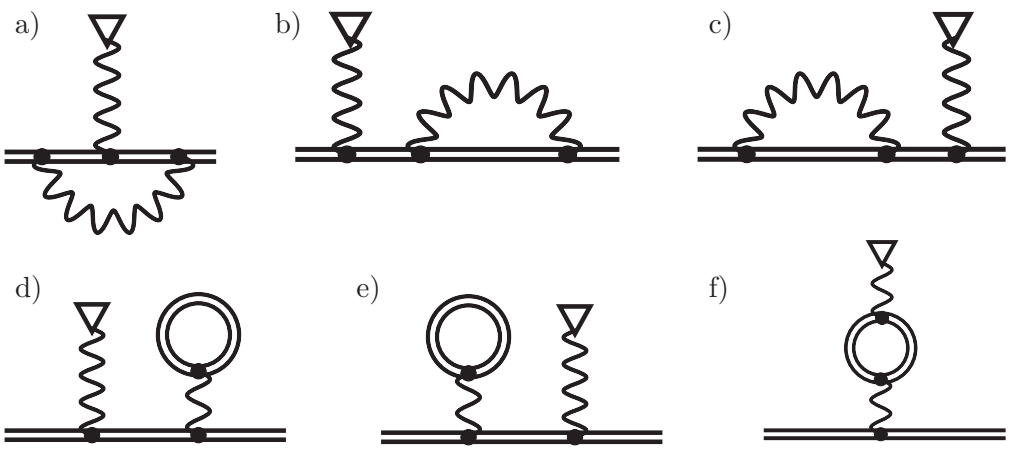

Fig. 2.3: The six Feynman diagrams of first order in the bound-state framework. Here, the double line indicates the bound-state propagator or wave function. These diagrams represent the one-loop corrections and can be calculated in all orders of αZ. (a) Corresponds to the self-energy vertex correction, while the remaining diagrams represent self-energy and vacuum-polarisation corrections to the g-factor.

In addition to the QED contributions, there are corrections arising from the nucleus within the BS-QED. Those effects are related to the finite size as well as the internal structure of the nucleus. The finite size contribution is larger for high-Z systems. The nuclear effects can be canceled when considering specific weighted g-factor differences [9, 25, 11] of different charge states of the same isotope. Furthermore, the nuclear recoil effect due to the finite mass of the nucleus needs to be considered.

Finally, for many-electron ions the interelectronic contribution needs to be accounted for. Those contributions can be divided into the ones involving photon exchanges between the electrons and the ones including additional photon or fermion loops which are called QED screening corrections.

To this date several hydrogenlike systems have been studied, leading to the stringent test of QED in strong fields which have been preformed with the g-factor of hydrogenlike silicon $^{28}Si^{13+}$ [12, 13]. The g-factor of lithiumlike ions has been exploited to access the recoil effect. That was achieved by measuring the isotope shift in lithiumlike calcium [14], where the calcium isotopes ^{40}Ca and ^{48}Ca have an almost identical nuclear charge radius. Furthermore, the g-factor of lithiumlike silicon [16] gave access to the relativistic many-electron contributions.

Within the course of this thesis, the g-factor of a five-electron system, that of a boronlike argon $^{40}Ar^{13+}$, has been measured. The experimental determination of the g-factor of such a system allows, for the first time, for precision tests of QED involving a bound electron possessing orbital angular momentum, and for more stringent tests of many-electron correlations. Furthermore, such ions, in combination

with their hydrogenic counterparts, can also be used in the future for an independent determination of the fine-structure constant α [9, 25, 11], competitive in precision with the presently best literature value [18].

2.3 Boronlike ion g-factor

For many-electron ions the uncertainty of the interelectronic interactions contributions typically dominate the uncertainty of the theoretical g-factor. For lithiumlike ions, the uncertainty of this contribution has been significantly improved [25, 26] by a rigorous QED calculation in all orders of αZ. For boronlike ions however, similar calculations are still anticipated.

The g-factor calculation of a five-electron system is increasingly challenging and requires the consideration of relativistic corrections within and beyond the Breit approximation. The most precise theoretical g-factor of $^{40}Ar^{13+}$ to date has a relative uncertainty of 9×10^{-7} [27]. This uncertainty is dominated by the current uncertainty of the many-electron, QED, and nuclear terms.

The $1s^2 2s^2 2p_{1/2}$ configuration of boronlike argon requires solving the Dirac equation including the negative-energy states of the Dirac spectrum since their contribution is comparable to the positive-energy states, similarly to the lithiumlike ions [16]. The ground-state g-factor of such an ion without nuclear spin can be expressed as:

$$g = g_{\mathrm{D}} + \Delta g_{\mathrm{int}} + \Delta g_{\mathrm{QED}} + \Delta g_{\mathrm{recoil}} + \Delta g_{\mathrm{NS}}, \tag{2.4}$$

where g_{D} is the Dirac value for a pointlike nucleus, Δg_{int} is the interelectronic interaction, Δg_{QED} is the QED contribution, $\Delta g_{\mathrm{recoil}}$ is the nuclear recoil correction and Δg_{NS} is the nuclear size correction. These contributions have been calculated for a boronlike argon $^{40}Ar^{13+}$ in [27] and are given in Tab. 2.1. For a range of nuclear charges, Z, these contributions are plotted in Fig. 2.4. It can be seen that most of the individual contributions increase in the presence of stronger fields. The minimum of the VP curve is due to the partial cancellation of the one-electron VP and VP screening diagrams [28].

Dirac value

The Dirac contribution to the g-factor is the leading-order contribution in α and $1/Z$ and it is given analytically for a pointlike nucleus, as described in Refs. [29, 30]:

$$g_{\mathrm{D}} = \frac{2}{3}\left(\sqrt{2\left(1+\sqrt{1-(\alpha Z)^2}\right)}-1\right) = \frac{2}{3} - \frac{1}{6}(\alpha Z)^2 - ..., \tag{2.5}$$

where Z is the atomic number. Because of the nonvanishing angular momentum of the state, unlike for s states, this g-factor is significantly different from the free Dirac value of 2. This modifies the range of the Larmor frequency to be measured by about a factor of three, however, with slight modifications in the ALPHATRAP setup the g-factor for p states can be determined with the same technique.

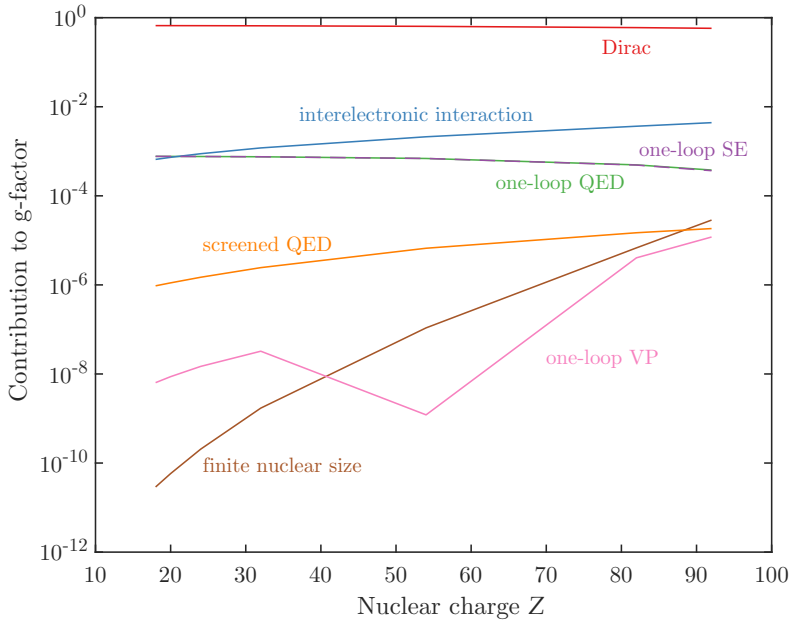

Fig. 2.4: Individual contributions to the g-factor of boronlike ions [28]. Here contributions due to the interelectronic interaction, one-loop QED, screened QED, vacuum polarisation (VP) and finite nuclear size are plotted. The current level of precision for $^{40}Ar^{13+}$ gives access to the individual contributions.

Interelectronic interaction

In a boronlike ion, the presence of five electrons increases the complexity of the system at hand. The electron-correlation effect of such systems is commonly calculated with the configuration-interaction method. Within this method, the $1s$ and $2s$ core electrons are fully correlated, i.e. they are not assumed to be frozen orbitals which only influence the $2p$ valence electron via their electrostatic screening potentials.

The one-photon exchange term $(1/Z)^1$ of the interelectronic interaction contribution was calculated within the QED framework [31, 32, 33] for $^{40}Ar^{13+}$. The two-photon exchange term $(1/Z)^{2+}$ was calculated in the so-called Breit approximation, i.e., neglecting certain higher-order retardation terms in the photon exchange using the configuration-interaction method in the Dirac-Fock-Sturm (CI-DFS) basis as for lithiumlike ions in Refs. [34, 35, 36]. Furthermore, it has also ben recently confirmed using the coupled-cluster method [37]. In Ref. [38] the term is calculated for middle-Z boronlike ions within second order perturbation theory in $1/Z$. In order to improve the precision of this contribution, a combination of CI-DFS and recursive higher-order perturbation theory is used and the result is indicated with a * in Tab. 2.1.

QED contributions

The leading effects of the QED contribution for many-electron ions such as a boronlike ion, are the self-energy and the vacuum polarisation correction. Those two

corrections comprise the one-loop QED contribution. The self-energy corrections have been calculated in Ref. [39, 40] for hydrogenlike ions to all orders in $Z\alpha$ for low-Z ions. In Ref. [35] it has been calculated for $^{40}Ar^{13+}$ using an effective screening potential. Within this approximation the core electrons are considered as frozen, which allows estimating the interaction of the active electron and nucleus with the use of a modified potential, the effective screening potential.

The precision of the self-energy contribution to the g-factor of boronlike argon has been improved by means of considering the screening effect of the $2p_{1/2}$ valence electron as an effective potential induced by the core electrons by two different numerical methods. This has been achieved (1) by a local screening potential following Ref. [41] and (2) on the basis of the dual-kinetic balance (DKB) approach [32] following Refs. [42, 43]. The self-energy correction calculated using method (2) is indicated in Tab. 2.1 with a *. The two-electron self-energy Feynman diagrams have not been calculated yet. However, it has been estimated by calculations performed for lithiumlike ions [25]. This resulted in an uncertainty of 0.51×10^{-6} which is included in the final theoretical g-factor.

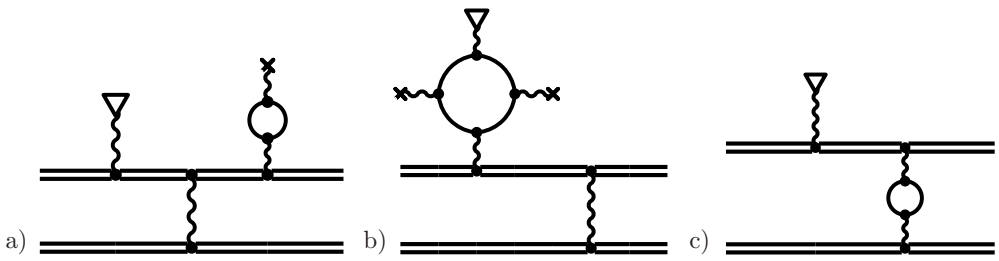

Fig. 2.5: Examples of vacuum-polarisation screening corrections of order 1/Z to the g-factor of the boronlike ground state. (a) electron-positron correction for the bound-electron interaction with the nucleus (electric loop VP) or (b) its interaction with the external magnetic field (magnetic loop VP). (c) Photon-exchange VP loop correction. A single line represents a free virtual fermion, and the wavy line terminated by a cross stands for the interaction with the nuclear Coulomb potential.

The vacuum-polarisation corrections are not relevant for the current theoretical precision of $^{40}Ar^{13+}$. Nevertheless, they are calculated and given in Tab. 2.1 and some example Feynman diagrams of VP corrections are shown in Fig. 2.5. Those contributions will be significant for heavy HCI (see Fig. 2.4) such as boronlike lead $^{208}Pb^{77+}$, for which they are estimated to be -4.06×10^{-6}. For more details see Ref. [28].

Nuclear recoil

The nuclear recoil contribution which is caused by the relativistic interaction between the nucleus, which has a finite mass, and the electron, necessitates calculations beyond the external-field approximation (Furry picture). That means that the nucleus

in not considered as a stationary Coulomb potential. The purely relativistic nuclear recoil effect has been addressed in the isotope shift of lithium like calcium [14, 44].

Compared to the hydrogenlike and lithliumlike ions experimentally investigated so far, the contribution is more pronounced for a p state of a boronlike ion, i.e. for $^{40}Ar^{13+}$ it amounts to $-9.09(19) \times 10^{-6}$. Furthermore, the current uncertainty of the recoil correction of boronlike ions is much larger than the one for hydrogen- and lithiumlike ions. The nuclear recoil correction for an $^{40}Ar^{13+}$ ion has been evaluated to zeroth and first orders of $1/Z$ in Refs. [36, 45].

Nuclear size

The leading contribution of the nuclear-size correction for a $2p_{1/2}$ state is given by [46, 38]:

$$\Delta g_{\mathrm{NS}} = \frac{(\alpha Z)^6}{16} m_{\mathrm{e}}^2 R_{\mathrm{nucl}}^2, \tag{2.6}$$

where R_{nucl} is the root-mean-square (rms) charge radius of the nucleus. According to Ref. [46] this contribution scales with $\frac{8}{3}(\alpha Z)^4$ for ns states. For boronlike argon this contribution amounts to $< 10^{-10}$, which is much smaller that the current theoretical precision and is thus negligible. However, in the high-Z range it is on the order of 10^{-6} to 10^{-5}, as can be seen in Fig. 2.4. When considering specific g-factor differences of heavy hydrogen- and boronlike ions, it has been demonstrated [9] that the large suppression of the nuclear size correction for the $2p_{1/2}$ compared to the $1s$ state, does not induce a significant cancelation of the α-dependent term. Therefore, this specific difference could allow for a high-precision determination of α.

Theoretical g-factor of $^{40}Ar^{13+}$

The different contributions discussed above are summarised in Tab. 2.1. The final theoretical g-factor is

$$g_{\mathrm{th}} = 0.663\,648\,12(58), \tag{2.7}$$

where the uncertainty has been improved by reducing the uncertainty of the one-loop QED contribution by a factor of 3 [28] and by reducing the uncertainty of the electron correlation contributions by combining the CI-DFS approach with recursive perturbation theory (P. Th.) to third and higher orders in $1/Z$.

This result is in good agreement with previous results given in Ref. [38] and in Ref. [36]. Those results vastly disagree with the calculated values given in Ref. [48] and Ref. [49]; furthermore, the result in the latter article is given without error bars. The different theoretical g-factors together with the experimental one presented in this thesis are compared in Fig. 7.7.

Tab. 2.1: Theoretical contributions to the g-factor of $^{40}Ar^{13+}$. The parenthesised numbers indicate the uncertainty of the last digit(s). All digits are significant if no uncertainty is given. Those contributions have been calculated in Ref. [27]. The predicted value of the g-factor from different calculations are given below.

Contribution	Value	Ref.
Dirac value	0.663 775 45	
Finite nuclear size	$< 10^{-10}$	
Electron correlation:		
one-photon exchange, $(1/Z)^1$	0.000 657 53	
$(1/Z)^{2+}$, CI-DFS	−0.000 007 5(4)	[36]
$(1/Z)^{2+}$, P. Th. & CI-DFS	−0.000 007 57(20)*	
Nuclear recoil	−0.000 009 09(19)	[45, 36]
One-loop QED:		
self-energy, $(1/Z)^0$	−0.000 768 372 3(3)	
$(1/Z)^{1+}$	−0.000 000 98(15)	
$(1/Z)^{1+}$	−0.000 001 04(19)*	
vacuum polarisation		
electric loop, $(1/Z)^0$	-4.187×10^{-10}	
$(1/Z)^1$	$6.526(2) \times 10^{-9}$	
magnetic loop, $(1/Z)^0$	4.131×10^{-10}	
$(1/Z)^1$	-1.341×10^{-10}	
Two-loop QED, $(Z\alpha)^0$	0.000 001 18(6)	[47]
Total theory	0.663 648 2(5)	
	0.663 648 08(58)*	
Theory g-factor	0.663 648 12(58)	[27]
	0.663 648 8(12)	[38]
	0.663 647 7(7)	[36]
	0.663 899(2)	[48]
	0.663 728	[49]

2.4 Measurement principle

In order to test the validity of the theory the same quantity is experimentally determined. To this end, a single HCI of interest is exposed to a strong magnetic field B_0 where the Zeeman splitting of the ground-state energy level is given by

$$\Delta E = g\mu_{\mathrm{B}} B_0 = h\frac{ge}{4\pi m_{\mathrm{e}}} B_0, \tag{2.8}$$

with

$$\nu_{\mathrm{L}} = g\frac{e}{4\pi m_{\mathrm{e}}} B_0 \tag{2.9}$$

being the spin-precession frequency or else Larmor frequency. The determination of the g-factor requires measuring the strength of the external magnetic field B_0.

This is achieved by means of the ion's free-cyclotron frequency in the same magnetic field:

$$\nu_{\mathrm{c}} = \frac{1}{2\pi}\frac{q}{m}B_0, \tag{2.10}$$

where q is the charge state and m is the mass of the ion. Combining equations (2.9) and (2.10) we obtain the g-factor with respect to the Larmor-to-cyclotron frequency ratio as follows:

$$g = 2\frac{m_{\mathrm{e}}}{m}\frac{q}{e}\frac{\nu_{\mathrm{L}}}{\nu_{\mathrm{c}}} = 2\frac{m_{\mathrm{e}}}{m}\frac{q}{e}\Gamma, \tag{2.11}$$

where $\Gamma = \frac{\nu_{\mathrm{L}}}{\nu_{\mathrm{c}}}$. Therefore by measuring the frequency ratio Γ and obtaining the mass ratio $\frac{m_{\mathrm{e}}}{m}$ from independent dedicated measurements, we experimentally determine the g-factor.

3 Penning trap

For the experimental determination of the g-factor with a fractional uncertainty of 10^{-9} or better, the frequency ratio Γ needs to be determined with the same precision. For this, we need to perform experiments on a single ion of interest when it is exposed to a very homogeneous magnetic field. Additionally, a very good vacuum in the order of $1 \times 10^{-16}\,\mathrm{mbar}$ or better is necessary that allows for storing a single ion for long periods of time without any disturbance in the ion's motion due to collisions with residual gas particles. For these reasons a Penning trap is the most appropriate tool and is used in our experimental setup for ion confinement and high-precision spectroscopy. In this chapter the main principles of an ideal Penning trap are introduced in section 3.1, followed by the real Penning-trap setup in section 3.2. Finally, the optimised design of the ALPHATRAP high-precision Penning trap is briefly introduced in section 3.3.

3.1 Ideal Penning trap

An ideal Penning trap is the superposition of a magnetic and an electrostatic field that can confine charged particles in all directions. The strong homogeneous magnetic field, defined as $\vec{B} = B_0\hat{z}$, confines the charged particle radially. By means of the Lorentz force

$$\vec{F}_\mathrm{L} = q\vec{v} \times \vec{B} \tag{3.1}$$

the ion with charge q and velocity $\vec{v}$ is forced to gyrate around the magnetic field lines with an angular frequency

$$\omega_\mathrm{c} = \frac{q}{m} B_0, \tag{3.2}$$

with $\nu_\mathrm{c} = \omega_\mathrm{c}/2\pi$ being the so-called free-space cyclotron frequency and q/m the ion's charge-to-mass ratio. Thus, the particle is confined within the radial plane. The axial confinement of the particle in the $\hat{z}$-direction is achieved by a weak electric quadrupole potential (Fig. 3.1(right)):

$$V_\mathrm{ideal}(\rho, z) = V_0 \frac{C_2}{2d^2}(z^2 - \frac{\rho^2}{2}), \tag{3.3}$$

where V_0 is the voltage difference between the ring electrode and the endcap electrodes, d is a characteristic trap length, C_2 is a dimensionless field parameter and $\rho^2 = x^2 + y^2$.

For the ideal case of a perfectly harmonic quadrupole potential, a Penning trap with infinitely large electrodes would be necessary. A Penning trap with hyperbolically shaped electrodes as well as the resulting quadrupole potential are shown in

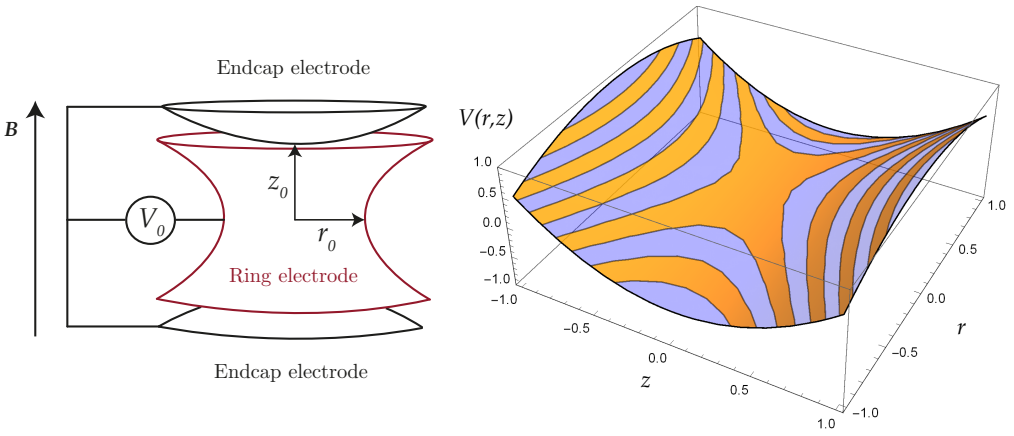

Fig. 3.1: (left) Sketch of a Penning trap with hyperbolically shaped electrodes. The external magnetic field is in the axial direction. In red the ring electrode is shown where the voltage V_0 is applied with respect to the endcap electrodes. (right) The resulting potential $V_{ideal}(\rho, z)$ is plotted.

Fig. 3.1. Creating a trapping potential would require at least three electrodes[1]: a ring electrode and a set of endcap electrodes. Typically, the endcap electrodes are grounded and the voltage difference V_0 is created by applying the voltage V_0 on the ring electrode.

The resulting motion is the superposition of three harmonic modes of oscillation. In the non-relativistic classical framework, the equation of motion reads:

$$\begin{pmatrix} \ddot{x} \\ \ddot{y} \\ \ddot{z} \end{pmatrix} = \frac{qB_0}{m} \begin{pmatrix} \dot{y} \\ -\dot{x} \\ 0 \end{pmatrix} + \frac{q}{m} \frac{V_0 C_2}{2d^2} \begin{pmatrix} x \\ y \\ -2z \end{pmatrix}. \tag{3.4}$$

The motion in the axial direction, conventionally defined in the z-direction, is decoupled from the other two radial components and describes a harmonic oscillation in the axial direction, with the axial frequency[2]

$$\omega_z = \sqrt{\frac{q}{m} \frac{V_0 C_2}{d^2}}. \tag{3.5}$$

In the radial direction, the ion is exposed to both the confining force of the magnetic field and the de-confining effect of the perpendicular component of the electric field. Solving the system of differential equations in (3.4) for the radial modes yields two independent solutions with the radial frequencies being:

$$\omega_\pm = \frac{\omega_c}{2} \pm \frac{1}{2}\sqrt{\omega_c^2 - 2\omega_z^2}, \tag{3.6}$$

[1] In principle at least *two* electrodes are required, e.g. a ring electrode enclosed in a spherical endcap electrode.

[2] For simplicity, the frequency ν and angular frequency $\omega = 2\pi\nu$ are used interchangeably.

where ω_+ and ω_- are the modified cyclotron and the magnetron frequency respectively.

The two radial modes are the *modified cyclotron mode* and the *magnetron mode*. The latter is a result of the $\vec{E} \times \vec{B}$ drift, which forces the ion into a slow oscillation in the radial plane, with frequency ω_-. This drift is caused by the $\vec{E}_\perp$ component of the electric field, which shifts the centre of the cyclotron mode outwards from the trapping centre, as shown in Fig. 3.2(left). The modified cyclotron mode is in the ideal case the free-space cyclotron frequency ω_c reduced by the magnetron frequency.

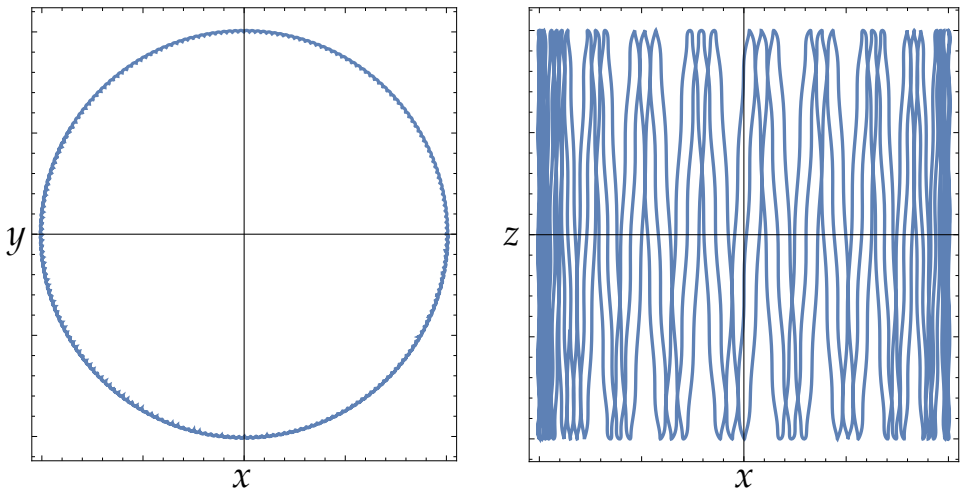

Fig. 3.2: Motion of a $^{40}Ar^{13+}$ ion in a Penning trap when projected in the xy-plane (left) and the xz-plane (right). The frequency ratio ω_+/ω_- is here arbitrarily chosen to be 382 for demonstration purposes.

The superposition of the three modes resulting in the combined orbit of a single ion in a Penning trap when projected in the xy- and xz-plane is shown in Fig. 3.2. The stability region of a Penning trap is defined in the limit of real frequencies, and from equation (3.6) we obtain:

$$B_0 > \sqrt{2\frac{m}{q}\frac{V_0 C_2}{d^2}}, \tag{3.7}$$

which is satisfied for a weak electric field and light masses. When this condition is not satisfied the ion is no longer confined in the radial direction leading to ion loss. Consequently, for typical trapping parameters, the frequencies are sorted following the hierarchy

$$\omega_c > \omega_+ \gg \omega_z \gg \omega_-. \tag{3.8}$$

For an $^{40}Ar^{13+}$ ion in a magnetic field $B_0 \approx 4.02\,\mathrm{T}$ and an electrostatic potential of $V_0 \approx -75\,\mathrm{V}$, the eigenfrequencies are $\nu_+ \approx 20\,\mathrm{MHz}$, $\nu_z \approx 650\,\mathrm{kHz}$ and $\nu_- \approx 10\,\mathrm{kHz}$. In an ideal Penning trap, the following relations between the eigenfrequencies hold:

$$\omega_c = \omega_+ + \omega_-, \tag{3.9}$$
$$\omega_z^2 = 2\omega_+\omega_-, \tag{3.10}$$

both of which are a direct outcome of equation (3.6). Within the invariance theorem [50, 51] the free-space cyclotron frequency ω_c is related with the three eigenfrequencies as follows:

$$\omega_c^2 = \omega_+^2 + \omega_z^2 + \omega_-^2. \tag{3.11}$$

The above relation is the one we use to determine the free-space cyclotron frequency by measuring the three eigenmodes' frequencies in our Penning trap. That is because equation (3.11) holds not only in the case of an ideal Penning trap, but also in the presence of imperfections (see section 3.2) such as misalignment between the electric and the magnetic field as well as ellipticity of the electrodes. The latter would force the motion of the ion into an elliptical radial orbit. These unavoidable imperfections that are met in a real Penning trap are cancelled via the *invariance theorem*.

Within the classical interpretation, the energy of the radial modes is given by the sum of the kinetic energy and the repulsive electrostatic potential energy [50]:

$$E_+ = \frac{1}{2}m(\omega_+^2 r_+^2 - \frac{1}{2}\omega_z^2 r_+^2) \approx \frac{1}{2}m\omega_+^2 r_+^2, \tag{3.12}$$
$$E_- = \frac{1}{2}m(\omega_-^2 r_-^2 - \frac{1}{2}\omega_z^2 r_-^2) \approx -\frac{1}{4}m\omega_z^2 r_-^2, \tag{3.13}$$

where r_+ and r_- are the radius of the modified cyclotron and magnetron motion, respectively. From equations (3.13) and (3.8) it should be noted that the magnetron mode is dominated by the potential energy and therefore exhibits a negative energy. Consequently, the energy of the mode is decreased by increasing its radius r_- and *vice versa*, making this mode metastable.

Due to the frequency hierarchy given in equation (3.8) it becomes immediately apparent that the largest contribution to the free-space cyclotron frequency determination comes from measuring the modified cyclotron frequency. Consequently, the final uncertainty of ν_c is dominated by the uncertainty of ν_+.

3.2 The real Penning trap

The ideal Penning trap, that has been discussed in the previous section, assumes infinitely large electrodes which makes it impossible to be implemented in the laboratory. Furthermore, even if an infinitely large trap would be possible the motion of the ion would be disturbed by, e.g., relativistic (see section 3.2.3) and image charge effects (see section 4.2).

Nevertheless, the realisation of a Penning trap as close to the ideal case as possible is a challenging task and it is essential for the remaining imperfections to be well understood and compensated for as much as possible. Even though a Penning trap with hyperbolically shaped electrodes seems appropriate because the shape of the trapping electrodes follow the equipotential field lines, this type of a Penning trap has disadvantages. These include the manufacturing precision, the additional difficulty in handling and aligning hyperbolically-shaped electrodes and, most importantly, the fact that there is no possibility for external ion injection or ion transport without introducing holes on the electrodes. The latter would modify the electrostatic quadrupole potential and shift it from the perfectly harmonic field. To overcome these, G. Gabrielse suggested the use of a cylindrical Penning trap instead [52], where the simpler geometry makes the machining of the individual electrodes easier, trap assembly becomes more straight forward and the trapping region is externally accessible within this open-endcap configuration.

A cylindrical Penning trap consists of at least three stacked electrodes: a ring electrode and two endcap electrodes. Typically in most experiments that use the cylindrical configuration, five electrodes which includes another set of correction electrodes are used. A drawing of such a configuration is shown in Fig. 3.3.

3.2.1 Electric field imperfections

Given the finite size of the electrodes, the electrostatic quadrupole potential will deviate from the ideal case even with a hyperbolical Penning trap. As mentioned above, most of the disadvantages of a hyperbolical trap can be avoided with a cylindrical Penning trap which is also used in ALPHATRAP. Machining imperfections,

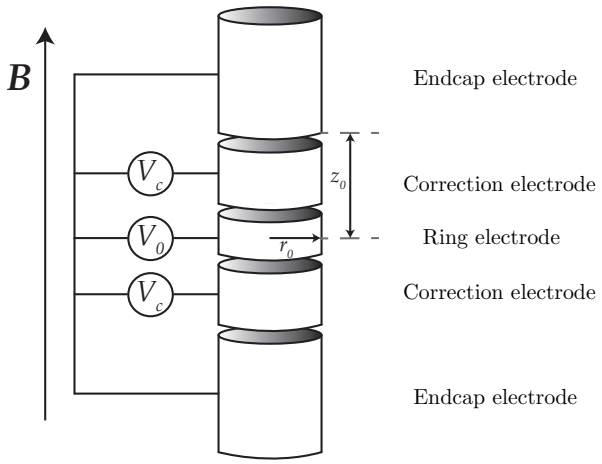

Fig. 3.3: Drawing of a cylindrical Penning trap. In this example, the trap consists of a ring electrode, a set of correction electrodes and two endcap electrodes that are typically grounded. The external magnetic field is in the axial direction while the axial particle confinement is achieved by applying a voltage V_0 at the ring electrode.

the presence of patch potentials on the inner surface of the electrodes as well as possible electrode misalignment during trap-assembling do contribute to a non-perfect trapping potential. Even though for a cylindrical configuration these effects can be reduced leading to a close-to-ideal field, the unavoidable remaining sources of trapping inhomogeneities need to be entirely understood and controlled.

A cylindrical Penning trap consists of a stack of cylindrical electrodes where the trapping potential is created by applying a voltage on the central electrode (the ring electrode), while the endcap electrodes are typically grounded as in the example case in Fig. 3.3. In order to create a quadrupole electric potential that resembles the ideal one as much as possible, additional sets of electrodes are placed next to the ring electrode. The dimensions of these correction electrodes and the voltage applied to them are chosen such that the axial symmetry is maintained.

It should be noted that the cylindrical symmetry of the trap is broken by existing slits on the electrodes, that are split in order to allow for ion excitation, manipulation and detection. Nevertheless, the remaining dominant electric field inhomogeneities maintain cylindrical symmetry. The trapping potential can be written as a series expansion:

$$V(r,\theta,z) = \frac{V_0}{2}\sum_{n=0}^{\infty} C_n \left(\frac{r}{d}\right)^n P_n(\cos\theta), \tag{3.14}$$

where V_0 is the voltage difference between the ring electrode and the endcap electrodes, d is a characteristic length of the trap, C_n are dimensionless expansion coefficients and $P_n(\cos\theta)$ are the Legendre polynomials. In the axial direction, all odd coefficients vanish due to the inherent mirror symmetry. For the ideal quadrupole potential all coefficients would be zero for $n > 2$, and the C_2-term describes the harmonic electrostatic potential in the z-direction, and it is given according to equation (3.5). Energy dependent frequency shifts were rigorously calculated in Ref. [50], and the dominant contribution, which relates to the C_4 coefficient in first order, can be written in a matrix form:

$$\begin{pmatrix} \Delta\nu_+/\nu_+ \\ \Delta\nu_z/\nu_z \\ \Delta\nu_-/\nu_- \end{pmatrix} = \frac{6C_4}{qV_0C_2^2} \begin{pmatrix} \frac{1}{4}(\nu_z/\nu_+)^4 & -\frac{1}{2}(\nu_z/\nu_+)^2 & -(\nu_z/\nu_+)^2 \\ -\frac{1}{2}(\nu_z/\nu_+)^2 & \frac{1}{4} & 1 \\ -(\nu_z/\nu_+)^2 & 1 & 1 \end{pmatrix} \cdot \begin{pmatrix} E_+ \\ E_z \\ E_- \end{pmatrix} \tag{3.15}$$

The presence of C_n-related contributions of the electrostatic field, would limit the measurement precision. Therefore, it is of outmost importance to eliminate as many higher-order contributions as possible. For this purpose, the design of the ALPHATRAP trap electrodes have been very carefully calculated and optimised. The remaining inhomogeneities can be experimentally determined and compensated for.

3.2.2 Magnetic field imperfections

The externally imposed magnetic field will always slightly deviate from the perfectly homogeneous magnetic field lines even if great care is taken when, e.g., the superconducting magnet is shimmed. The remaining $\vec{B}$-field imperfections are additionally caused by the residual magnetisation of the different material that compose the experimental setup, when the latter is exposed to the external magnetic field.

Similarly to the electric field, the magnetic field can be expanded in terms of Legendre polynomials. The corresponding series expansion can be further simplified for the case of $r = 0$ at the center of the magnet:

$$B_z(z) = \sum_{i=0}^{\infty} B_i z^i, \tag{3.16}$$

where the radial components are insignificant in comparison with the axial ones. The leading order contribution for the $\vec{B}$-field imperfections in the trapping region, the quadratic residual magnetic bottle $\sim B_2 z^2$ inhomogeneity, induces energy dependent frequency shifts that have been calculated in Ref. [50]:

$$\begin{pmatrix} \Delta\nu_+/\nu_+ \\ \Delta\nu_z/\nu_z \\ \Delta\nu_-/\nu_- \\ \Delta\nu_L/\nu_L \end{pmatrix} = \frac{B_2}{B_0 m(2\pi\nu_z)^2} \begin{pmatrix} -(\nu_z/\nu_+)^2 & 1 & 2 \\ 1 & 0 & -1 \\ 2 & -1 & -2 \\ -(\nu_z/\nu_+)^2 & 1 & 2 \end{pmatrix} \cdot \begin{pmatrix} E_+ \\ E_z \\ E_- \end{pmatrix}. \tag{3.17}$$

It should be noted that the energy dependent frequency shifts that are given in equations (3.15) and (3.17) are according to Ref. [50], where it is assumed that $\nu_+ \gg \nu_-$. This approximation is suitable for small shifts and the typically low energies, therefore they are suitable for the present work. The same shifts have been calculated in Ref. [53], where the energy dependent shifts are obtained from first principles. There, a Taylor expansion is used which assumes small effects which applies for ALPHATRAP and the present work.

3.2.3 Relativistic corrections

So far, the ion motion and the corresponding shifts are considered non-relativistically. The high precision of our measurements, however, requires to account for the relativistic mass increase. A simple model is commonly used to describe frequency shifts due to the relativistic mass increase of the ion in the reference frame of the lab. Even though in reality the relativistic corrections are more complex, it has been shown in Ref. [54] that this approximation is in very good agreement with the complex relativistic corrections to the equation of motion, and is more than sufficient to describe the relative shift of the free-space cyclotron frequency.

According to Ref. [54], and since typically the ion's velocity and amplitudes are small enough to allow approximating the mass of the particle by

$$\gamma m = \frac{m}{\sqrt{1 - v^2/c^2}} \approx m(1 + \frac{v^2}{2c^2}) \tag{3.18}$$

with the relative mass increase

$$\frac{\Delta m}{m} = \frac{v^2}{2c^2}. \tag{3.19}$$

Translating the mass shift into a free-space cyclotron frequency shift by use of equation (3.2), we obtain the relative shift of ν_c:

$$\frac{\Delta \nu_c}{\nu_c} = -\frac{\Delta m}{m} \approx -\frac{\langle E_+ \rangle}{mc^2}. \tag{3.20}$$

It is shown in the same paper that this approximation is in very good agreement with the precise determination of the relativistic shifts.

The reference frame of the valence electron's precession is the particle itself, therefore in order to estimate the size of the effect on the Γ ratio we need to transform back to the reference frame of the laboratory. Taking the latter into account, the relativistic shift on the electron precession frequency reads [55] :

$$\frac{\Delta \nu_L}{\nu_L} \approx \frac{\Delta \nu_c}{\nu_c} \frac{\nu_c}{\nu_L}. \tag{3.21}$$

For the case of the relativistic correction to the Larmor frequency, it is interesting to note that the shifts in the two frequencies do not cancel out, the shift is different for both. For typical energies and amplitudes during the *g*-factor measurement, and for a single $^{40}Ar^{13+}$ in our setup, the maximal relativistic mass increase is in the order of $\sim 10^{-13}$, and thus negligible for the current level of precision.

3.3 The ALPHATRAP optimised design

The central tool of our experimental setup is the Penning trap, specifically the precision trap that is used for high-precision spectroscopy. Therefore, it is of outmost importance to optimise as well as understand and control the characteristics of the precision trap as much as possible. The advantages that are entailed by the choice of a cylindrical Penning trap (see also section 3.2), include better machining precision, external access for ion injection as well as laser and microwave injection without modifications on the electrodes.

In a real configuration, the potential is deviating from the ideal case. For this reason, additionally to the ring electrode, correction electrodes are used to minimise anharmonicities of the quadrupole trapping potential. Most Penning-trap setups use a *5-electrode* configuration. In order to compensate for higher order field components, in ALPHATRAP we use a *7-electrode* configuration. That way, we achieve higher harmonicity and a larger trapping region, which allows excitations to larger amplitudes without energy dependent frequency shifts.

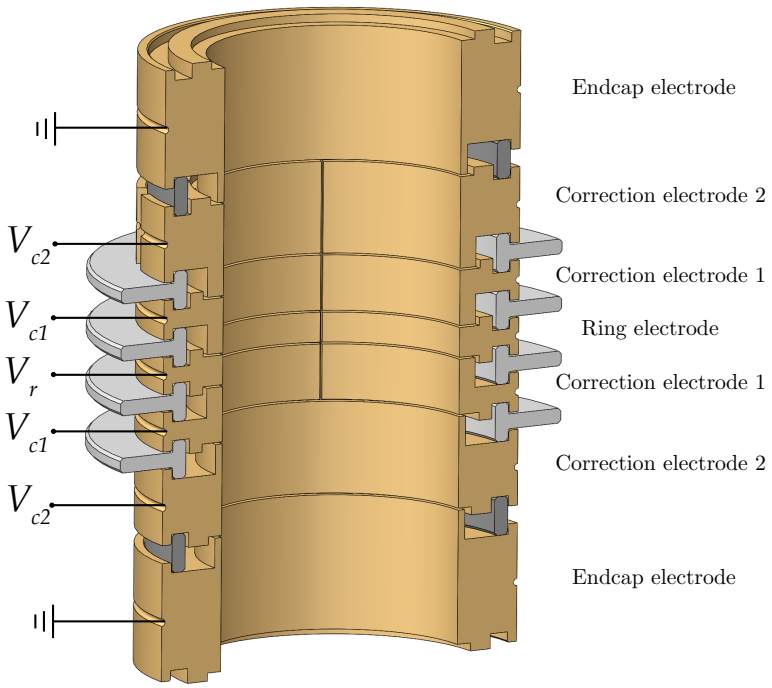

Fig. 3.4: Drawing of the seven-electrode configuration. The length definition variables for all electrodes are indicated in the figure.

The ALPHATRAP precision trap consists of a ring electrode two upper correction electrodes, two lower correction electrodes and upper and lower endcap electrodes as shown in Fig. 3.4. In order to minimise the deviation of the real trapping potential from the ideal electrostatic quadrupole potential, the dimensions of the trap electrodes where optimised prior to manufacturing. The design of the precision-trap electrodes are similar to the LIONTRAP electrodes [56, 57] but with a larger radius of $r = 9\,\mathrm{mm}$, which allows for high-precision measurements up to hydrogenlike $^{208}Pb^{81+}$. Both the ALPHATRAP and LIONTRAP electrode dimensions where optimised analytically by Florian Köhler [44]. Within this work, the dimensions of the ALPHATRAP precision trap were independently analytically verified to be optimal. A detailed description of the trap as well as the trapping potential is discussed is section 5.1.1.

Ion detection and manipulation

4

In order to perform high-precision measurements of the g-factor with a single ion in a Penning trap, not only a highly-optimised setup is required as described in the previous chapter, but also the ability to perform several measurements on the same ion over a significant course of time. This can be achieved with a non-destructive ion-detection scheme, where the ion's eigenfrequencies are detected via the induced charges on the electrodes surfaces. The very low oscillating current combined with the cryogenic environment require sophisticated detection electronics, which have been detailed in Refs. [58, 59].

The g-factor is obtained by the frequency ratio $\Gamma = \nu_{\mathrm{L}}/\nu_c$ which in extend requires measuring the three eigenfrequencies of the ion as well as determining the ion's Larmor precession frequency. In this chapter, the basic principle of the image current detection technique will be presented in the first section 4.1, followed by section 4.2 where the interaction between the ion and the detection system is discussed. In section 4.3 the measurement technique of the axial frequency is presented. The detection of both radial modes can be achieved by suitable coupling to the axial mode as explained in section 4.4. The Larmor frequency is measured by use of the continuous Stern-Gerlach effect which is introduced in section 4.5. Finally, the magnetic moment dynamics as well as the Adiabatic Rapid Passage technique, that was used for the search of the resonance prior to the g-factor measurement, is presented in section 4.6.

4.1 Image current detection

While the ion oscillates in the trap, it induces charges on the surfaces of the electrodes. In the axial direction for example, the induced image charges oscillate between the upper and lower correction electrodes with the ion's axial frequency. If we consider the trap as an ideal capacitor with the ion oscillating between the two plates, the current that it induces is

$$I_{\mathrm{ind}} = \frac{q}{D_{\mathrm{eff}}}\dot{z}, \tag{4.1}$$

where $z(t) = z_0 \cos(\omega_z t + \phi)$ and D_{eff} being the effective electrode distance. D_{eff} is defined as the distance between the two infinitely-large capacitor plates, where the induced charge due to the ion is the same field as in the real trap. In the real case of a cylindrical Penning trap, the effective electrode distance can be numerically calculated and it depends on the trap geometry and on the particular electrode chosen to be the signal pick-up electrode.

The induced current on the electrodes' surfaces is typically a few fA. In order to measure this tiny oscillating current, we connect a large impedance in parallel to the

trap. That way, we can probe the oscillation frequency of the ion by measuring the voltage drop across the impedance. This tank circuit is essentially a superconducting, high-impedance coil with inductance L and a high impedance Z. Details about the detection electronics can be found in the ALPHATRAP review publication [58] and in the PhD thesis of Andreas Weigel [59]. In combination with the parasitic capacitance C of the trap, the total impedance of the tank circuit is

$$Z(\omega) = \left(\frac{1}{R} + i\omega C - \frac{i}{\omega L}\right)^{-1}. \tag{4.2}$$

In the case where the ion is absent, the detected spectrum of the resonator (as shown in figure 4.1) is described by the function [55, 44]:

$$u_{\mathrm{res}}(\omega) = 10\log_{10}\left(A_{\mathrm{off}}^2 + \frac{A\cdot R}{1+(Q(\frac{\omega}{\omega_{\mathrm{R}}} - \frac{\omega_{\mathrm{R}}}{\omega}))^2}\right) + \theta\cdot(\omega-\omega_{\mathrm{R}}), \tag{4.3}$$

where A_{off} is the noise level offset due to the electronic noise of the cryogenic amplifier which is also amplified by the amplification factor Amp, $A = Amp\sqrt{4k_{\mathrm{B}}T\delta\nu R_{\mathrm{P}}}$ is the amplitude with $\delta\nu$ the frequency bandwidth, R is related to the effective parallel resistance of the resonator, $Q = \nu_{\mathrm{R}}/\Delta\nu$ is the quality factor of the resonator, and θ is the slope of the transfer function of the amplifier. Here $u_{\mathrm{res}}(\omega)$ is given in units of dBVrms with $1\,\mathrm{dBVrms} = 20\log_{10}(1\,\mathrm{Vrms})$.

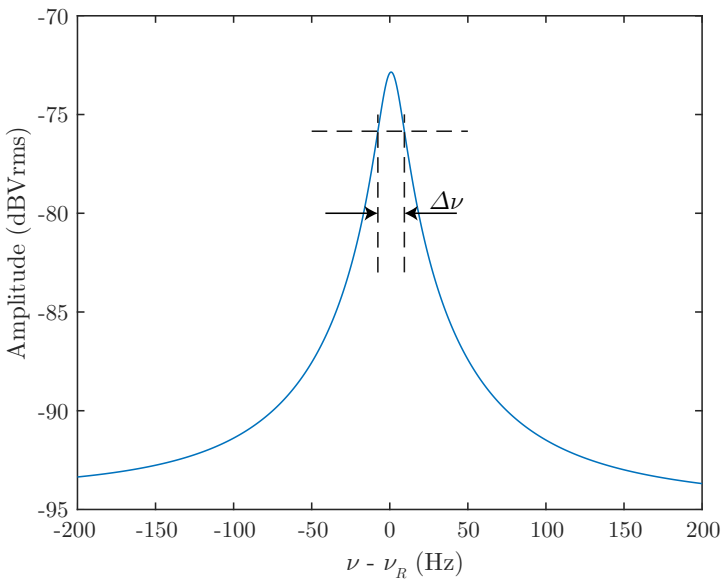

Fig. 4.1: The thermal noise of the axial resonator connected to the trap. In the figure, the width $\Delta\nu$ of the resonance is indicated at $-3\,\mathrm{dB}$ from the maximum, which is related to the Q value by $Q = \nu_{\mathrm{R}}/\Delta\nu$.

4.2 Ion-resonator interaction

If we now consider an ion present in the trap, it will interact with the resonator as well as with the induced image charges. These interactions lead to some important effects: resistive cooling, dip detection, image charge shift and frequency pulling. Even though resistive cooling and dip detection are essential for ion cooling and non-destructive detection, the image charge and frequency pulling effects introduce unwanted shifts. These effects are being discussed in this section.

The detection system is cryogenically cooled to a temperature of $4.2\,\mathrm{K}$. Therefore, there is no access to the cryogenic detection electronics while the experiment is in operation. Consequently, it is not trivial to change the parameters of the tank circuit, such as the resonator's frequency ν_R. Conveniently, the axial frequency ν_z of the ion depends on the trapping voltage according to equation (3.5). That way, the quadrupole trapping potential can be adjusted by the voltage on the trap electrodes, which shifts the axial frequency of the ion accordingly. Like this, the ion is brought into resonance with the (fixed) resonator frequency ν_R.

Due to the oscillation of the ion in the axial direction, the induced image current back-acts on the ion's motion. This is expressed by an extra damping term in the equation of motion, leading to

$$\ddot{z} + \frac{q^2 Re(Z(\omega))}{m D_\mathrm{eff}} \dot{z} + \omega_\mathrm{z}^2 z = 0, \tag{4.4}$$

with $\frac{q^2 Re(Z(\omega))}{m D_\mathrm{eff}}$ being the damping constant.

Resitive cooling

When the ion is in contact with the resonator, and its axial frequency is the same as the resonator, it would initially appear as a peak on top of the resonator. The amplitude of the peak depends on the excess of axial energy of the ion, compared to the thermal noise of the resonator. In resonance, power

$$P = I_\mathrm{ind}^2 \cdot R \tag{4.5}$$

is dissipated on the tank circuit, leading to the ion's resistive cooling. The axial energy is reduced exponentially $\propto e^{-t/\tau}$ with the cooling time constant

$$\tau = \frac{m}{q^2} \frac{D_\mathrm{eff}^2}{Re(Z(\omega))} = \frac{m}{q^2} \frac{D_\mathrm{eff}^2}{R}, \tag{4.6}$$

until thermal equilibrium is reached. The cooling time constant for an $^{40}\mathrm{Ar}^{13+}$ ion on the axial detector of our precision trap is about $\tau \approx 40\,\mathrm{ms}$.

Dip detection

After a few cooling time constants, thermal equilibrium is reached between the ion and the electron plasma of the resonator which in turn is in thermal equilibrium with the bulk of the resonator as well as possible excess noise originating e.g. from the cryogenic amplifier. The bulk of the resonator is cooled to $4.2\,\mathrm{K}$. At thermal equilibrium the trapped ion is equivalent to a series LC circuit with parameters:

$$L_{ion} = \frac{mD_{\mathrm{eff}}^2}{q^2}, \tag{4.7}$$

$$C_{ion} = \frac{q^2}{m\omega_{ion}^2 D_{\mathrm{eff}}^2}. \tag{4.8}$$

The spectral noise is calculated using the real part of the total impedance of the ion and the resonator. The resulting spectrum is the characteristic dip which is shown in figure 4.2. There, the ion when oscillating at the same frequency as the resonator, $\omega_{\mathrm{z}} = \omega_{\mathrm{R}}$ it shorts the thermal noise of the resonator and the noise signal drops to the background noise level. The line shape that describes the ion-resonator interaction is

$$u_{\mathrm{res}}(\omega) = 10\log_{10}\left(A_{\mathrm{off}}^2 + \frac{A\cdot R}{1+(Q(\frac{\omega}{\omega_{\mathrm{R}}} - \frac{\omega_{\mathrm{R}}}{\omega}) - \frac{\omega}{\omega'})^2}\right) + \theta\cdot(\omega - \omega_{\mathrm{R}}), \tag{4.9}$$

where

$$\omega' = \tau(\omega^2 - \omega_{\mathrm{z}}^2). \tag{4.10}$$

From the above expression it is easy to notice that when $\omega = \omega_{\mathrm{z}}$ the denominator goes to infinity and thus the second term in (4.9) is nulled. That forces the noise spectrum to sharply drop to the background noise level, creating a dip. It is also interesting to note, that if there were no background noise and if the ion would be infinitely stable, the spectrum noise would go to $-\infty$ in logarithmic units.

Image charge shift

The presence of an ion inside the trap induces image charges on the electrodes' surfaces. Those image charges create an electrostatic field $\vec{E}_{IC}$ which creates a force $\vec{F} = q\vec{E}_{IC}$ and adds an extra term in the equation of motion. That effect leads to a systematic shift of the eigenfrequencies. The shift affects mostly the radial modes while due to the axial symmetry the axial mode is shifted by a much smaller amount. In fact, in a perfect cylinder there would be no shift of the axial frequency while in a real cylindrical trap there exists a small shift of ν_{z} due to, e.g., the slits that break the axial symmetry. The image charge shift has been approximated analytically [60] and semi-analytically [55] for the cylindrical Penning trap of the

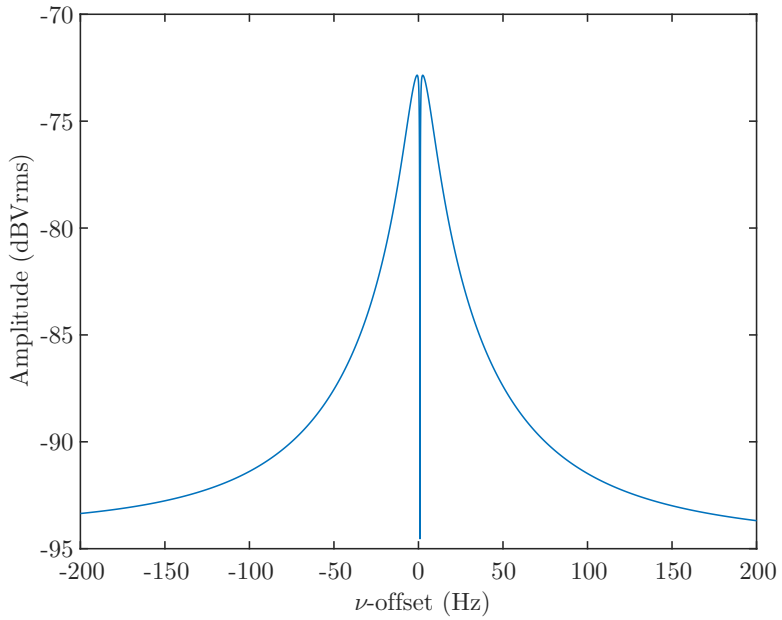

Fig. 4.2: Simulation of the characteristic dip signal of a single $^{40}Ar^{13+}$ ion on the axial detector of the precision trap.

Mainz *g*-factor experiment on highly charged ions. Furthermore, this effect has been experimentally determined and calculated numerically [61], among others, for the LIONTRAP experiment. The frequencies shifts according to [61]:

$$\Delta\nu_{\pm} = \mp n\frac{\mathcal{E}_{\mathrm{r}}}{2\pi B_0} \tag{4.11}$$

$$\Delta\nu_{\mathrm{z}} = -n\frac{q}{m}\frac{\mathcal{E}_{\mathrm{z}}}{8\pi^2\nu_{\mathrm{z}}}, \tag{4.12}$$

where n is the charge state of the ion, q/m is the ion's charge-to-mass ratio, and $\mathcal{E}_r$ and $\mathcal{E}_{\mathrm{z}}$ are the linear field gradients of the radial and the axial component of the electric field $\vec{E}_{IC}$, respectively. The numerical factor $\mathcal{E}_{\mathrm{r}} \propto e/4\pi\varepsilon_0 r^3$, where ε_0 is the vacuum permittivity and r is the trap radius, is given in units of $\mathrm{V/m}^2$ and is numerically calculated using COMSOL for the specific geometry of the trap in consideration, in the case of ALPHATRAP including the vertical slits of the half-split electrodes. The corresponding shift of the free-space cyclotron frequency is given by

$$\Delta\nu_c \approx n\frac{2\mathcal{E}_{\mathrm{r}} + \mathcal{E}_{\mathrm{z}}}{4\pi B_0} \approx n\frac{\mathcal{E}_{\mathrm{r}}}{2\pi B_0}, \tag{4.13}$$

which leads to the relative shift of the free-space cyclotron frequency

$$\frac{\Delta\nu_c}{\nu_c} \approx \frac{m\mathcal{E}_{\mathrm{r}}}{eB_0^2}. \tag{4.14}$$

This systematic effect has been the limiting factor for previous high-precision measurements, since it contributed the largest systematic uncertainty. It becomes obvious from equation (4.14) that the shift is increased for heavier ion masses. The image charge shift can only be reduced by increasing the trap radius, which is the case for the ALPHATRAP precision trap where, for the current precision level, the shift of an $^{40}Ar^{13+}$ ion is negligible.

Frequency pulling

The interaction of the ion with the tank circuit leads to the formation of a dip signal on the thermal noise spectrum of the resonator which enables detecting the ion's frequency by considering the circuit's total impedance. The real part of the impedance has an insignificant effect on the frequency of the ion. However, the imaginary part of the impedance can create and effective potential as described in Refs. [62, 55], which leads to a frequency shift. This shift can be minimised for when the ion is exactly at resonance with the tank circuit or when the resonator's frequency is sufficiently far from the ion's frequency.

The frequency pulling due to the axial tank circuit which is on resonance with ν_z is corrected for by the dip line shape described in equation (4.9). The cyclotron resonator however, is detuned from the ions modified cyclotron frequency and it gives rise to a relative shift of the modified cyclotron frequency according to [62, 55]:

$$\frac{\Delta\nu_+}{\nu_+} \approx -\frac{Q}{\tau_+}\frac{\omega_R - \omega_+}{\omega_+^2 + 4Q^2(\omega_R - \omega_+)^2}, \tag{4.15}$$

where τ_+ is the cooling time constant of the modified cyclotron mode in resonance. This effect of the frequency being shifted by the resonator is commonly referred to as *frequency pulling* or as *the image current effect*.

4.3 Axial frequency detection

The axial frequency can be obtained when fitting the noise spectrum of the ion in resonance with the tank circuit, using equation (4.9) with ν_z as a free parameter. The dip signal (shown in Fig. 4.2) is characterised by its width at the $-3\,\mathrm{dB}$ level, the so-called *dip width*:

$$\Delta\nu_z(N) = \frac{N}{2\pi}\frac{1}{\tau} \tag{4.16}$$

with N being the number of ions of the same species and τ is given in equation (4.6). For a single $^{40}Ar^{13+}$ the dip width is about $4.2\,\mathrm{Hz}$.

The *dip detection* technique, as described in section 4.2, is used for detecting the ion's frequency in thermal equilibrium with the resonator. The typically low temperatures of about $4.2\,\mathrm{K}$ correspond to small thermal amplitudes of the modes (about $10\,\mu\mathrm{m}$ for the axial motion). Therefore, the effect of systematic shifts due to

imperfections of the trapping fields, to the image charge shift and to shifts due to patch potentials are highly suppressed during the dip detection. However, the long measurement time ($\sim 85\,\mathrm{s}$) that is required for resolving the dip signal during FFT analysis makes the measurement of the axial frequency prone to fluctuations of the trapping potentials.

4.4 Radial frequency detection - Double dip

In principle the modified cyclotron mode can be measured by using the induced image charges as described in section 4.1. By use of the half-split ring and correction electrodes, the induced charges can be detected with a dedicated cyclotron resonator connected to those half-electrodes. That way ν_+ can be measured as well as resistively cooled.

Even though such a cyclotron detector is attached to the ALPHATRAP precision trap, it was not used until now. By means of a cyclotron resonator the temperature of the modified cyclotron mode can be cooled down to $4.2\,\mathrm{K}$. Due to the fact that ν_+ cannot be shifted by changing the trapping voltage the resonance frequency of the tank circuit has to be adjusted to match the modified cyclotron frequency. Even though the target frequency is planned carefully for the specific charge-to-mass ratio before the experiment is cooled down, there will always be a shift of the resonator's frequency at cryogenic temperatures. For that reason, the cyclotron resonator is equipped with a varactor diode which allows for tuning the resonator's frequency within a range of about $500\,\mathrm{kHz}$. During the course of the measurement campaign presented in this thesis, the cyclotron resonator's frequency range did not overlap with the modified cyclotron frequency of boronlike argon.

Instead, the axial detector is used also for measuring the radial eigenfrequencies of the ion by use of the *double-dip technique*. For the determination of ν_+ a quadrupole excitation $\mathrm{Q_{xz}}$ is applied on the red sideband with frequency $\nu_\mathrm{rf} = \nu_+ - \nu_z$. This excitation field has the form:

$$E_\mathrm{Qxz} = \frac{V_\mathrm{Qxz}}{D^2_\mathrm{eff,xz}}(\cos\omega_\mathrm{rf}t + \phi_\mathrm{rf}) \begin{pmatrix} z \\ 0 \\ x \end{pmatrix}, \tag{4.17}$$

where V_Qxz is the applied voltage and $D_\mathrm{eff,xz}$ is the effective electrode distance of the first upper correction electrode, which is a half-split electrode. By coupling this radiofrequency field to the ion's motion the modified cyclotron mode is coupled to the axial mode. Equivalently to a two-level system interacting with a classical field, the two modes are forced into a Rabi oscillation while the quadrupole excitation is applied. At resonant coupling the axial mode is amplitude modulated according to

$$z(t) = z_0 \sin(\omega_z t + \phi_z) \sin\left(\frac{\Omega}{2}t + \phi_\Omega\right)$$
$$= \frac{1}{2}\left[\cos\left(2\pi\left(\nu_z - \frac{\nu_\Omega}{2}\right)t + \phi'\right) - \cos\left(2\pi\left(\nu_z + \frac{\nu_\Omega}{2}\right)t + \phi''\right)\right], \tag{4.18}$$

where at $t = 0$ the axial amplitude $z = z_0 = 0$, $\nu_\Omega = \Omega/2\pi$, $\phi' = \phi_z - \phi_\Omega$, $\phi'' = \phi_z + \phi_\Omega$ and ϕ_z, ϕ_Ω are arbitrary initial phases. When the modes are coupled, energy is transferred between the two modes with the Rabi frequency Ω, which depends on the coupling strength of the field. When the two modes are coupled, the axial state is dressed with the modified cyclotron state and the two dressed states are coupled to the axial tank circuit and thus resistively cooled. Therefore, while the modified cyclotron mode is coupled to the axial mode excessive energy of ν_+ is dissipated on the axial resonator. After a few cooling time constants, both modes are resistively cooled and are in thermal equilibrium with the detector. Thus their quantum numbers $\langle n_z \rangle$ and $\langle n_+ \rangle$ are equal, leading to the energy relation [50]:

$$\langle E_+ \rangle = h\nu_+\left(\langle n_+ \rangle + \frac{1}{2}\right) = \frac{\nu_+}{\nu_z} h\nu_z \left(\langle n_z \rangle + \frac{1}{2}\right) = \frac{\nu_+}{\nu_z}\langle E_z \rangle . \tag{4.19}$$

Similarly, the magnetron mode can be cooled at the upper sideband, when a quadrupole excitation is applied with frequency $\nu_{rf} = \nu_z + \nu_-$. At thermal equilibrium, the expectation value of the energy of magnetron mode reads:

$$\langle E_- \rangle = -\frac{\nu_-}{\nu_z}\langle E_z \rangle . \tag{4.20}$$

Due to the fact that the magnetron mode is metastable and exhibits negative energy (equation (3.13)), cooling this mode is only possible with sideband coupling at the upper sideband. Decreasing the mode's energy via direct resistive or laser cooling would increase the magnetron radius and lead to ion loss. With the appropriate coupling frequency, both radial modes can be resistively cooled via the axial resonator and thus also become thermally distributed. Consequently, the temperatures of the radial modes can be written as

$$T_+ = \frac{\nu_+}{\nu_z} T_z \quad \text{and} \quad T_- = -\frac{\nu_-}{\nu_z} T_z. \tag{4.21}$$

Sideband coupling is therefore used for temperature measurements, as will be discussed in section 6.7.

After the modes are cold they can be detected via the characteristic *double-dip* signal. During continuous irradiation of a Q_{xz} wave with $\nu_{rf} = \nu_+ - \nu_z$, the modified cyclotron frequency can be determined. According to equation (4.18) the initial axial dip is split into two dips as shown in Fig. 4.3.

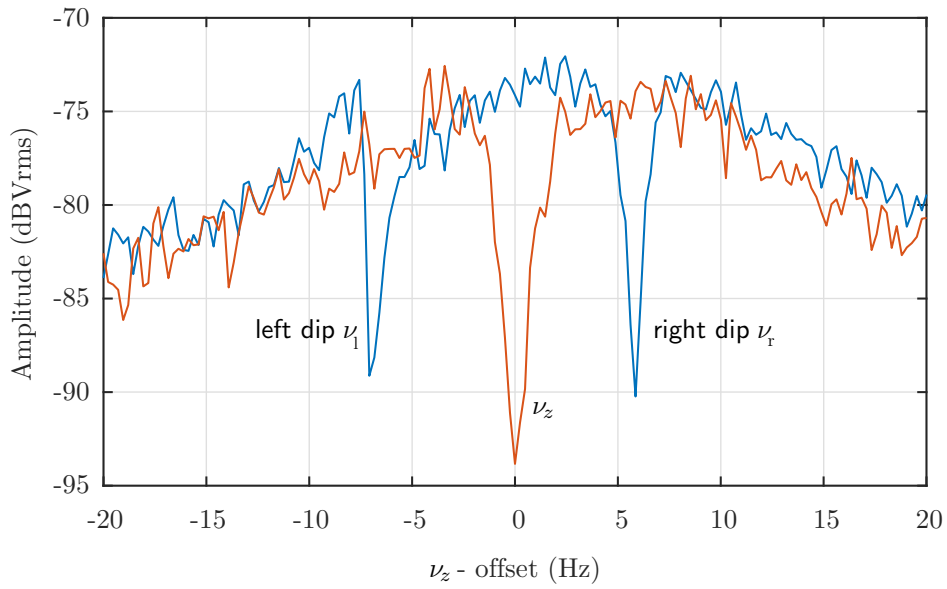

Fig. 4.3: Sideband coupling at $\nu_{rf} = \nu_+ - \nu_z$. In red, the typical axial dip with ν_z of the ion when no coupling is applied is shown. In blue the double dip is plotted, with the frequencies of the *left* (ν_l) and *right* (ν_r) dips indicated in the figure. The width of each dip of the double dip is half the width of the single axial dip, when the coupling is exactly resonant.

The frequencies of the *left* and *right* dips are given by

$$\nu_l = \nu_z - \frac{\nu_\Omega}{2}, \tag{4.22}$$

$$\nu_r = \nu_z + \frac{\nu_\Omega}{2}, \tag{4.23}$$

where ν_l and ν_r are the frequencies of the left and right dip, respectively. Assuming a non-perfectly resonant coupling rf drive, the double-dip splitting is no longer symmetric around the axial single dip. Rather, the two dips show an avoided crossing behavior, which can be seen in figure 4.4. There, the *left*, *right* and non-coupled axial dip are shown. The frequency of each dip is recorded for different coupling frequencies ν_{rf} within a frequency range of $\pm 20\,\mathrm{Hz}$.

For a small detuning δ around the coupling frequency such that $\nu_{rf} = \nu_+ - \nu_z + \delta$, the Rabi frequency becomes [63]

$$\nu_{\Omega 0} = \sqrt{\nu_\Omega^2 + \delta^2} \tag{4.24}$$

and the ion oscillates at the axial mode with frequency components

$$\nu = \nu_z - \frac{\delta}{2} \pm \frac{1}{2}\sqrt{\delta^2 + \nu_{\Omega 0}^2}. \tag{4.25}$$

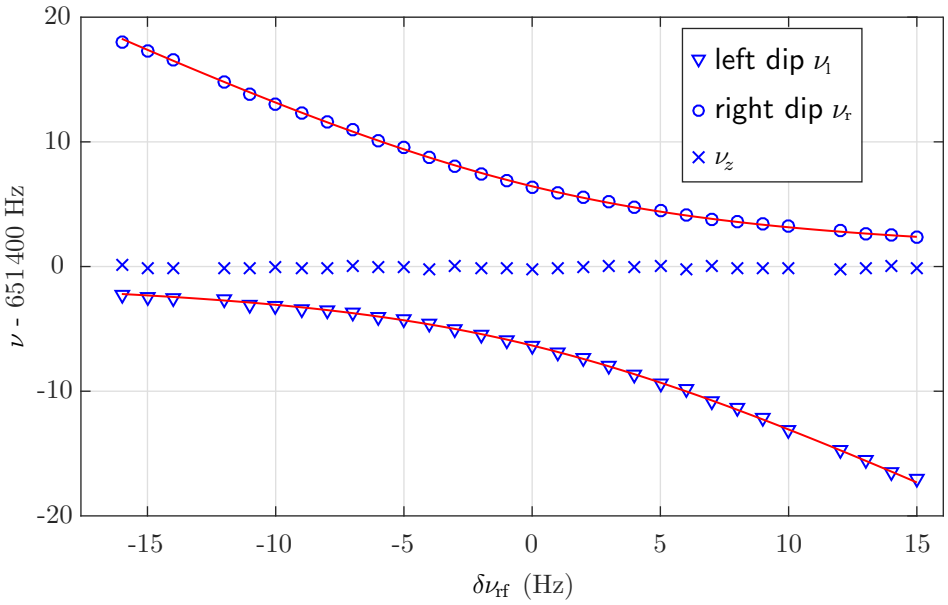

Fig. 4.4: Avoided crossing of the left and right dip (see Fig. 4.3) due to coupling of the axial and modified cyclotron modes using the the sideband $\nu_+ - \nu_z$. The axial frequency ν_z is independently measured after each sideband coupling measurement. The fit (red line) is according to equation (4.25) in [63].

The modified cyclotron frequency can thus be obtained by use of

$$\nu_+ = \nu_r + \nu_l - \nu_z + \nu_{rf}, \tag{4.26}$$

which is exact within the rotating wave approximation. Here, the axial frequency ν_z is measured independently when the rf drive is off. During the *g*-factor measurement and in order to account for drifts of the axial frequency during the double-dip measurement due to the trapping potential, ν_z is measured before and after the sideband coupling of the reduced cyclotron mode to the axial mode (see sections 7.1 and 7.3.1).

In the same way, the magnetron frequency is determined using the *double-dip technique*, when the magnetron frequency is coupled to the axial one via the sideband frequency $\nu_{rf} = \nu_z + \nu_-$ which leads to the following relation:

$$\nu_- = \nu_{rf} + \nu_z - \nu_r - \nu_l. \tag{4.27}$$

The line shape of the double-dip is described by

$$u_{res}(\omega) = 10\log_{10}\left(A_{off}^2 + \frac{A \cdot R}{1 + (Q(\frac{\omega}{\omega_R} - \frac{\omega_R}{\omega}) - \frac{\omega}{\omega_1} - \frac{\omega}{\omega_2})^2}\right) + \theta \cdot (\omega - \omega_R) \tag{4.28}$$

$$\text{where } \omega_1 = \tau_l(\omega^2 - \omega_l^2) \text{ and } \omega_2 = \tau_r(\omega^2 - \omega_r^2),$$

with ω_l and ω_r being the frequencies of the left and the right dip, respectively. Fitting the data with the frequencies of the left and right dip as free parameters, allows for determining the radial modes' frequencies. In that way, all three eigenfrequencies are measured. The axial frequency ν_z is measured directly with the *dip technique* and the two radial modes are measured via the *double-dip technique*. Therefore, the free-space cyclotron frequency ν_c can be obtained by use of the invariance theorem given in equation (3.11).

Instead of using the double-dip technique to measure the modified cyclotron frequency a phase sensitive detection scheme can be used alternatively, the so called *Pulse and Amplify* (PnA). This technique has been developed by Sven Sturm and is detailed in Refs. [64, 55]. When coupling ν_+ and ν_z on the upper sideband with a coupling frequency $\nu_\mathrm{rf} = \nu_+ + \nu_\mathrm{z}$ the modes' amplitudes increase exponentially. At the same time the motional phase can be transferred from one mode to the other. The PnA detection scheme provides with a higher precision than the double-dip and is planned to be implemented at ALPHATRAP for the upcoming measurement campaigns. During the course of this thesis the PnA detection was not necessary, the double-dip technique was sufficient for the current level of precision.

4.5 Larmor frequency detection

The experimental determination of the g-factor as explained in section 2.4, requires measuring the frequency ratio $\Gamma = \frac{\nu_\mathrm{L}}{\nu_c}$. So far, the measurement principle of ν_c has been introduced. Those techniques cannot be applied in determining the spin precession frequency ν_L since it does not induce image charges on the electrodes. Instead, the Larmor frequency is deduced by probing the Zeeman transition between two states. For this, the *Continuous Stern-Gerlach effect* [65] is employed, which was first introduced by Hans Dehmelt [66] and allows for spin-state determination. By introducing a strong magnetic field inhomogeneity which modifies the magnetic field B_0 as follows:

$$B_\mathrm{z}(z,r) = B_0 + B_2(z^2 - \frac{r^2}{2}), \tag{4.29}$$

the axial frequency couples to the magnetic moment

$$\mu_\mathrm{z} = -g\mu_\mathrm{B}S_\mathrm{z}/\hbar, \tag{4.30}$$

where $\mu_\mathrm{B} = e\hbar/(2m_\mathrm{e})$ is the Bohr magneton, $S_\mathrm{z} = \pm\frac{1}{2}\hbar$ the magnetic quantum number and $\hbar = h/2\pi$ is the reduced Planck constant. This magnetic field configuration is often referred to as *magnetic bottle*. That way, an additional force is introduced in the z-direction

$$F_\mathrm{z} = -\nabla_\mathrm{z}(\mu_\mathrm{z}B_\mathrm{z}) = \mp g\mu_\mathrm{B}B_2 z, \tag{4.31}$$

which leads to the following equation of motion:

$$\ddot{z} + \left(\omega_{z0}^2 \pm \frac{g\mu_B B_2}{m}\right) z = 0 \tag{4.32}$$

and couples the axial frequency of the ion with the spin direction of the valence electron. The axial frequency thus becomes

$$\omega_z \approx \omega_{z0} \pm \frac{g\mu_B B_2}{2m\omega_{z0}}. \tag{4.33}$$

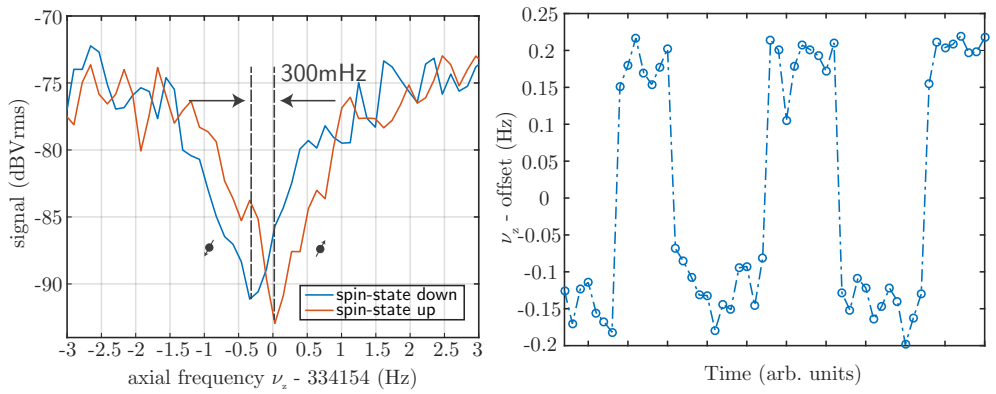

Fig. 4.5: (left) Axial frequency shift in the analysis trap due to a spin flip. After the injection of mm-waves, the dip signal shifts by about 300 mHz. (right) Several consecutive axial dip measurements where the spin orientation has been changed from spin-down to spin-up and *vice versa* a few times. The stability of the axial frequency allows for unambiguous spin-state determination.

Therefore, when introducing mm-waves with frequency close to the Larmor frequency ν_L, the spin state can be changed. Within a magnetic bottle configuration this quantum jump between the two spin states, the so-called *spin flip*, is translated into a small shift of the ion's axial frequency as

$$\Delta\nu_z = \pm\frac{g\mu_B B_2}{m4\pi^2\nu_z}, \tag{4.34}$$

which can be measured. The magnetic field inhomogeneity is characterised by the B_2 coefficient and is created by a dedicated ring electrode of our analysis trap, and it has been measured to be $B_2 = 44.35(84)\,\mathrm{kT/m^2}$, as discussed in section 6.5. A spin flip of a $^{40}Ar^{13+}$ in our setup corresponds to a shift of about 300 mHz out of 335 kHz, and is shown in Fig. 4.5.

The detection of such a shift requires a stable enough trapping voltage as discussed in section 5.1.2 and at the same time minimising the effect of possible external heating sources of the modified cyclotron mode. A change in E_+ due to noise or insufficient cooling of the mode would lead to unwanted ν_z shifts in the analysis trap due to the strong magnetic bottle configuration. Explicit spin-state determination becomes increasingly challenging with the mass of the ion. Even more so for the

case of heavy boronlike ions such as $^{208}Pb^{77+}$, with an expected axial frequency shift due to a spin flip in the order of only $54\,\mathrm{mHz}$.

4.6 Magnetic moment dynamics

With the continuous Stern-Gerlach effect the spin state of the particle can be probed and thus the Larmor frequency can be determined. The latter is obtained after several attempts to induce a spin flip in the precision trap with mm-waves with different frequencies ν_{MW} within a range of frequencies that includes ν_L. In the case of boronlike argon, the relative precision of the theoretical g-factor is in the order of 10^{-6}, which would make it tedious to find a 10^{-8} resonance within reasonable measurement time scales. For this reason the appropriate range for ν_{MW} has been defined by means of the adiabatic rapid passage (ARP) method, a technique novelly implemented in a high-precision Penning-trap experiment.

In this section the dynamics of the system are described starting from the simple precession of the magnetic moment in a static field in the laboratory frame (LF), when a transformation to the rotating frame (RotF) is applied and with the injection of mm-waves. Finally the principle of rapid adiabatic passage and how this has been implemented, for the first time, in a Penning-trap setup is discussed at the end of the section.

The classical dynamics of $\vec{\mu}$ is being discussed. For the case of a two-level spin system the classical solution is exactly identical to the quantum mechanical treatment. In the following discussion the classical results are used to derive some quantum-mechanical quantities, such as the Rabi frequency Ω_R and the spin-flip probability P_SF.

4.6.1 Magnetic moment in the laboratory frame (LF)

A magnetic moment $\vec{\mu}$ that precesses around a static homogeneous magnetic field is described by the interaction energy $V = -\vec{\mu}\vec{B}_0$, the force $\vec{F} = -\vec{\nabla}\cdot V$ which is zero in a homogeneous field, and the torque $\vec{T} = \vec{\mu}\times\vec{B}_0$. This results in a change of the angular momentum $\vec{L}$ which we define as $\vec{L} = \frac{1}{\gamma}\vec{\mu}$. This change is described by

$$\left(\frac{d}{dt}\right)_\mathrm{LF}\vec{L} = \gamma\vec{L}\times\vec{B}_0 = \vec{T}, \tag{4.35}$$

where γ is the gyromagnetic ratio and it is $\gamma = \frac{ge}{2m_\mathrm{e}}$ for our system. Equation (4.35) describes a pure precession of the angular momentum (or $\vec{\mu}$) around $\vec{B}_0$, as shown in Fig. 4.6(left). That means that $|\vec{\mu}|$ is constant and is rotating around $\vec{B}_0$ with a constant angular velocity, which is called the Larmor frequency:

$$\vec{\Omega}_\mathrm{L} = -\gamma\vec{B}_0. \tag{4.36}$$

4.6.2 Magnetic moment in the rotating frame (RotF)

Here we consider the same system in the rotating frame. For a vector $\vec{A}$ any change in the LF can be expressed by a change in the RotF as

$$\left(\frac{d}{dt}\right)_{\mathrm{LF}} \vec{A} = \left(\frac{d}{dt}\right)_{\mathrm{RotF}} \vec{A} + \vec{\Omega} \times \vec{A}, \tag{4.37}$$

with $\vec{\Omega}$ being the rotational frequency of RotF. Applying this to the angular momentum we get:

$$\left(\frac{d}{dt}\right)_{\mathrm{RotF}} \vec{L} = \left(\frac{d}{dt}\right)_{\mathrm{LF}} \vec{L} - \vec{\Omega} \times \vec{L}. \tag{4.38}$$

From equations (4.35) and (4.38) we obtain:

$$\begin{aligned}\left(\frac{d}{dt}\right)_{\mathrm{RotF}} \vec{L} &= \gamma \vec{L} \times \vec{B}_0 - \vec{\Omega} \times \vec{L} \\ &= \gamma \vec{L} \times (\vec{B}_0 + \vec{\Omega}/\gamma).\end{aligned} \tag{4.39}$$

Comparing equation (4.39) to the dynamics of $\vec{L}$ in the lab frame given in equation (4.36), it is shown that in the rotating frame the magnetic field $\vec{B}_0$ is replaced by an effective magnetic field $\vec{B}_{\mathrm{eff}}$ and thus in the rotating frame the magnetic moment precesses around the effective magnetic field

$$\vec{B}_{\mathrm{eff}} = \vec{B}_0 + \frac{\vec{\Omega}}{\gamma} = \vec{B}_0 + \vec{B}_{\mathrm{RotF}}, \tag{4.40}$$

as illustrated in Fig. 4.6(right). The additional field $\vec{B}_{\mathrm{RotF}}$ is a pseudo magnetic field that arises from the frame transformation.

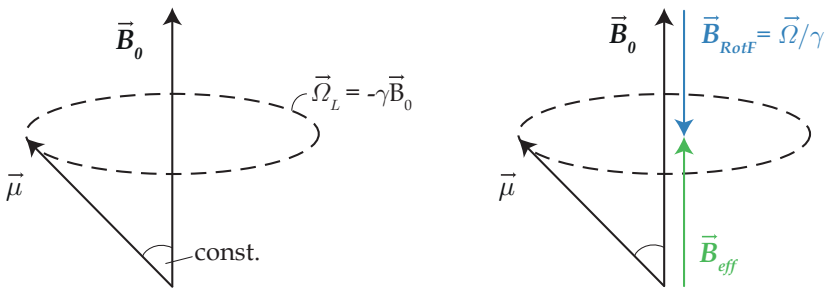

Fig. 4.6: (left) Illustration of the magnetic moment precession with frequency $\vec{\Omega}_{\mathrm{L}}$ around a static magnetic field $\vec{B}_0$, in the frame of the laboratory. (right) The same precession depicted in the rotating frame where the magnetic moment precesses around the effective magnetic field $\vec{B}_{\mathrm{eff}}$

The interesting case is when the RotF rotates with the Larmor frequency $\vec{\Omega} = \vec{\Omega}_{\mathrm{L}}$. In this case:

$$\vec{B}_{\mathrm{RotF}} = \frac{\vec{\Omega}_{\mathrm{L}}}{\gamma} = -\vec{B}_0, \tag{4.41}$$

which means that $\dot{\vec{L}}_{\mathrm{RotF}} = 0$, $\vec{L}$ does not change in the rotating frame.

4.6.3 mm-wave injection

So far only the interaction of $\vec{\mu}$ with a stationary magnetic field has been considered. We now investigate how the magnetic moment behaves when an additional rotating magnetic field is introduced.

When mm-waves are injected a rotating magnetic field $\vec{B}_{\mathrm{mmW}} = B_{\mathrm{mmW}}(\hat{x}\sin(\omega t) + \hat{y}\cos(\omega t))$ is introduced to the system[1]. This field rotates with a frequency ω in the frame of the laboratory. As already mentioned, in resonance $\omega = \Omega_{\mathrm{L}}$ and $\vec{B}_{\mathrm{RotF}} = -\vec{B}_0$. That leads to

$$\vec{B}_{\mathrm{eff}} = \vec{B}_0 + \vec{B}_{\mathrm{RotF}} + \vec{B}_{\mathrm{mmW}} = \vec{B}_{\mathrm{mmW}}, \tag{4.42}$$

and is demonstrated in Fig. 4.7(left). This means that in the RotF and in resonance the field in the z-direction is cancelled out and the only remaining field is the field of the mm-waves $\vec{B}_{\mathrm{mmW}}$. Consequently $\vec{\mu}$ is precessing around $\vec{B}_{\mathrm{mmW}}$ with a frequency

$$\Omega_{\mathrm{SF}} = \gamma B_{\mathrm{mmW}} = \omega_{\mathrm{R}}, \tag{4.43}$$

which is the Rabi frequency on resonance or the spin-flip frequency.

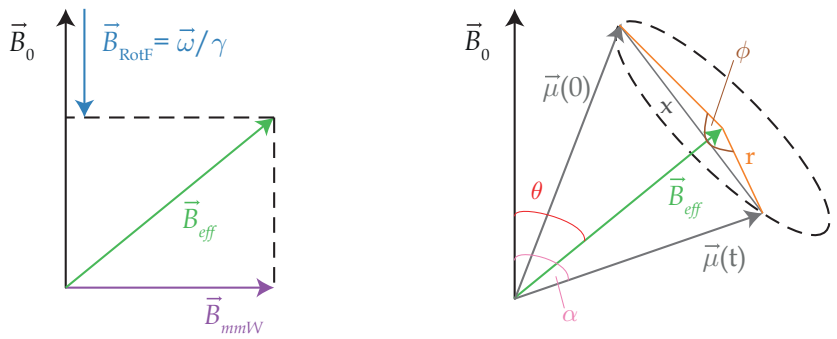

Fig. 4.7: (left) The effective magnetic field in the RotF during mm-wave irradiation with frequency ω. (right) The magnetic moment precesses around the effective magnetic field $\vec{B}_{\mathrm{eff}}$. On resonance the angle θ is 90°.

In the off-resonant case the RotF and $\vec{B}_{\mathrm{mmW}}$ are not rotating with the Larmor frequency. They rotate with a frequency $\omega \neq \Omega_{\mathrm{L}}$ and the effective magnetic field is

$$\vec{B}_{\mathrm{eff}} = \vec{B}_0 - \frac{\vec{\omega}}{\gamma} + \vec{B}_{\mathrm{mmW}}, \tag{4.44}$$

[1] In our case the field is linearly polarised since it is transmitted via a rectangular waveguide as will be discussed in section 4.6.5.

which leads to

$$|\vec{B}_{\text{eff}}| = \sqrt{B_{\text{mmW}}^2 + \left(B_0 - \frac{\omega}{\gamma}\right)}, \tag{4.45}$$

where we assume that $\vec{B}_{\text{mmW}} \perp \vec{B}_0$, as shown in Fig. 4.7(left). Therefore the magnetic moment μ precesses around the magnetic field $\vec{B}_{\text{eff}}$ with the generalised Rabi frequency

$$\Omega_{\text{R}} = \gamma B_{\text{eff}} = \sqrt{\gamma^2 B_{\text{mmW}}^2 + (\gamma B_0 - \omega)^2} = \sqrt{\omega_{\text{R}}^2 + (\Omega_{\text{L}} - \omega)^2}, \tag{4.46}$$

where $(\omega_{\text{L}} - \omega)$ is the frequency detuning. In order to study the spin-flip dynamics we are interested in the dynamics of the magnetic moment $\vec{\mu}(t)$, specifically the z-component of the magnetic moment $\mu_{\text{z}}(t)$. From Fig. 4.7(right) the following relations are obtained:

$$r = \mu \sin\theta = \mu \frac{\omega_{\text{R}}}{\Omega_{\text{R}}}, \tag{4.47}$$

$$\mu_{\text{z}}(t) = \mu \cos\alpha, \tag{4.48}$$

$$x^2 = 2\mu^2(1 - \cos\alpha), \tag{4.49}$$

$$x^2 = 2r^2(1 - \cos\phi). \tag{4.50}$$

From equations (4.49) and (4.50) we obtain:

$$\mu_{\text{z}} t = \mu\left(1 - 2\left(\frac{\omega_{\text{R}}}{\Omega_{\text{R}}}\right)^2 \sin^2\left(\frac{\Omega_{\text{R}} t}{2}\right)\right). \tag{4.51}$$

The spin-flip probability is given by

$$P_{\text{SF}}(t) = \frac{\mu_{\text{z}}(0) - \mu_{\text{z}}(t)}{2\mu_{\text{z}}(0)} \tag{4.52}$$

$$= \left(\frac{\omega_{\text{R}}}{\Omega_{\text{R}}}\right)^2 \sin^2\left(\frac{\Omega_{\text{R}} t}{2}\right). \tag{4.53}$$

This means that turning off the drive field $\vec{B}_{\text{mmW}}$ after $t = \pi/\Omega_{\text{R}}$ will lead to an inversion of the direction of $\vec{\mu}$. This is known as "π-pulse". In our experiment however, the fluctuations of the magnetic field for low ω_{R} do not allow for a π-pulse therefore we estimate the average of the probability over one period:

$$\langle P_{\text{SF}} \rangle = \frac{1}{2\pi} \int_0^{2\pi} \left(\frac{\omega_{\text{R}}}{\Omega_{\text{R}}}\right)^2 \sin^2(\beta) d\beta \tag{4.54}$$

$$= \frac{1}{2}\left(\frac{\omega_{\text{R}}}{\Omega_{\text{R}}}\right)^2. \tag{4.55}$$

From equations (4.55) and (4.46) we obtain the spin-flip probability as a function of the mm-wave frequency:

$$\langle P_{\mathrm{SF}} \rangle = \frac{\omega_{\mathrm{R}}^2}{2(\omega_{\mathrm{R}}^2 + (\Omega_{\mathrm{L}} - \omega)^2)}, \tag{4.56}$$

which is a Lorentzian distribution and exhibits a maximum of 0.5.

4.6.4 Adiabatic rapid passage (ARP)

Until now the injected field $\vec{B}_{\mathrm{mmW}}$ was assumed to be rotating at a constant frequency, where the maximum spin-flip probability is 0.5 even if we perfectly guess Ω_{L}, in the case that coherency is removed by the magnetic field fluctuations. Now we introduce the adiabatic rapid passage method, a technique with which $P_{\mathrm{SF}} = 1$ can be realised. Once again the dynamics is discussed in the classical framework. The quantum mechanical equivalent of ARP is a Landau-Zener transition [67, 68].

Considering now a change in the frequency of the injected field, we introduce the ARP technique. This technique is used to invert the direction of the magnetic moment (spin flip) by means of a frequency sweep of the drive field across the resonance frequency, with the sweep starting from a value far off-resonance. For a successful ARP the frequency sweep, or the rotation of the effective field, needs to be slower than the Larmor frequency:

$$\Omega_{\mathrm{R}} = \gamma B_{\mathrm{eff}} \ll \dot{\theta}, \tag{4.57}$$

where θ is the angle between B_{eff} and B_0, as shown in Fig. 4.7. For a magnetic moment that precesses around a static field $\vec{B}_0$ we assumed that the drive field $\vec{B}_{\mathrm{mmW}}$ is much smaller than the static field. For the case where $\omega \ll \gamma B_0$, the angle θ and the field $\vec{B}_{\mathrm{RotF}}$ are so small that the drive field is considered as perturbative and the effective magnetic field is (almost) aligned with the z-direction. The magnetic moment is assumed to be aligned with $\vec{B}_{\mathrm{eff}}$ and thus for a small angle θ the magnetic moment is tightly coupled to the effective field. Therefore, the fast-precessing $\vec{\mu}$ will follow $\vec{B}_{\mathrm{eff}}$ with a constant angle θ as long as the rotation of the effective field is slow enough.

Once the sweep has reached Ω_{L} the magnetic moment $\vec{\mu}$ is tilted by $\pi/2$ and $\vec{B}_{\mathrm{eff}} = \vec{B}_{\mathrm{mmW}}$ and is pointing towards the x-direction. At this point B_{eff} has its smallest and $\dot{\theta}$ its largest value during the sweep. By continuing the drive frequency sweep through the resonance to frequencies larger than the Larmor frequency $\omega \gg \gamma B_0$, then $B_{\mathrm{RotF}} \gg \gamma B_0$ which leads to the effective field pointing to the $-z$-direction. In that way the direction of $\vec{\mu}$ is changed by π and a spin flip is achieved by means of ARP. Close to resonance the rotation angle of the effective magnetic field is

$$\theta = \frac{\pi}{2} - \frac{B_{\mathrm{z,eff}}}{B_{\mathrm{mmW}}}, \tag{4.58}$$

and the effective field is

$$B_{\mathrm{z,eff}} = B_0 - \frac{\omega(t)}{\gamma}. \tag{4.59}$$

Combining equations (4.57), (4.58) and (4.59) we obtain the condition for adiabaticity:

$$\dot{\theta} = \frac{\dot{\omega}}{\gamma B_{\mathrm{mmW}}} = \frac{\dot{\omega}}{\omega_{\mathrm{R}}} \ll \omega_{\mathrm{R}}, \tag{4.60}$$

which finally leads to

$$|\dot{\omega}| \ll \omega_{\mathrm{R}}^2. \tag{4.61}$$

When this condition is satisfied, and the frequency of the drive field is swept so that from the z-direction it ends up pointing to the opposite direction, a spin flip is performed with a 100% probability. Otherwise, if the direction of $\vec{B}_{\mathrm{eff}}$ changes non-adiabatically the magnetic moment will not remain tightly bound and will start precessing around the field with the new angle θ.

The magnetic field B_0 is sufficiently stable so that magnetic field fluctuations can be ignored. Including the B-field stability in the adiabaticity condition yields

$$\dot{\theta} = -\frac{\dot{B}_0}{B_{\mathrm{mmW}}} + \frac{\dot{\omega}}{\gamma B_{\mathrm{mmW}}}, \tag{4.62}$$

which leads to the condition for the fluctuations of the static magnetic field $\dot{B}_0 \ll \gamma B_{\mathrm{mmW}}^2 \approx 7 \times 10^{-4}\,\mathrm{T/s}$. The stability of our magnetic field is shown in Fig. 5.5.

4.6.5 Adiabatic rapid passage at ALPHATRAP

So far the dynamics of the magnetic moment that precesses around a magnetic field as well as the principle of ARP have been introduced. Some remarks concerning ALPHATRAP and how the ARP has been implemented are discussed here.

- Because the mm-wave generator was not equipped with an appropriate computer-controlled sweeping module, instead in this work a sweep of the static magnetic field B_0 has been performed. In that configuration the drive field B_{RotF} is kept constant while the B_0 is reduced thus the effective field B_{eff} is scanned through resonance, in the same way as discussed previously in section 4.6.4. In other words, instead of changing the frequency of the drive field, we actually change the Larmor frequency.

  In practice this has been achieved by using a set of Helmholtz coils that are placed outside the superconducting magnet. The sweep is performed by modifying the additional field generated by the Helmholtz coils at the position of the ion.

- The transfer efficiency of the injected power has been measured in an offline setup to be about $\eta \approx 8\%$ from the output of the mm-wave generator to the end of the mm-wave guide. Assuming that the transfer efficiency is the same after the mm-wave setup has been installed at the ALPHATRAP setup, the power that is injected on the particle in the center of the precision trap is

$$P_{\mathrm{mmW}} = \eta P'_{\mathrm{mmW}}, \tag{4.63}$$

where P'_{mmW} is the power set on the mm-wave generator. Assuming a plane wave for the injected mm-waves and that there are no intensity losses from the principal mode to other modes, the power of the drive field is given by

$$P_{\mathrm{mmW}} = \frac{1}{2} A c \frac{B^2_{\mathrm{mmW}}}{2\mu_0}, \tag{4.64}$$

where $A = \pi r^2$ with $r = 9\,\mathrm{mm}$ being the trap's radius, c the speed of light, B_{mmW} the magnetic field component of the mm-waves, μ_0 the magnetic permeability of vacuum and the additional 0.5 factor originates from the RWA discussed below. Here it is assumed that the propagation velocity through the cylinder is the speed of light. Furthermore, it is assumed that there are no reflections and therefore that the absorption cone at the end of the cylinder is perfectly absorbing.

During the ARP measurement, a power of $10\,\mathrm{dB}$ was set on the mm-wave generator. Note that during the *g*-factor measurement the power was lower. According to equation (4.64) the field strength is in the order of $B_{\mathrm{mmW}} \approx 1.1 \times 10^{-7}\,\mathrm{T}$ which leads to

$$\omega_{\mathrm{R}} = \gamma B_{\mathrm{mmW}} \approx 2\pi \cdot 1\,\mathrm{kHz}. \tag{4.65}$$

Concerning the interaction of the ion, a plane wave is a good approximation of the flat Gaussian profile which is adiabatically enlarged when travelling from the AT through the much larger PT, especially when considering the small motional amplitudes of the ion. However, for an accurate estimation of the field strength one would need to integrate the Poynting vector over the area. Alternatively, the power can be calibrated by the measured resonance width of the *g*-factor resonance.

- The Lorentzian distribution that describes the spin-flip probability distribution with respect to the mm-wave frequency in equation (4.56) has a FWHM of $2\omega_{\mathrm{R}}$. Therefore the width of the resonance is expected to be in the order of

$$\frac{2\omega_{\mathrm{R}}}{2\pi\nu_{\mathrm{L0}}} = \frac{\gamma B_{\mathrm{mmW}}}{\pi\nu_{\mathrm{L0}}} \sim 10^{-8}. \tag{4.66}$$

- The ARP technique reduced significantly the measurement time that would be required to find the resonance prior to the *g*-factor measurement campaign. The relative precision of the theoretical *g*-factor in the order of 10^{-6} and the Larmor frequency of $^{40}Ar^{13+}$ in our $\approx 4.023\,\mathrm{T}$ being about $37\,\mathrm{GHz}$ leads to a scanning frequency range of about $100\,\mathrm{kHz}$. To "hit" the 10^{-8} resonance would require scanning the range with steps of about $150\,\mathrm{Hz}$. Using the typical *g*-factor measurement cycle to find the resonance would translate into about 670 measurement cycles with each cycle lasting about $15\,\mathrm{min}$. With this technique the spin-flip probability is maximally 50% therefore each step should be repeated at least twice. Thus the total measurement time would be in the order of $335\,\mathrm{h}$.

  With this particular set of Helmholtz coils that has been installed outside the ALPHATRAP superconducting magnet, the magnetic field at the center of the trap is modified by $0.588\,86\,\mu\mathrm{T/mA}$. The sweep during the ARP is in fact performed my increasing the current in the Helmholtz coils to a value of $350\,\mathrm{mA}$ in 30 steps, in a timescale of $40\,\mathrm{ms/step}$. Therefore, the magnetic field is changed by $6.867\,\mu\mathrm{T/step}$ which translates into a relative change of 1.7×10^{-6}. That means that the Larmor frequency ν_L is changed by $15.9\,\mathrm{kHz/step}$ leading to a total of 6 measurement cycles ($\sim 1.5\,\mathrm{h}$) for scanning a frequency range of $100\,\mathrm{kHz}$. That way the range is reduced to $15.9\,\mathrm{kHz}$ and with a few additional sweeps with adequate sweep-range overlapping the range has been finally reduced to the desired range of $2\,\mathrm{kHz}$.

- The adiabaticity condition from equation (4.61) reads as:

$$\frac{|\omega_\mathrm{R}|^2}{|\dot{\omega}|} \approx 19 \tag{4.67}$$

- Instead of a rotating mm-wave field the injected field is in fact a linearly polarised field. This can be considered as a superposition of a co-rotating and a counter-rotating field. Close to resonance and when we apply the transformation to the rotating frame, we "select" the co-rotating field component according to the rotating wave approximation (RWA). That way the co-rotating component becomes time independent while the counter-rotating component rotates with twice the frequency. The amplitude of the co-rotating field is reduced by a factor of 2.

  The presence of a counter-rotating field introduces a shift of the Larmor frequency, namely the Bloch-Siegert frequency shift [69, 70]. It is given by

$$\frac{\Delta\omega_\mathrm{L}}{\omega_\mathrm{L}} \approx \left(\frac{1}{2}\frac{\omega_\mathrm{R}}{\omega_\mathrm{L}}\right)^2, \tag{4.68}$$

which could be non-negligible for small static magnetic fields B_0 or strong drives B_{mmW}. For the *g*-factor of $^{40}Ar^{13+}$ at ALPHATRAP this shift is estimated to be in the order of 5×10^{-15}, therefore it is negligible.

5 Experimental setup

Considering the different conditions under which the free-space cyclotron frequency ν_c and the Larmor precession frequency ν_L are being determined, it become obvious that the experimental setup is a rather complicated one. An essential part is the necessity for a double-trap setup in order to account for both a very homogeneous magnetic field for high-precision frequency measurements and a very strong magnetic bottle for spin-state spectroscopy. Additionally, the demanding extreme high vacuum and detection electronics as well as the cryogenic operational temperatures lead to a challenging experimental setup.

The newly assembled setup of ALPHATRAP, even though it is a predecessor of the Mainz *g*-factor experiment on highly charged ions, has some demanding requirements given, for instance, the coupling to an external ion beamline. More details about the bulk of the experiment, such as the magnet, cryostat and cryogenic electronics can be found in the PhD thesis of Andreas Weigel [59] and in the ALPHATRAP review paper [58].

In this chapter the double-trap setup of ALPHATRAP is presented in section 5.1, with emphasis on the precision trap and analysis trap. It is followed by a brief description of the rest of the experimental setup, including the magnet and the cryostat of the experiment in section 5.2 as well as the room-temperature ion-beamline and the ion sources which are coupled to the trap tower in section 5.3.

Parts of this chapter have been published in Ref. [58].

5.1 ALPHATRAP trap tower

The ALPHATRAP trap tower shown in Fig. 5.1 consists of a double Penning-trap system and a set of capture electrodes. The capture trap is used for capturing externally injected ions by fast switching of the potential of this set of electrodes [59]. The double Penning-trap system involves the so called “precision trap” and “analysis trap”, which are the tools necessary for the *g*-factor determination via the double-trap method.

The capture trap, the precision trap and the analysis trap are separated by a series of transport electrodes that allow adiabatic ion transport from one trap to another. The externally injected ions have to travel through the ion injection diaphragm with $3\,\mathrm{mm}$ inner diameter that was planned to be used also as a Faraday Cup during the first attempts of external ion injection. Between the diaphragm and the capture trap a microwave damping cone made from carbon nanotube filled peek (TECAPEEK ELS nanoblack [71]) is installed, which has a specific volume resistance within the range of $10^3\,\Omega\,\mathrm{cm}$ to $10^5\,\Omega\,\mathrm{cm}$. Every electrode is isolated from its neighbouring electrodes

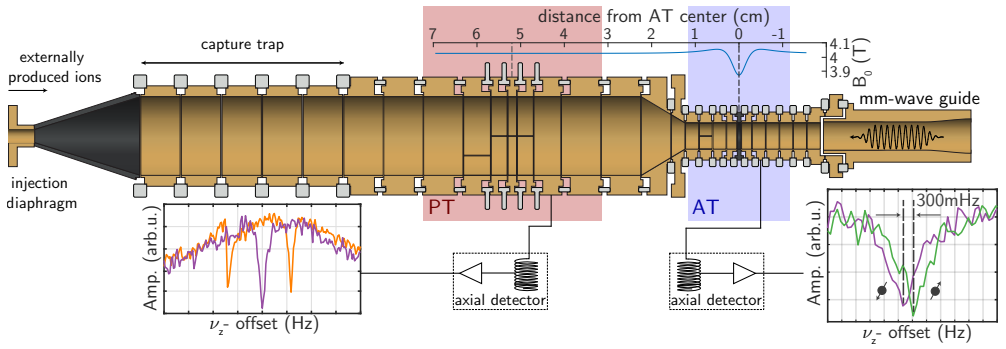

Fig. 5.1: The ALPHATRAP trap tower. The precision trap is used for high-precision spectroscopy and the analysis trap is used for the spin-state determination via the continuous Stern-Gerlach effect. The ions enter via the ion injection diaphragm before they are captured within the capture trap. Modified from [27].

by sapphire or quartz insulators[1], whilst the insulator between the bottom plate of the analysis trap and the mm-wave guide is made out of PEEK material.

To prevent undesired effects due to paramagnetic oxygen contaminations, which would lead to sizeable fluctuations of the magnetic field at cryogenic temperatures, all electrodes are made out of Oxygen Free High Conductivity (OFHC) copper and have been machined with a tolerance of $10\,\mu\mathrm{m}$. After manufacturing, in order to avoid oxidation, all electrodes were subjected to gold-plating, where a uniform layer of $10\,\mu\mathrm{m}$ of gold was deposited on the electrodes' surfaces via galvanic deposition. A $2\,\mu\mathrm{m}$ silver layer acts as a diffusion barrier between copper and gold.

All the electrodes have been very carefully cleaned before and after the gold-plating procedure. The assembly of the trap tower as well as the wiring of all electrodes took place inside a clean-room. The trap assembly was performed under a microscope after which the dimensions of the trap were verified using high-precision measurement tools with $1\,\mu\mathrm{m}$ measurement precision.

5.1.1 Precision trap

In order to allow for high-precision experiments with both low and highly charged ions, the precision trap has to meet a number of special requirements. For this reason, the precision trap is larger than predecessor high-precision Penning traps and features an exceptionally harmonic electrostatic potential. In Fig. 5.2 the precision-trap electrodes are depicted. The trap features some non-standard characteristics:

[1] Both the sapphire and the quartz-glass insulators were manufactured with tolerances down to $3\,\mu\mathrm{m}$ for the critical surfaces.

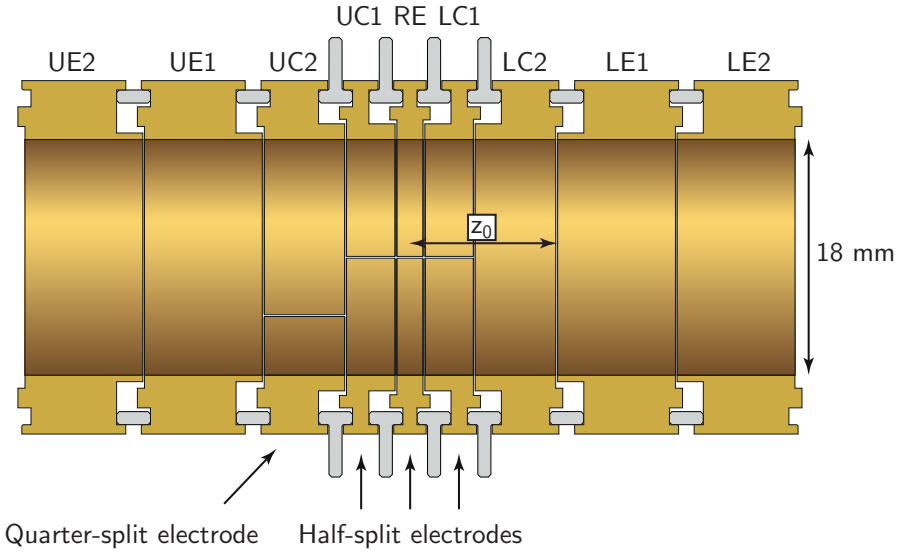

Fig. 5.2: A schematic representation of the precision trap is shown. It consists of a ring electrode (RE), two sets of correction electrodes - upper correction 1 (UC1), lower correction 1 (LC1) and upper correction 2 (UC2), lower correction 2 (LC2) - and four endcap electrodes (UE1, LE1, UE2 and LE2). The sapphire and glass insulators are shown in grey. The ring electrode as well as the upper and lower correction electrode 1 are half-split while the upper correction electrode 2 is quarter split. Two sets of endcap electrodes are used rather than one set of double-in-length endcap electrodes. Functionally, the endcaps (together with the rest of the trap tower), act together to define the ground potential reference [58].

Large radius

All electrodes of the precision trap have a radius of $9\,\mathrm{mm}$ predominantly to reduce systematic uncertainties that are caused by the image charge shift [55, 61] of the ion's free cyclotron frequency, which scales with $\propto \frac{1}{r^3}$, as has been discussed in section 4.2. Since the relative image charge shift scales linearly with the ion's mass, it would be dominant for heavy ions such as $^{208}\mathrm{Pb}^{81+}$. With the optimised trap geometry with $r = 9\,\mathrm{mm}$, the image charge shift is reduced by more than an order of magnitude compared to predecessor experiments using only a radius of $r = 3.5\,\mathrm{mm}$. Additionally, the effect of patch potentials on the electrode surfaces on the ion's motion is also reduced with a large trap radius. Such patch potentials can occur due to variations of the work function of the gold layer or accumulation of charges on the electrodes during ion loading.

7-Electrode Configuration

Higher electric field harmonicity allows excitation to larger amplitudes without the effect of systematic shifts that would arise otherwise. Cylindrical traps can be made harmonic by suitable electrode geometries and by additional proper tuning of the applied voltages (see section 6.2) in order to correct for the unavoidable deviation from the ideal trap case. Most cylindrical Penning traps are composed of a stack of 5 electrodes, namely a ring electrode, two correction electrodes positioned bilaterally symmetric with respect to the ring electrode and a set of endcap electrodes that are typically grounded. Introducing an extra set of correction electrodes (see Fig. 5.2), allows for compensating higher order field components via two degrees of freedom, leading to much better harmonicity. That way excitations of the ion's motion to larger radii are enabled, an essential feature for high-precision measurement techniques like PnA [64, 55].

The ALPHATRAP precision trap consists of a ring electrode, two sets of correction electrodes and two sets of endcap electrodes (see Fig. 5.2). The ideally very long endcap electrodes have been split in shorter sections. That way the ion can be adiabatically transported to and from the precision trap. Ensuring that the transport between the traps is adiabatic is essential for preventing changes in the spin state or energy of the ion.

On the inner cylinder surface all electrodes have a distance of $l_{\mathrm{g}} = 140\,\mu\mathrm{m}$ from their adjacent electrodes, a distance maintained by means of sapphire or quartz-glass ring insulators. As can be seen in Fig. 5.2, the insulators between the ring and correction electrodes are T-shaped. They are made out of quartz glass and have been machined to at least the same precision as the electrodes. Since the shrinking coefficient of sapphire is significantly smaller than the one of copper, the electrodes shrink onto the insulators in a controlled fashion. This allows for a well-defined final position of the electrodes when cooling down from room temperature to $4\,\mathrm{K}$. The same distance of $140\,\mu\mathrm{m}$ separates the segmented electrodes. The ring electrode as well as the set of first correction electrodes are half split allowing dipole as well as quadrupole excitation that is used for coupling the radial modes to the axial one via sideband coupling (see section 4.4). The second upper correction electrode (UC2) is a quarter-split electrode permitting radial mode coupling. All split electrodes in the precision trap are insulated via sapphire plates which are unnoticeable in Figs. 5.1 or 5.2.

The dimensions of our precision trap, which is designed similarly to the precision trap of the Light Ion Trap (LIONTRAP) [56], a high-precision mass spectrometer for light ions in Mainz, are listed in table 5.3b and have been calculated analytically during the optimisation process [44] and independently verified numerically as well as analytically. In this 7-electrode configuration, five parameters can vary towards the optimum geometry for the highest electric field harmonicity. For a fixed trap radius and gap between adjacent electrodes, these parameters are the length of the ring,

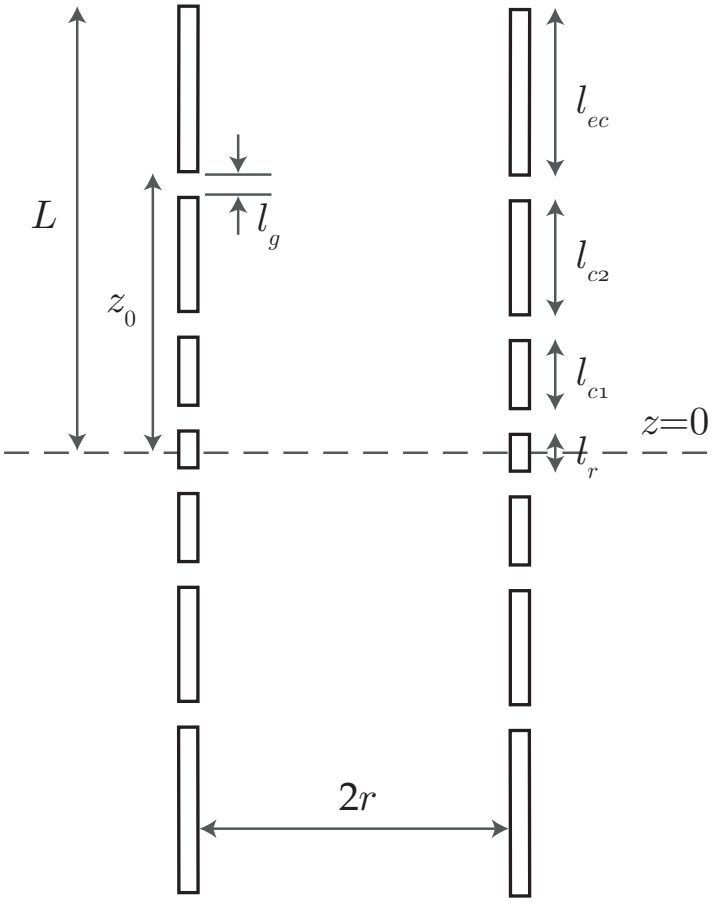

(a)

Electrode	Abbreviation	Variable	length (mm)
Ring	RE	l_{r}	1.997
Correction 1	LC_1/UC_1	l_{c1}	3.715
Correction 2	LC_2/UC_2	l_{c2}	6.164
Endcap	$LE_{1,2}/UE_{1,2}$	l_{ec}	9.023
Radius	-	r	9.002
Gap	-	l_{g}	0.140

(b)

Fig. 5.3: The length definitions of the precision trap are defined in the largely simplified sketch show in (a). Note that here only one set of endcap electrodes is shown, for simplicity. The optimised dimensions of the trap's electrodes are listed in (b).

first and second correction electrodes as well as the voltages applied to the correction electrodes ($l_\mathrm{r}, l_\mathrm{c1}, l_\mathrm{c2}, V_\mathrm{c1}, V_\mathrm{c2}$). The potential in the gap between electrodes has been modelled either as a linear potential or as a 5th order polynomial [72]. It should be noted that in our calculations we found good agreement between the calculations mentioned above.

Assuming an empty trap and cylindrical as well as axial mirror symmetry with respect to the trap centre, the electrostatic potential inside the trap follows equation (3.14) where the C_n coefficients are dimensionless expansion parameters, V_0 is the voltage difference between the ring and the endcap electrodes, $d = \sqrt{\frac{1}{2}(z_0^2 + \frac{r^2}{2})} = 9.156\,\mathrm{mm}$ is a characteristic length of the trap and z_0 is defined as $z_0 = l_\mathrm{r}/2 + l_\mathrm{g} + l_\mathrm{c1} + l_\mathrm{g} + l_\mathrm{c2} + l_\mathrm{g}$, as shown in Fig. 5.3a. The optimisation parameters ($l_\mathrm{r}, l_\mathrm{c1}, l_\mathrm{c2}, V_\mathrm{c1}, V_\mathrm{c2}$) have been chosen such that $C_4 = C_6 = C_8 = C_{10} = 0$ as well as $D_2^\mathrm{comb} = 0$ where

$$C_{n,\mathrm{eff}} = C_n + D_n^\mathrm{comb}, \tag{5.1}$$

$$D_n^\mathrm{comb} \equiv D_{n1} \cdot TR_1 + D_{n2} \cdot TR_2, \tag{5.2}$$

and

$$TR_{1,2} = \frac{V_\mathrm{c1,2}}{V_0}. \tag{5.3}$$

Here, the so-called tuning ratios TR_1 and TR_2 are defined which are the ratios between the voltage applied to the respective correction electrode and the voltage applied to the ring electrode. By optimising both tuning ratios *in situ*, it is possible to completely null at least C_4 and C_6 simultaneously even in the presence of unavoidable machining imperfections. In this case the robustness of our trap design typically causes C_8 to remain small as well. The remaining anharmonicities lead to frequency shifts that are typically negligible even for high-precision measurements.

To be able to practically operate the trap, it is important that the orthogonality criterion is fulfilled. In an orthogonal trap, the ion's axial frequency is independent of the correction voltages. That is, the axial frequency $\nu_z \propto \sqrt{C_2}$ given in equation (3.5), remains unaffected while changing the applied tuning ratio. Since double orthogonality ($D_{21} = D_{22} = 0$) is not possible in this kind of configuration, the trap is orthogonalised by imposing the "combined orthogonality" criterion of $D_2^\mathrm{comb} = 0$ in equation (5.2). In other words, the trap is not orthogonal with respect to the individual correction voltages. When adjusting the voltages that are applied to the first set of correction electrodes also the voltage applied to the second set has to be changed in order to keep the axial frequency invariant. Specifically, the trap was designed such that it is orthogonal when changing both tuning ratios $TR_{1,2}$ by the same factor. Measuring this factor and optimising the trapping field will be discussed is section 6.2.

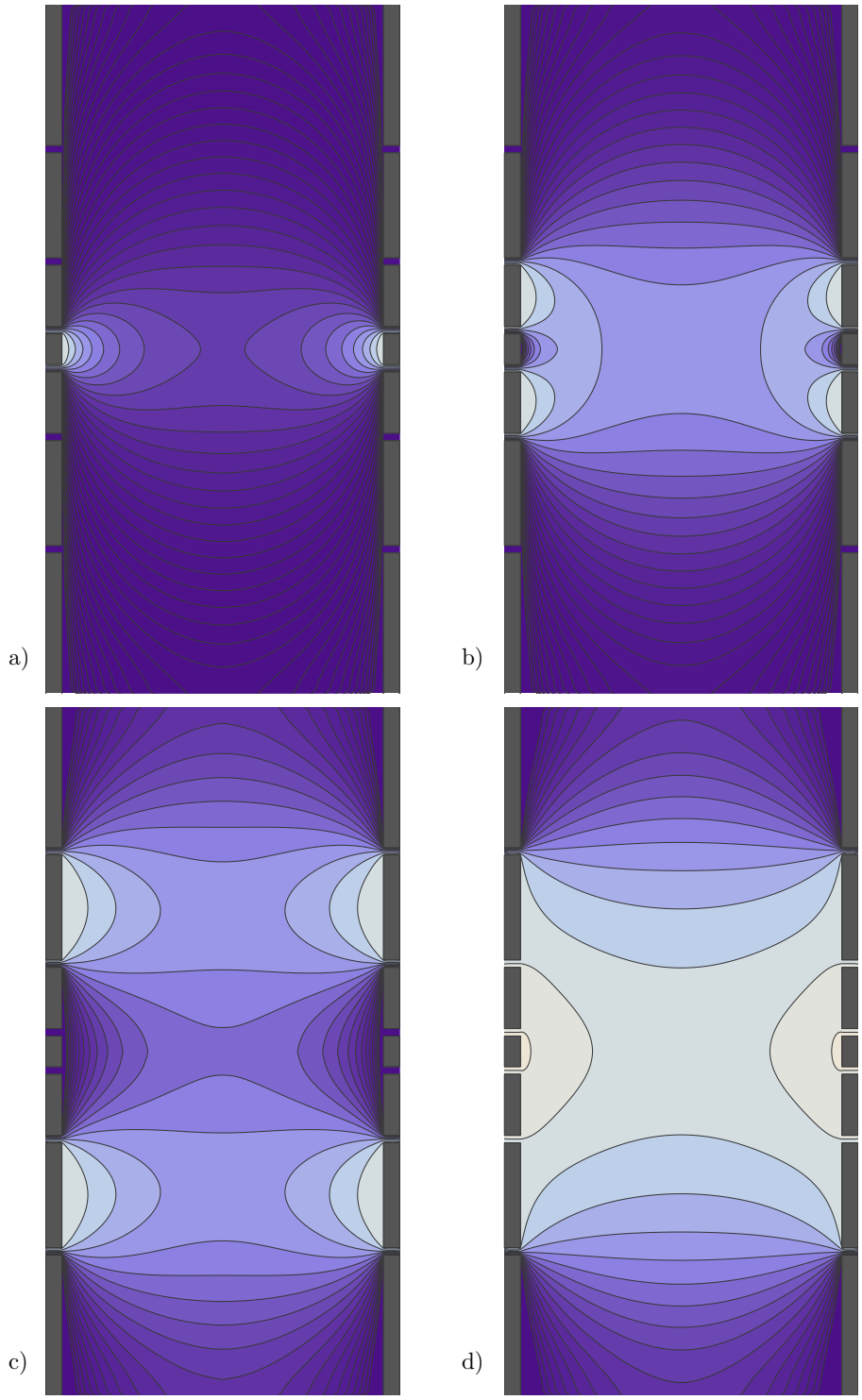

Fig. 5.4: Contour plot of the potential lines of the 7-electrode precision trap. The potential of the ring electrode when 1 V is applied to it and all of the other electrodes are grounded (a), the same configuration for the correction electrodes 1 and 2 ((b) and (c) respectivelly) and the total potential of the trap when the optimal $TR_{1,2}$ are applied (d). Lighter colour indicates higher potential. The dimensions of the electrodes are to scale but the gaps between the electrodes are considered to be larger than $140\,\mu$m, for representation purposes.

The total potential is a superposition of the field produced by V_0, V_{c1} and V_{c2}, yielding

$$\Phi = \phi_0 + \frac{V_{c1}}{V_0}\phi_{c1} + \frac{V_{c2}}{V_0}\phi_{c2} = \phi_0 + TR_1\phi_{c1} + TR_2\phi_{c2}. \tag{5.4}$$

Following Ref. [72] the field produced by the ring electrode and the first and second correction electrode can be written as

$$\phi_k(r,z) = \sum_{n=0}^{\infty} a_n \frac{J_0(i\frac{n\pi}{L}r)}{J_0(i\frac{n\pi}{L}r_0)} \cos(\frac{n\pi}{L}z), \tag{5.5}$$

where $k = \{0, c1, c2\}$ for the individual electrodes, J_0 is the Bessel function of the first kind, r_0 is the trap radius and

$$a_n = \frac{2}{L}\int_0^L \phi_k(r_0,z)\cos(\frac{n\pi}{L}z)dz, \tag{5.6}$$

with $\phi_k(r_0,z)$ being the boundary conditions for the corresponding electrode. The potential field $\phi_k(r,z)$ produced by each electrode when $1\,\mathrm{V}$ is applied to the corresponding electrode while the rest are grounded is plotted in Fig. 5.4a,5.4b and 5.4c. The total field Φ for the optimum individual tuning ratios is plotted in Fig. 5.4d.

Magnetic Field Homogeneity and stability

The magnetic field in the z-direction is given in equation (3.16) and the shift due to the leading order correction, the quadratic magnetic bottle $\sim B_2 z^2$, is given in equation (3.17).

For high-precision determination of the ion's free cyclotron frequency, not only the harmonicity of the electric field is necessary but also the homogeneity of the magnetic field is essential. Due to the shimming procedure, the magnetic field of our superconducting magnet is very homogenous without the trap tower setup. When the double-trap setup is inserted inside the bore of the magnet, the dominant magnetic field inhomogeneity contribution in the precision-trap region is the residual B_2 due to the magnetic bottle configuration. For this reason, a ring that is also made out of the same ferromagnetic material VACOFLUX50 [73] was designed and positioned appropriately so that it compensates for magnetic field inhomogeneities notably, about one order of magnitude. The resulting B_2 in the precision trap was measured to be $B_2 = 0.0643(32)\,\mathrm{T/m^2}$ and the linear field gradient of our setup is $B_1 = 2.638(24)\,\mathrm{mT/m}$ and will be discussed is sections 6.3 and 6.4, respectively.

The magnetic field not only needs to be homogeneous but also as temporally stable as possible. Unlike long-term drifts, the medium-term fluctuations (in the order of $\sim 1\,\mathrm{min}$) of the magnetic field can limit the precision of the measurement when the double-dip technique is employed. Although the frequencies ν_{mmW} and ν_c are determined simultaneously, fluctuations during the measurement period increase the Larmor resonance linewidth as discussed in sections 4.6 and 7.2.

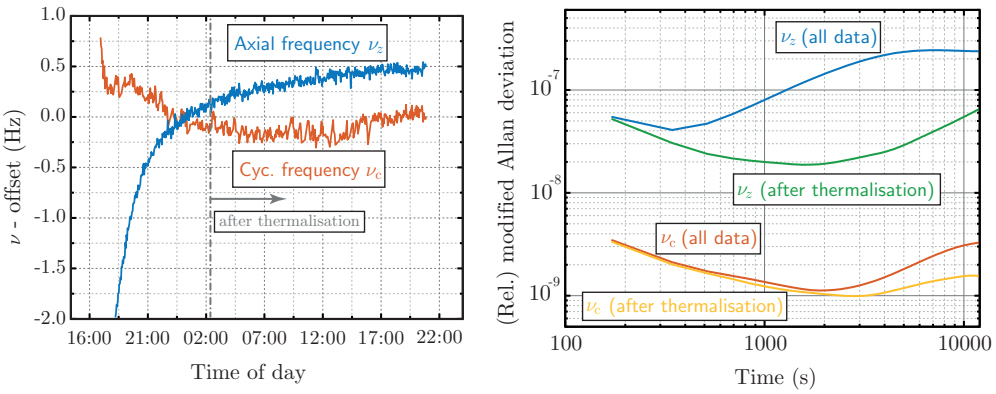

Fig. 5.5: (left) Axial and free-cyclotron frequency measurements in the precision trap over the course of several hours. The data was recorded after refilling the cryogen reservoirs and a thermalisation process is clearly visible over the first hours. (right) Modified Allan deviation of the time sequence on the left. For the green and yellow traces only data after the thermalisation (indicated on the left plot) is used [58].

ALPHATRAP's superconducting magnet has been shimmed and the resulting magnetic field has been measured with an NMR probe prior to full assembly of the experiment. Afterwards, while measuring the relative stability of ν_+ the observed frequency drift required the implementation of a self shielding superconducting coil [58, 74] which is designed to compensate for externally induced magnetic field gradients by conservation of the flux in the centre of the precision trap. The resulting field stability after the superconducting self-shielding coil was installed is demonstrated in Fig. 5.5, where several consecutive measurements of ν_+ were taken over the course of about 15 hours. During the same time, the behaviour of the axial frequency is monitored in order to check the stability of the voltage source simultaneously. The voltage applied on the precision-trap electrodes is supplied by a custom-made voltage source, the Stable Reference for Penning-trap experiments (StaRep) [75]. It can supply up to $-100\,\mathrm{V}$ with each channel having a precision of a few nV and a voltage stability $< 10^{-8}$ for a time scale of $15\,\mathrm{min}$.

It should be noted that to date, neither the experimental setup nor the voltage source are temperature or pressure stabilised. This is an ongoing project that is expected to improve the frequency stability by reducing the influence of environmental conditions.

5.1.2 Analysis trap

The analysis trap is dedicated to the determination of the ion's spin state via the continuous Stern-Gerlach effect [66] (see section 4.5). There, in contrast to the precision trap, a very strong magnetic inhomogeneity is required in order to allow for detectable axial frequency jumps caused by spin flips. This trap differs from the

precision trap in a few important aspects: it has a ferromagnetic ring electrode, it is smaller in dimensions and it is a 5-electrode trap.

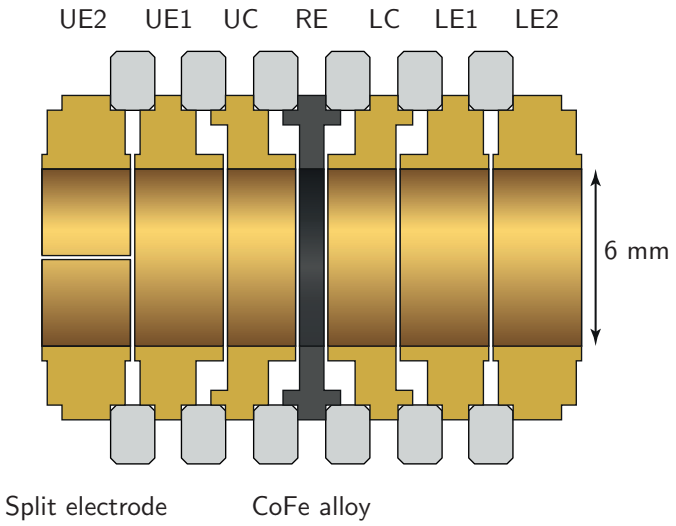

(a)

Electrode	Abbreviation	length (mm)
Ring	RE	0.823
Correction	LC/UC	2.309
Endcap	$LE_{1,2}/UE_{1,2}$	3.004
Radius	-	3.002

(b)

Fig. 5.6: Schemtic of the analysis trap (a) [58] as well as its dimensions (b).The trap consists of a ring electrode (RE), a set of correction electrodes (upper correction (UC) and lower correction electrodes (LC)) and two sets of endcap electrodes (upper endcap 1 and 2 (UE1 and UE2) and lower endcap 1 and 2 (LE1 and LE2)). The ferromagnetic ring electrode (RE), that is depicted here in black for demonstrative purposes, is also gold-plated in reality. The half-split electrode (UE2) for Q_{xz} excitation is shown. The electrodes are insulated via sapphire rings (grey).

Magnetic Bottle

The ring electrode of this trap is made out of VACOFLUX50 [73], which has a very high saturation magnetisation corresponding to about $2.35\,\mathrm{T}$ and can locally create the strong magnetic bottle configuration that is necessary for the spin-flip detection (for details see section 4.5). The strength of the magnetic bottle is experimentally determined as discussed in section 6.5.

5-Electrode Configuration

The analysis trap, shown in Fig. 5.6, is much smaller than the precision trap. With a radius of $r_{\mathrm{AT}} = 3\,\mathrm{mm}$ the necessary strong magnetic bottle configuration is enabled. The lower limit for the radius of the analysis trap was set by the spin transition frequency of boronlike lead $^{208}\mathrm{Pb}^{77+}$, as a smaller radius would not support transmission of the mm-waves required to induce a spin flip. The dimensions of the analysis-trap electrodes are given in table 5.6b.

The analysis trap is a five-electrode trap with only a single set of correction electrodes as shown in Fig. 5.6. Just like in the case of the precision trap, the analysis trap includes two sets of short endcap electrodes instead of one set of long endcap electrodes to enable adiabatic ion transport.

Similarly to the precision trap, the electrodes are made out of OFHC copper and have been gold plated with the same galvanic process that is mentioned in section 5.1.1. Owing to the small radius of this trap, and therefore the larger impact of the image charge shift and patch potentials on the surface of the electrodes, the inner surface of the analysis-trap electrodes has been plasma polished to ensure a smoother surface. Unlike the T-shaped insulators that are used in the precision trap for controlled positioning of the electrodes at a temperature of $4\,\mathrm{K}$, here the sapphire insulators have a simpler rectangular shape. They maintain the same distance between the electrodes, a distance of $140\,\mu\mathrm{m}$, whilst the two halves of the split electrode of the trap are kept in distance by spherical quartz glass insulators.

Axial Frequency Stability

For unambiguous spin-flip determination in the analysis trap, disturbances of the modified cyclotron frequency, ν_+, need to be minimised since unwanted noise would compromise the stability of the axial frequency, ν_z. Due to the strong magnetic field inhomogeneity, energy fluctuations of the modified cyclotron mode E_+ would inhibit measurable axial frequency fluctuations. Within this configuration, the influence of the trap voltage is low (due to the low axial frequency) compared to the desirable large influence of the spin state and the influence of E_+ on the axial frequency stability.

In the case of a boronlike argon ion the expected frequency jump due to a spin flip is $312\,\mathrm{mHz}$. To detect a shift of $312\,\mathrm{mHz}$ out of the $335\,\mathrm{kHz}$ of the ion's axial frequency with high fidelity, we impose the requirement of at least $75\,\mathrm{mHz}$ stability. That means that the applied voltage needs to be stable at a 4.5×10^{-7} level. This level of stability is provided by a UM1-14 voltage source [76] (for details see Ref. [59]) and as can be seen in Fig. 5.7 the axial frequency stability requirement is met for $^{40}\mathrm{Ar}^{13+}$, permitting explicit spin-flip detection. Measuring the axial frequency consecutively over the course of several hours, the obtained jitter was found to be about $55\,\mathrm{mHz}$. In the same figure, the strong drift that occurred during the first $3\,\mathrm{h}$

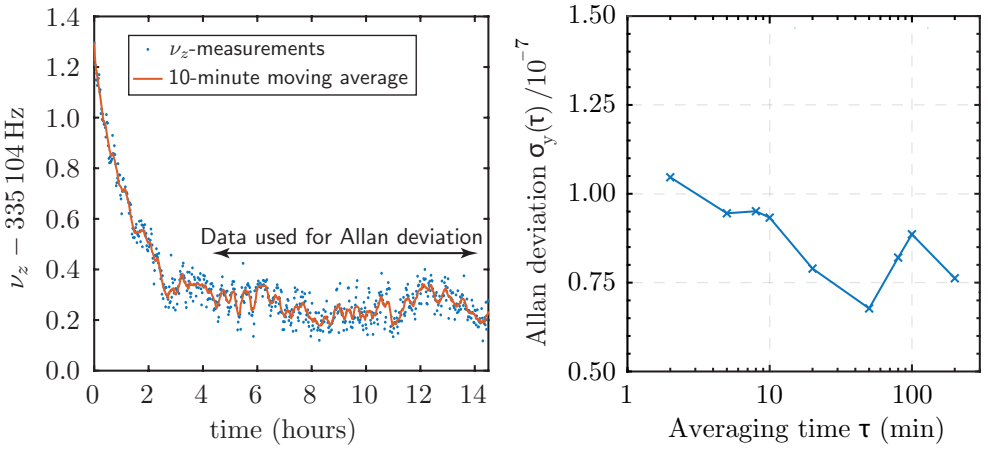

Fig. 5.7: (left) Axial frequency stability in the analysis trap over time. Consecutive axial frequency measurements over the course of $14\,\mathrm{h}$ where each data point is obtained every $80\,\mathrm{s}$. The strong drift during the first $3\,\mathrm{h}$ of the measurement shown in the left plot is due to thermalisation of the voltage source, and is plotted for demonstration purposes. (right) The Allan deviation is plotted with respect to measurement time, excluding the thermalisation data [58].

is due to thermalisation of the voltage source with the environmental conditions of the lab.

5.1.3 Millimeter-wave setup

The mm-wave injection is essential for spin-flip spectroscopy. For the ground state of a boronlike ion the Zeeman splitting within our $4.023\,\mathrm{T}$ magnet is about $37.3\,\mathrm{GHz}$. These mm-waves are generated by a synthesizer (Anritsu MG3694C) which can generate waves with frequencies up to $40\,\mathrm{GHz}$. Those waves are transmitted in the room-temperature apparatus towards the trap with rectangular waveguides, the dimensions of which is chosen with respect to the frequency of the wave.

The waves are transmitted from the output of the generator to the bottom of the magnet and inside the magnet bore. There, the mm-waves propagate from room temperature to the cryostat's insulation vacuum and finally to the cryogenic vacuum of the trap chamber. For this, different horn-to-horn transitions are installed for each of the different temperature/pressure stages. At the bottom of the trap chamber, which is at $4\,\mathrm{K}$, a UV fused silica window is installed and allows transmission of both the mm-waves as well as light over a broad spectral range from visual down to near ultraviolet. That way simultaneous injection of mm-waves and a laser beam, which can be used for e.g. Doppler laser cooling as described in Refs. [58, 77, 74] or laser spectroscopy of HCI [78], is possible.

For hydrogenlike ions however, the spin-flip frequency amounts to $112\,\mathrm{GHz}$, about a factor of three higher than boronlike ions. To be able to transmit those waves in the trap for future experiments, not only the the output of the synthesiser needs to be multiplied by an active multiplier chain (OML S10MS), but also single-mode

operation needs to be ensured. This is achieved by a mode-cleaner in the cryogenic setup which would replace the currently attached straight tube. The setup for $112\,\mathrm{GHz}$ wave transmission is detailed in Ref. [79].

5.2 Magnet and cryostat

The Penning traps of the ALPHATRAP setup are inserted in the warm bore of a superconducting magnet which provides the homogeneous and temporally stable magnetic field. The magnet, a schematic of which is shown in Fig. 5.8, is an Oxford 200/130 NMR vertical bore magnet, which has previously been used in the SMILETRAP experiment [80]. It can generate a field of up to $4.7\,\mathrm{T}$, but has been charged to only $4\,\mathrm{T}$. This choice brings the Larmor and cyclotron frequencies into a convenient regime. Prior to inserting the setup in the magnet's bore, the magnetic field has been shimmed to about $2 \cdot 10^{-7}$ based on the line shape of a $1.5\,\mathrm{cm}^3$ cylindrical NMR probe.

The experiment is cryogenically cooled by an independent liquid helium cryostat which has been specifically designed for ALPHATRAP. That way the trap chamber is surrounded by an insulation vacuum, which significantly reduces the challenging requirements on the leak-tightness of the setup. The liquid nitrogen (LN_2) tank is placed on top of the magnet. It which contains $55\,\mathrm{l}$ of LN_2, sufficient to keep the experiment cold for about 5 days. A copper shield tube extends into the superconducting magnet's bore and provides the thermal shielding of the inner $4\,\mathrm{K}$ insert, which hangs vertically on three Vespel SP1 rods for minimum heat conductance.

While the $4\,\mathrm{K}$ part can be easily removed by a crane, the $77\,\mathrm{K}$ cryostat is permanently mounted. To provide optimal radiation shielding, the LN_2 cryostat is completed by a piece of copper shield, which is mounted on the $4\,\mathrm{K}$ insert. It is attached by copper braids and copper-beryllium springs to the LN_2 cryostat just before the final lowering of the $4\,\mathrm{K}$ insert. The complete $77\,\mathrm{K}$ stage is insulated by vacuum and multi-layer insulation (MLI). The $4\,\mathrm{K}$ stage, which is mainly subjected to conductive load via the electric cabling, is radiation-shielded by a high-conductivity, single layer metal foil, which minimises absorption of heat radiation from the $77\,\mathrm{K}$ stage. The overall load on the $4\,\mathrm{K}$ stage, including dissipated power in the cryogenic amplifiers, is sufficiently low to result in a hold-time of about 5 days with $14\,\mathrm{l}$ of LHe.

5.3 Beamline and ion sources

The ALPHATRAP trap tower is connected to several ion sources, which can deliver ions of any charge-to-mass ratio up to $^{208}Pb^{81+}$, via an ion beamline as shown in Fig. 5.8. Those ion sources are the Heidelberg electron beam ion trap (EBIT) [81], the Heidelberg compact EBIT (HC-EBIT) [82] and a laser ablation ion source (LIS) [83]. The ion sources as well as the beamline are also discussed in Refs. [58, 59].

The cryogenically operated HD-EBIT is going to deliver the heavy HCI up to $^{208}Pb^{81+}$ that will allow ALPHATRAP to preform high-precision tests of QED in strong

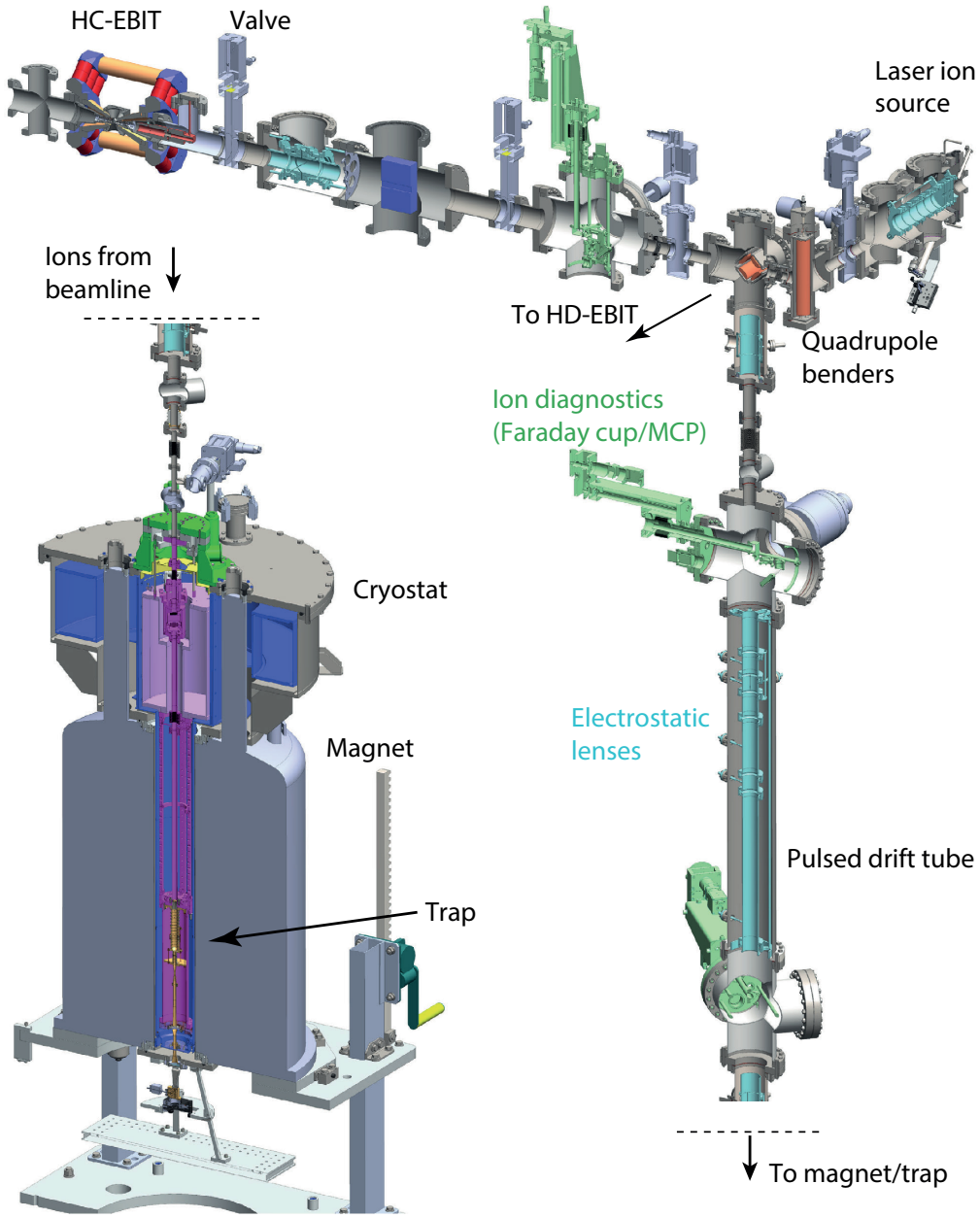

Fig. 5.8: Overview of the ALPHATRAP beamline, cryostat and magnet. The ion sources indicated in the figure. The setup is distributed over two levels, with the floor separating the two levels indicated here with a dashed grey line. The main laboratory houses the trap which is placed in the warm bore of the superconducting magnet and it is located in the basement of the experimental hall of MPIK. In the ground-floor, the superconducting HD-EBIT is located. A part of our beamline coupling ALPHATRAP to the HD-EBIT is not shown in the figure. Externally produced ions are guided towards the vertical beamline by electrostatic quadrupole benders. Before the ions are injected towards the trap and captured in the capture-trap, a pulsed drift-tube is used to reduce the kinetic energy of the ion bunch down to $100\,\mathrm{eV} \times \mathrm{q}$. Figure taken from [58].

fields. HD-EBIT is designed to generate and electron beam with up to $150\,\mathrm{keV}$ energy and a current of $500\,\mathrm{mA}$. The strong magnetic field of up to $9\,\mathrm{T}$ is produced by a superconducting magnet. It can, in principle, produce ions such as $^{208}\mathrm{Pb}^{81+}$. At the moment, the HD-EBIT is being modified in order to reach the design parameters that would allow heavy HCI production. Before the heaviest HCI can be delivered however, a wide range of middle-Z HCI are of interest and will be produced by HD-EBIT and delivered to ALPHATRAP in the near future.

The HC-EBIT is a room-temperature, permanent magnet EBIT. The magnetic field in the center of the trap is about $0.74\,\mathrm{T}$ which compresses the electron beam for higher ionisation rates. The cathode is typically at potential of $-1\,\mathrm{kV}$ to $-1.5\,\mathrm{kV}$ with respect to ground while the inner electrodes, which are used for axial ion trapping, are at potentials of about $+2\,\mathrm{kV}$, resulting in electron energies of up to $3.5\,\mathrm{keV}$ in the center of the structure. Using this HC-EBIT low- and medium-Z ions up to $^{40}\mathrm{Ar}^{16+}$ and $^{129}\mathrm{Xe}^{37+}$ have been produced in a pulsed ejection mode [82]. The $^{40}\mathrm{Ar}^{13+}$ used for the g-factor measurement presented in this thesis has been produced by the HC-EBIT.

LIS is a laser ablation source where a high-intensity pulsed laser (doubled Nd:YAG laser system by Litron Nano S) is used to ablate atoms from a solid target. It has a maximum pulse energy of $35\,\mathrm{mJ}$ and a pulse length of $6\,\mathrm{ns}$ to $8\,\mathrm{ns}$ at $532\,\mathrm{nm}$. With high power density of $> 1 \times 10^8\,\mathrm{W/cm^2}$ a plasma is created the ions of which are extracted by applying a constant electric field. So far, LIS has been used for beryllium-ion production which have been successfully delivered and trapped in ALPHATRAP.

The externally produced HCI are directed to the trap by means of an ultra-high vacuum (UHV) beamline. During ion injection there exists a line-of-sight from room temperature to the $4\,\mathrm{K}$ cryogenic environment of the trap. In order to minimise the particle flux, vertical section of the room-temperature beamline has a pressure of $10^{-11}\,\mathrm{mbar}$. Several diagnostic units are installed that consist of a microchannel plate (MCP), a phosphorous plate and a CCD camera (Allied Vision Prosilica GC655). Additionally, the beamline is equipped with focus lenses and steerers that allow successfully guiding the ion beam until the magnetic field gradient which finally guides the ions towards the capture section of ALPHATRAP.

6 Towards the first ALPHATRAP g-factor measurement

In order to preform a g-factor measurement, the trap and thus the behaviour of the particle inside the trap need to be very well under control and understood. For that purpose series of measurements have been performed with the goal of optimising the trapping conditions and probing the residual effects.

The preparation for a g-factor measurement is essential for the final result and is presented in this chapter. This includes the creation of a single ion of interest which is presented in section 6.1 as well as the optimisation and characterisation of the trapping fields of the precision trap which are presented in sections 6.2, 6.3 and 6.4. Furthermore, the characterisation of the magnetic bottle configuration in the analysis trap which enables spin-state detection is described in section 6.5. Achieving a sufficiently low temperature of the particle is essential throughout a g-factor measurement. A source of heating of the modified cyclotron mode is shown in section 6.6 and finally the determination of the axial temperature of the ion is discussed in section 6.7.

6.1 Single ion preparation

After an ion bunch has been captured with the capture electrodes and transported to the precision trap, the very important task of reducing the cloud to a single ion of interest takes place. Different techniques exist for reducing the ion cloud population down to a single ion, namely the axial, magnetron and cyclotron cleaning techniques, which will be discussed in this section. It should be noted that the data presented in this section has been obtained for carbon ions. Nevertheless, the exact same techniques are used for preparing a single boronlike argon ion.

Axial cleaning is used to remove all particles with q/m different to the one of interest. It consists of strong rf-excitation sweeps that are applied on all frequencies except the axial frequency of the ion of interest. That way, unwanted species are excited to large amplitudes before the applied confining potential is shortly relaxed, so that the energetic ions are no longer axially confined. In Fig. 6.1 a cloud of five $^{12}C^{5+}$ ions is shown in blue, after axial cleaning has been applied. When the impurities are removed from the trap, a single ion is prepared by lowering the trap potential until all ions but one are lost due to collisions between the ions.

Another possibility to reduce the ion population down to the one of interest, is by addressing the magnetron mode. With this *magnetron cleaning* technique, a wideband excitation in the form of noise close to the magnetron frequency is applied. Only the magnetron motion of the ion of interest is simultaneously cooled using the axial-magnetron sideband, in order to cancel the effect of the applied noise. This

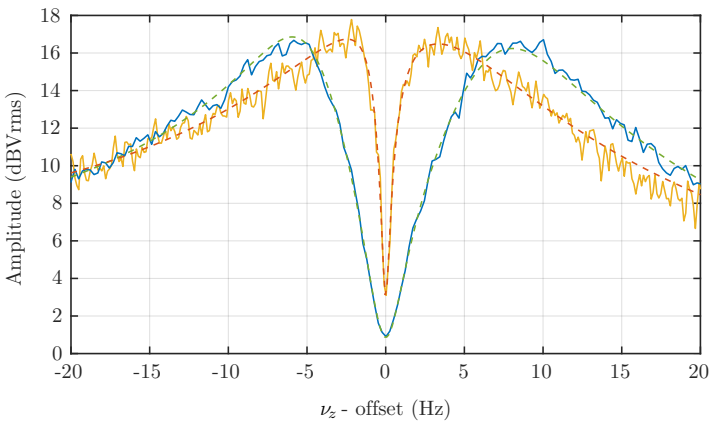

Fig. 6.1: The axial dip formed by a single $^{12}C^{5+}$ ion (yellow) and the dip corresponding to five $^{12}C^{5+}$ ions (blue). The dip width scales linearly with the number of ions, see also Fig. 6.2.

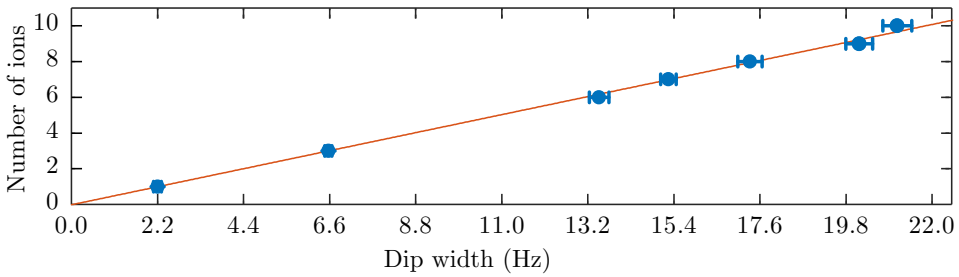

Fig. 6.2: Measured dip width with respect to the number of $^{12}C^{5+}$ ions. The linear fit to the data is plotted in red.

way all unwanted species are eventually lost radially to the walls of the trap, leaving the ion(s) of interest confined inside the trap.

When the cloud consists only of ions of the desired charge-to-mass ratio, the *cyclotron cleaning* technique can be used to reduce it to a single ion of interest.

Since the width of the noise dip scales linearly with the number of ions resonant with the detection system, we can extract the number of ions inside the trap from a fit to the dip. In Fig. 6.2 the number of $^{12}C^{5+}$ ions with respect to the dip-width is plotted. By applying a burst excitation on the modified cyclotron frequency of the ion species, all existing ions are excited to slightly different amplitudes mostly due to collisions. Consequently, each ion appears as an individual peak on the cyclotron resonator, assuming that the cyclotron resonator is tuned to the ion's ν_+, which was not the case for $^{40}Ar^{13+}$. In this configuration it is possible to address individual ions by individual chirped cyclotron excitations. Finally, the hot ions can be removed

from the trap either by exciting the now individually shifted axial frequencies or by simply lowering the trap potential and waiting for collisions of the hot ions. A good signature for the success of the cleaning procedure is shown in figure 6.1, where the dip width of the signal shown in the yellow spectrum corresponds to a single ion. Especially in the analysis trap, the stability of the axial frequency is a good indicator for remaining contaminants as any interactions between different ions would inevitably lead to frequency fluctuations in the strong magnetic bottle.

6.2 Electric Field Optimisation

The goal of creating a quadrupole trapping potential as close to the ideal as possible is central for preforming high-precision measurements, as discussed in sections 3.2.1 and 5.1.1. Even though the dimensions of the trap have been thoroughly optimised, the potential will differ slightly from the calculated one due to the finite machining precision and unavoidable variations of the potential on the electrode surfaces, the so-called patch potentials.

As mentioned in sections 3.2.1 and 5.1.1 the C_n coefficients in equation (3.14) that characterise the leading order anharmonicities of the electric field (C_4, C_6, C_8 and C_{10} in the case of ALPHATRAP) can be minimised by applying suitable correction voltages. To do so, the ion's axial frequency was monitored while the radius of the ion's magnetron motion was altered. In the presence of electric field imperfections, the relative axial-frequency shift by the dominant C_4 contribution is given by [53]

$$\frac{\Delta\nu_z}{\nu_z} = -\frac{C_4}{C_2}\frac{3}{2d^2}r_-^2 \tag{6.1}$$

in first order. Because the precision trap is a 7-electrode trap, it needs to be dynamically compensated as discussed in section 5.1.1. Therefore, during the optimisation measurement for each magnetron radius the correction voltage of both correction electrodes is multiplied by a factor called here "TR_{comb}". Note that the optimum combined tuning ratio is in fact the factor that the calculated tuning ratios TR_1 and TR_2 need to be multiplied by for a highly harmonic electric field in the centre of the precision trap. Up to second order, therefore considering up to the C_6 anharmonicity, the axial frequency shifts with the magnetron excitation strength as

$$\Delta\nu_z \approx -\frac{C_4}{C_2}\frac{3}{2d^2}\nu_z \cdot \kappa_-^2 \cdot (t \cdot U_{\text{exc}}^-)^2 + \frac{C_6}{C_2}\frac{45}{16d^4}\nu_z \cdot \kappa_-^4 \cdot (t \cdot U_{\text{exc}}^-)^4, \tag{6.2}$$

where κ_- is the magnetron radius calibration factor. Assuming the ion is originally cooled to negligible amplitudes, κ_- relates the magnetron radius to the excitation burst as

$$r_- = \kappa_- \cdot t \cdot U_{\text{exc}}^-. \tag{6.3}$$

With optimal settings, even for large radii up to $0.8\,\text{mm}$ (compared to the thermal radius of about $2\,\mu\text{m}$), the axial frequency shifts by significantly less than $1\,\text{Hz}$.

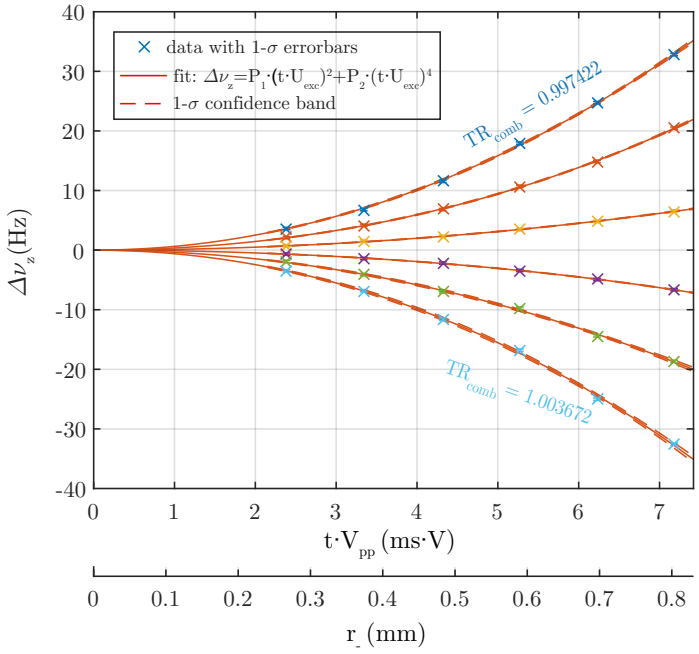

Fig. 6.3: Axial frequency shifts for different tuning ratios at different excitation pulses of the magnetron mode. After having extracted the calibration factor κ_- (see text) the excitation pulses are converted into radii of the magnetron mode, r_-. The plotted axial frequency shift is the difference between the axial frequency when the magnetron mode is pulsed and thermalised ($\nu_z^{\text{hot}} - \nu_z^{\text{cold}}$).

Therefore, the axial frequency is essentially independent of the oscillation amplitude, demonstrating excellent harmonicity.

To obtain the optimal settings for the voltages applied to the correction electrodes, a measurement cycle is as follows: The trap is detuned by scaling the individual tuning ratios with a factor TR_{comb} different to the calculated ideal value TR'_{comb}, which has a value of 1.0 by definition. There the axial frequency ν_z^{cold} is recorded. Then, having set the trap back to the estimated close-to-optimal voltages (therefore setting the factor back to TR'_{comb}), the magnetron burst is applied leading to a larger magnetron radius. At this stage the ν_z^{hot} is recorded with the tuning-ratio factor set to TR_{comb}. Finally the ion is cooled back via sideband cooling and the cycle is repeated for a different trap detuning and for different excitation pulses. The applied excitation pulses of the magnetron mode are dipole rf drives on the D_x electrode and their strength is varied via the pulse length whilst the excitation pulse amplitude is fixed to $0.24\,\text{V}_{\text{pp}}$. Setting an amplitude larger than $0.24\,\text{V}_{\text{pp}}$ on the particular function generator switches on an amplifier that amplifies the output signal. When this happens we have observed an increase of the noise which is avoided by a suitable amplitude setting.

By changing the ions magnetron radius for different TR_{comb} settings we can map the harmonicity of the trap as can be seen in Fig. 6.3. The obtained data from

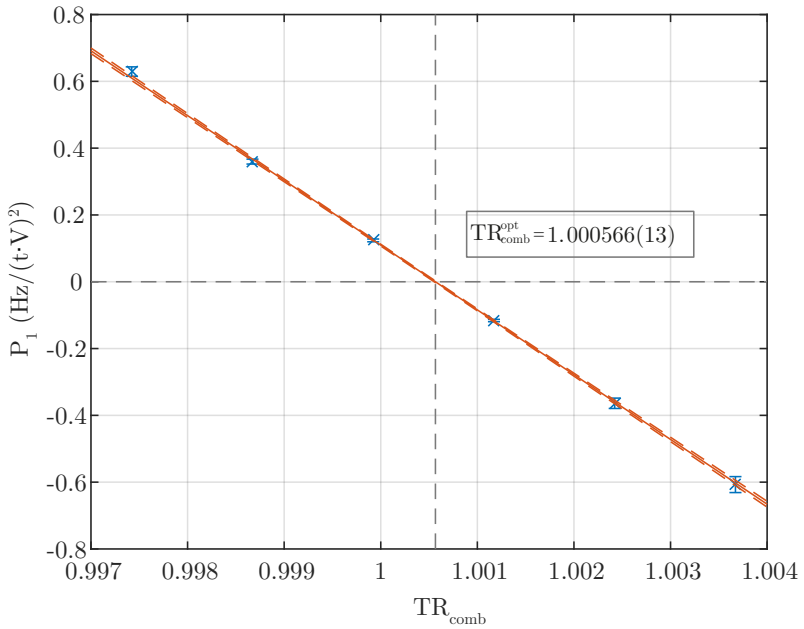

Fig. 6.4: Polynomial fit parameters $P_1(\propto C_4)$ as a function of the combined tuning-ratio factor TR_{comb}. From the linear fit the optimum value $TR^{\text{opt}}_{\text{comb}}$ is obtained for $P_1 = 0$, where the axial frequncy shifted is nulled.

all individual excitation pulse strength scans for each tuning ratio is fitted using equation (6.2). The fitting coefficients are defined as $P_1 \equiv -\frac{C_4}{C_2}\frac{3}{2d^2}\nu_z \cdot \kappa_-^2$ and $P_2 \equiv \frac{C_6}{C_2}\frac{45}{16d^4}\nu_z \cdot \kappa_-^4$. Considering the linear dependence of the C_4 coefficient with respect to the applied tuning ratio (Fig. 6.4), the optimum combined tuning ratio can be obtained.

In order to minimise the C_4 coefficient we chose the tuning ratio factor TR_{comb} that corresponds to the zero crossing in Fig. 6.4, which is $TR^{\text{opt}}_{\text{comb}} = 1.000566(13)$. This value deviates from the expected calculated value by about 5×10^{-4}, which shows a good performance of the experimental setup with respect to the theoretical predictions. For comparison, when we consider the manufacturing tolerances of the PT electrodes ($10\,\mu\text{m}$) and assume that the length of all electrodes and the gap between the electrodes is increased by $10\,\mu\text{m}$ while the trap radius is smaller by $10\,\mu\text{m}$, the deviation from the optimum combined tuning ratio is about 1%. The effect of patch potentials, which have been estimated to be maximally $16\,\text{mV}$, on the optimum expected combined tuning ratio is in the order of 2×10^{-5}.

From the slope a of the fit in Fig. 6.4 and from equation (6.2) we obtain the calibration constant κ_-:

$$\kappa_- = \sqrt{-\frac{2}{3}\frac{aC_2d^2}{D_4^{\text{comb}}\nu_z}} = 111.7(1.3)\mu\text{m}/(\text{V}\cdot\text{ms}), \tag{6.4}$$

where $C_2 = -0.590325$, D_4^{comb} is calculated to be $D_4^{\mathrm{comb}} = -0.786505$, $d = 9.1565\,\mathrm{mm}$ is the characteristic trap size and a is given by the slope in Fig. 6.4 as $a = -193.9(2.3)\,\mathrm{Hz}/(\mathrm{V}\cdot\mathrm{ms})^2$. During this optimisation measurement there was no effect of the C_6 contribution. However, the trap can be further optimised in the future by using larger excitation amplitudes and addressing TR_1 and TR_2 individually. That way the condition $C_4 = C_6 = 0$ can be satisfied.

6.3 B_2 inhomogeneity in the precision trap

In a similar way as described in the previous section the modified cyclotron mode can be addressed for probing the axial frequency shift for different trap detunings at different amplitudes r_+. Here the shifts caused by relativistic effects and the magnetic inhomogeneity B_2 are non-negligible. The absolute axial frequency shift due to the relativistic contribution is given by [54]:

$$(\Delta\nu_\mathrm{z})_\mathrm{Rel} = -\frac{1}{mc^2}\frac{\nu_+\nu_\mathrm{z}}{2(\nu_+-\nu_-)}\frac{(2\pi)^2 m}{2}\nu_+(\nu_+-\nu_-)r_+^2 \approx -\frac{\pi^2}{c^2}\nu_+^2\nu_\mathrm{z}r_+^2. \tag{6.5}$$

When all modes are thermalised with the axial tank circuit, the amplitudes of the modes given by equations (3.13), (4.19), (4.20), and (4.21) are given by

$$\langle z\rangle = \sqrt{\frac{2k_\mathrm{B}T_\mathrm{z}}{m4\pi^2\nu_\mathrm{z}^2}}, \tag{6.6}$$

$$\langle r_+\rangle = \sqrt{\frac{\nu_\mathrm{z}}{\nu_+}}\langle z\rangle, \tag{6.7}$$

$$\langle r_-\rangle = \sqrt{\frac{2\nu_\mathrm{z}}{\nu_-}}\langle z\rangle. \tag{6.8}$$

Therefore, for a $^{40}\mathrm{Ar}^{13+}$ ion with $T_\mathrm{z} = 6\,\mathrm{K}$, $\nu_+ \approx 20\,\mathrm{MHz}$, $\nu_\mathrm{z} \approx 651\,\mathrm{kHz}$ and $\nu_- \approx 10\,\mathrm{kHz}$ the thermal radius of the modified cyclotron mode $\langle r_+\rangle$ is about $2\,\mu\mathrm{m}$. According to equation (6.5) the induced relative shift of the axial frequency of $^{40}\mathrm{Ar}^{13+}$ is in the order of 1.7×10^{-13}. Furthermore, the axial frequency shifts due to the B_2-contribution according to [53]:

$$(\Delta\nu_\mathrm{z})_{\mathrm{B}_2} = \frac{B_2}{4B_0}\frac{(\nu_+ + \nu_-)\nu_\mathrm{z}}{\nu_-}r_+^2 \approx \frac{B_2}{2B_0}\frac{\nu_+^2}{\nu_\mathrm{z}}r_+^2. \tag{6.9}$$

Finally the axial frequency shifts in first order due to electrostatic imperfections according to [53]:

$$(\Delta\nu_\mathrm{z})_{\mathrm{C}_4,\mathrm{C}_6} = -\frac{3}{2d^2}\frac{C_4}{C_2}\nu_\mathrm{z}r_+^2 + \frac{C_6}{C_2}\frac{45}{16d^4}\nu_\mathrm{z}r_+^4, \tag{6.10}$$

when accounting for contributions related with up to the C_6 coefficient and assuming that the coupling terms in the C_6-contribution are negligible at typical thermal am-

plitudes. Adding linearly the contributions of the electrostatic potential, relativistic effect and the magnetic inhomogeneity B_2 given in equations (6.10), (6.5) and (6.9), the axial frequency shifts with respect to the modified cyclotron excitation strength as

$$\Delta\nu_z = \left(-\frac{3}{2d^2}\frac{C_4}{C_2}\nu_z - \frac{\pi^2}{c^2}\nu_+^2\nu_z + \frac{B_2}{2B_0}\frac{\nu_+^2}{\nu_z}\right)\kappa_+^2 \cdot (t\cdot U_{\text{exc}}^+)^2 + \frac{C_6}{C_2}\frac{45}{16d^4}\nu_z\kappa_+^4 \cdot (t\cdot U_{\text{exc}}^+)^4, \tag{6.11}$$

where higher order magnetic field inhomogeneities such as the B_4-contribution are assumed to be negligible. Here κ_+ is the reduced cyclotron radius calibration factor relating r_+ to the excitation burst as

$$r_+ = \kappa_+ \cdot t \cdot U_{\text{exc}}^+. \tag{6.12}$$

By exciting the reduced cyclotron mode to different amplitudes the B_2-coefficient can be extracted. The corresponding measured $\Delta\nu_z$ with respect to the square of the applied excitation pulse is shown in Fig. 6.5. The measurement cycle is the same as discussed in section 6.2 but here we excite the modified cyclotron mode instead, using the same set of pulse lengths as before for the same trap detuning while the amplitude of the pulse is kept constant to $0.15\,\text{V}_{\text{pp}}$. The data is fitted using equation (6.11) with fitting coefficients defined as

$$P_1 \equiv \left(-\frac{3}{2d^2}\frac{C_4}{C_2}\nu_z - \frac{\pi^2}{c^2}\nu_+^2\nu_z + \frac{B_2}{2B_0}\frac{\nu_+^2}{\nu_z}\right)\kappa_+^2, \tag{6.13}$$

$$P_2 \equiv \frac{C_6}{C_2}\frac{45}{16d^4}\nu_z\kappa_+^4. \tag{6.14}$$

The linear dependence of P_1 with respect to TR_{comb} is plotted in Fig. 6.6. From the slope of the linear fit and equation (6.14), the calibration factor κ_+ is determined as

$$\kappa_+ = \sqrt{-\frac{2}{3}\frac{a_+ C_2 d^2}{D_4^{\text{comb}}\nu_z}} = 173.76(98)\,\mu\text{m}/(\text{V}\cdot\text{ms}), \tag{6.15}$$

where $a_+ = -468.9(2.6)\,\text{Hz}/(\text{V}\cdot\text{ms})^2$. In the same plot, the parameter P_1 is nulled only when the C_4 contribution is compensated by both the relativistic and the B_2 contribution. Therefore, the tuning ratio at the zero-crossing point is $TR_{\text{comb}}^{\text{opt}'} = 1.0008807(85)$. Here the optimum is defined for $\Delta\nu_z = 0$, unlike the one presented in section 6.2 where the optimum combined tuning ratio was obtained for $C_4 = 0$. The value of $TR_{\text{comb}}^{\text{opt}'}$ is shifted with respect to the optimum value that is obtained using magnetron-mode pulses. Estimating the contribution of C_4 at $TR_{\text{comb}}^{\text{opt}'}$, the B_2 coefficient is determined from

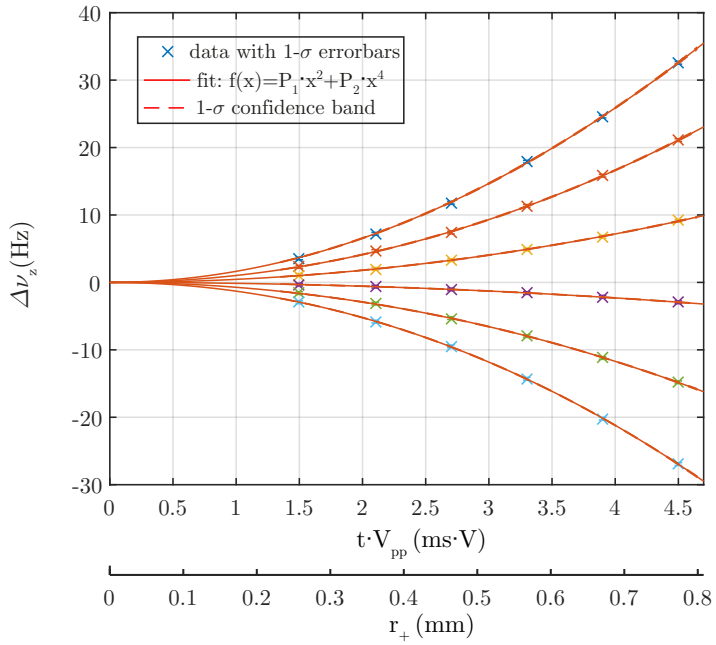

Fig. 6.5: Axial frequency shift for different tuning ratios at different radii of the modified cyclotron mode mode, r_+. The plotted axial frequency shift is the difference between the axial frequency when the modified cyclotron mode is pulsed and thermalised ($\nu_z^{\text{hot}} - \nu_z^{\text{cold}}$).

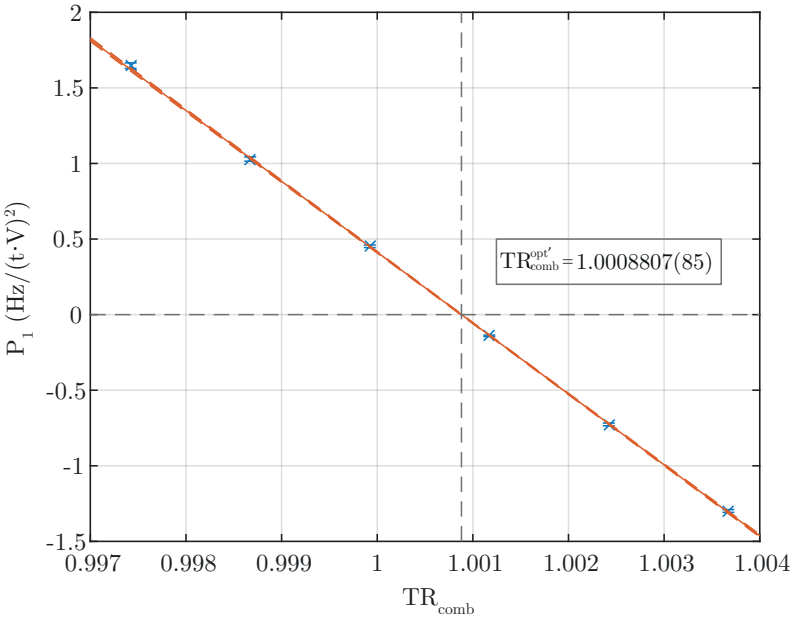

Fig. 6.6: Polynomial fit parameters P_1 as a function of the combined tuning-ratio factor TR_{comb}. From the linear fit the optimum value $TR_{\text{comb}}^{\text{opt}'}$ is obtained for $P_1 = 0$, where C_4 is compensated by the relativistic and the B_2 contribution, unlike in Fig. 6.4 where $TR_{\text{comb}}^{\text{opt}}$ is determined for $C_4 = 0$.

$$B_2 = \frac{2B_0\nu_z^2}{\nu_+^2}\left(\frac{3\nu_z}{2d^2C_2}D_4^{\text{comb}}(TR_{\text{comb}}^{\text{opt}'} - TR_{\text{comb}}^{\text{opt}}) + \frac{\pi^2\nu_+^2\nu_z}{c^2}\right), \tag{6.16}$$

$$\text{as} \quad B_2 = 0.0643(32)\,\text{T/m}^2. \tag{6.17}$$

6.4 B_1 inhomogeneity in the precision trap

The linear gradient of the magnetic field in the center of the precision trap is experimentally determined. The magnetic field gradient creates a net force on the magnetic moment due to the finite cyclotron energy and shifts the axial position of the trapping center.

In order to determine this B_1-inhomogeneity in the precision trap, the position of the ion in the axial direction has been changed assuming that the magnetic force is purely axial. At different positions the free-cyclotron frequency of the ion is extracted, leading to the determination of the magnetic field with respect to the axial distance from the center of the precision trap.

To shift the position of the ion in the axial direction, asymmetric voltages are applied on the outer correction electrodes namely the upper and lower correction electrode 2 (UCE2 and LCE2, respectively). The corresponding shift in z due to an asymmetric voltage applied on those correction electrodes is estimated by means of a simulated potential, shown in Fig. 6.7. By increasing the voltage applied on the UCE2 and simultaneously decreasing the voltage applied on LCE2 by $8\,\text{V}$, the expected shift of trapping center in the axial direction is $1\,\text{mm}$.

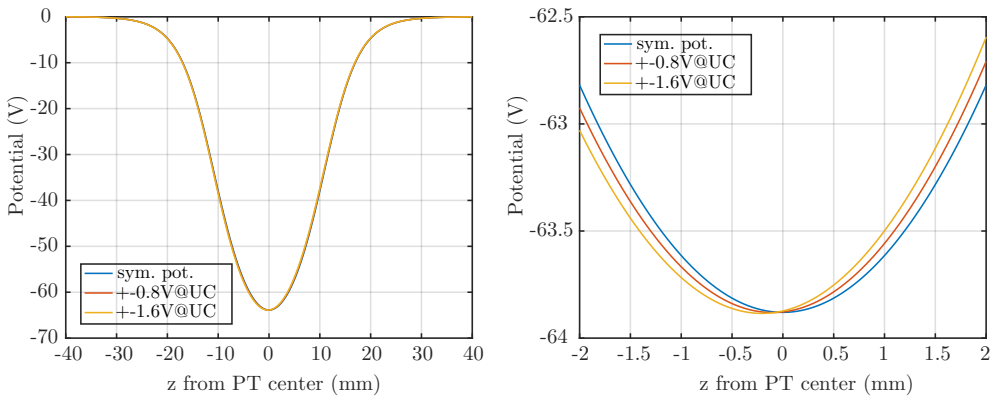

Fig. 6.7: (left) Simulation of the trapping potential in the axial direction. Three different cases are plotted: axially symmetric potential (blue), asymmetric potential where the voltage applied on the UCE2 electrode is increased by $0.8\,\text{V}$ and the voltage on the LCE2 is reduced by $0.8\,\text{V}$ (red) and the same asymmetry as before but with the UCE2 electrode increased increased by $1.6\,\text{V}$ and the voltage on the LCE2 reduced by $1.6\,\text{V}$ (yellow). The right plot is only a zoom into the $z-$direction so that the shift of the trapping center becomes visible.

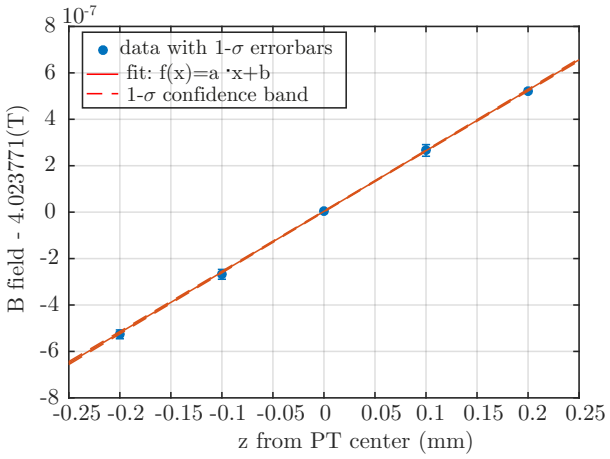

Fig. 6.8: Measured magnetic field at different axial positions in the precision trap. From the linear fit the gradient of the magnetic field is obtained as $B_1 = 2.566(29)\,\mathrm{mT/m}$.

The measured magnetic field with respect to z is shown in Fig. 6.8. From the slope of the linear fit the magnetic field gradient coefficient B_1 is found to be $B_1 = 2.566(29)\,\mathrm{mT/m}$. Here the uncertainty includes a 0.4% uncertainty of the ion's position due to the trap's electrodes machining tolerance ($10\,\mu\mathrm{m}$). The effect of patch potentials, which have been estimated to be maximally $16\,\mathrm{mV}$, on B_1 is negligible. The relative shift of the modified cyclotron frequency due to B_1 is given by [84, 85]:

$$\frac{\Delta\nu_+}{\nu_+} \approx -\left(\frac{B_1}{B_0}\right)^2 \frac{\nu_+^2}{\nu_z^2} r_+^2. \tag{6.18}$$

Given the small radius of about $2\,\mu\mathrm{m}$ that typically exist in the present work, the effect of B_1 on ν_+ is $< 10^{-15}$ and thus insignificant.

6.5 Magnetic bottle in the analysis trap

The strong magnetic bottle configuration in the analysis trap is caused by the dedicated ferromagnetic ring. To measure the strength of the resulting magnetic field inhomogeneity the radius of the modified cyclotron mode r_+ is modified in order to observe the shift in the axial frequency according to equation (6.9). The contributions due to electrostatic anharmonicities and relativistic effects are negligible.

Similarly to the calibration of the magnetron mode radius r_- with respect to the applied pulse which was discussed in section 6.2, the modified cyclotron mode radius r_+ has been calibrated. The relation of the radius to the excitation pulse in the precision trap is given by equation (6.12) and the calibration constant κ_+ given in (6.15).

To determine the B_2 coefficient of the ring electrode in the analysis trap, the ion's axial frequency is measured in this trap before the ion is adiabatically transported to the precision trap. There, the modified cyclotron mode is pulsed to a well-defined radius, according to equations (6.12) and (6.15). Then the ion is transported back to the analysis trap where the axial frequency of the ion is measured anew. The shift of the axial frequency in the analysis trap for various different r_+ is shown in Fig. 6.9.

It should be noted that the plotted radii are the radii in the analysis trap r_+^{AT}. The ion is pulsed to a well-defined radius in the precision trap r_+^{PT} and after it is transported to the analysis trap the radius is modified due to the different B_0 magnetic field, according to:

$$r_+^{\mathrm{AT}} \approx \frac{B_0^{\mathrm{PT}}}{B_0^{\mathrm{AT}}} r_+^{\mathrm{PT}}. \tag{6.19}$$

At the beginning of each measurement cycle, the ion is sideband cooled via the axial resonator in the precision trap before it is pulsed to a different radius and transported to the analysis trap. Each radius has been measured five times. In order to obtain B_2, the data is fitted using a parabolic fit of the form $f(x) = p_1 x^2$ where weights of the form $1/r_+^2$ are considered. That is, due to the fact that a jitter in the modified radius δr_+ leads to a jitter of the axial frequency shift approximately linear to the radius r_+. The obtained result is:

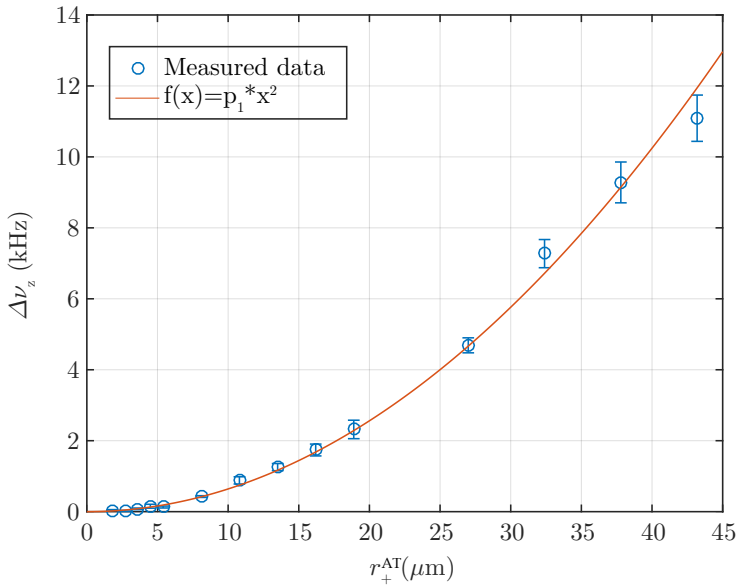

Fig. 6.9: The magnetic bottle configuration in the analysis trap. The ion is pulsed to a well-defined amplitude of the modified cyclotron mode r_+ before it is transported to the analysis trap. There, the axial frequency shifts accordingly and follows a parabolic behaviour with respect to the radius r_+. The coefficient B_2 is extracted from the fit, for more details see text.

$$B_2^{\mathrm{AT}} = 44\,349(837)\,\mathrm{T/m^2}, \tag{6.20}$$

which corresponds to an expected axial frequency jump in the case of $^{40}\mathrm{Ar}^{13+}$ due to a spin flip in the order of $312(6)\,\mathrm{mHz}$ and agrees with the observed value during the *g*-factor measurement.

6.6 Cyclotron heating in the precision trap

It is important to investigate that the temperature of the ion is not modified by spurious noise sources during, for instance, ion transport or waiting times between steps in the *g*-factor measurement cycle.

During the preparatory measurements, the ion was transported several times from the precision trap to the analysis trap and back in order to check the absence of energy accumulation. This dedicated measurement demonstrated adiabatic ion transport between the two traps [59]. Therefore, in the absence of mode coupling in the precision trap, the temperature of the ion should remain unchanged after being transported to the analysis trap. Thus by recording the axial frequency of the ion in the analysis trap after every transport to the precision trap should exhibit a jitter that would only represent the stability of the voltage source of the AT. However, in the here presented measurements the axial frequency shift in the AT indicated a change in the modified cyclotron mode. Within the magnetic bottle, an excess energy in ν_+ leads to a shift in the axial frequency.

To identify the source of heating, several measurements were performed and are plotted in Fig. 6.10. The ion was transported from the analysis trap to the precision trap and back, using different conditions. The data indicate a heating source related to the cyclotron resonator in the precision trap, while the ion's adiabatic transport is confirmed by the last set of data shown in green (circles) in Fig. 6.10. There, the ion has been partly transported to PT and the axial frequency shift in the AT reflects the expected stability of about $60\,\mathrm{mHz}$.

All data shown in Fig. 6.10 have been obtained while the cryogenic amplifier of the cyclotron resonator is in the "off" state. For details about the cyclotron resonator see Ref. [59]. The Q value of the resonator has been measured to be about 3500. The ion's modified cyclotron frequency is $\nu_+ \approx 20.0899\,\mathrm{MHz}$ which leads to a cooling time constant of $\tau_{0\mathrm{V}} = 55.5 \times 10^3\,\mathrm{s}$ and $\tau_{+10\mathrm{V}} = 13.5 \times 10^3\,\mathrm{s}$ for $0\,\mathrm{V}$ and $10\,\mathrm{V}$ on the varactor diode, respectively. From this the resonator's electronic noise is estimated to be about $10\,000\,\mathrm{K}$. This is a rough estimation given that this set of data is the only one recorded so far. Even though it is possible that the initial temperature of the ion was unfavourably high, the estimated temperature is too high to assume a coincidence. This effect needs to be further investigated by measuring the temperature of the cyclotron resonator and verify the source of heating.

It should be noted that the varactor diode is used to shift the cyclotron resonator's frequency as far away as possible from the ion's frequency during the *g*-factor mea-

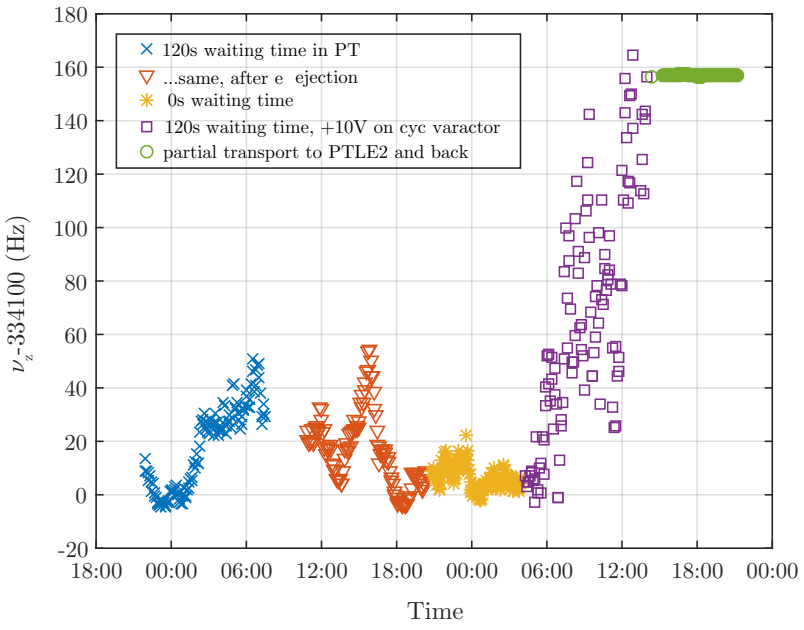

Fig. 6.10: Investigation of the source of heating of the ion above the ambient temperature of 4.2 K. Here we plot the axial frequency difference between consecutive measurements in the analysis trap after the ion is transported to the PT. The points in blue are obtained by transporting the ion in the PT, waiting for 120 s and transporting the ion back to the AT where a dip signal is recorded. Data plotted in red are obtained exactly the same way only that after the first data set in blue was finished an attempt to remove possible electrons trapped in the potential hills of the trap tower has been made. That was followed by a data set where the waiting time in the PT was reduced to 0 s plotted in yellow. Thereafter, in purple the axial frequency is plotted where the waiting time in the PT is once more 120 s and the frequency of the cyclotron resonator is shifted as close as possible to the ion's frequency using the varactor diode. Finally, the ion was only partially transported to the PT, i.e. specifically transported to the second lower endcap of the PT before it was transported back to the AT where the axial frequency was recorded and plotted in green.

surement. Additionally, during the g-factor measurement the modified cyclotron mode is coupled to the axial mode and therefore it is cooled during the determination of Γ. However, this is not the case during the single dip measurements. This effect is taken into account in the final result of the $^{40}Ar^{13+}$ g-factor in section 7.3.7.

6.7 Axial temperature measurement T_z

In order to reduce energy-related shifts, such as shifts due to magnetic field inhomogeneities, electric field anharmonicities, relativistic mass increase as well as the line shape of the Γ resonance, the temperature of the ion needs to be as low as possible during the g-factor measurement.

When the ion is in contact with the axial resonator, it is in thermal equilibrium with the effective temperature of the detection system. This can be higher than the ambient temperature of $4.2\,\mathrm{K}$ due to electronic noise of the cryogenic amplifier. In resonance, the ion's energy fluctuates with the cooling time constant $\tau \approx 40\,\mathrm{ms}$. The ergodic hypothesis states that at thermodynamic equilibrium, the time average and the ensemble average of the energy are equivalent. Therefore, a set of measurements of the ion's energy is also Boltzmann distributed. The thermal distribution of the axial mode is given by

$$\rho(E_\mathrm{z}) = \frac{1}{k_B T_\mathrm{z}} e^{-\frac{E_\mathrm{z}}{k_B T_\mathrm{z}}} \tag{6.21}$$

as shown in figure 6.11.

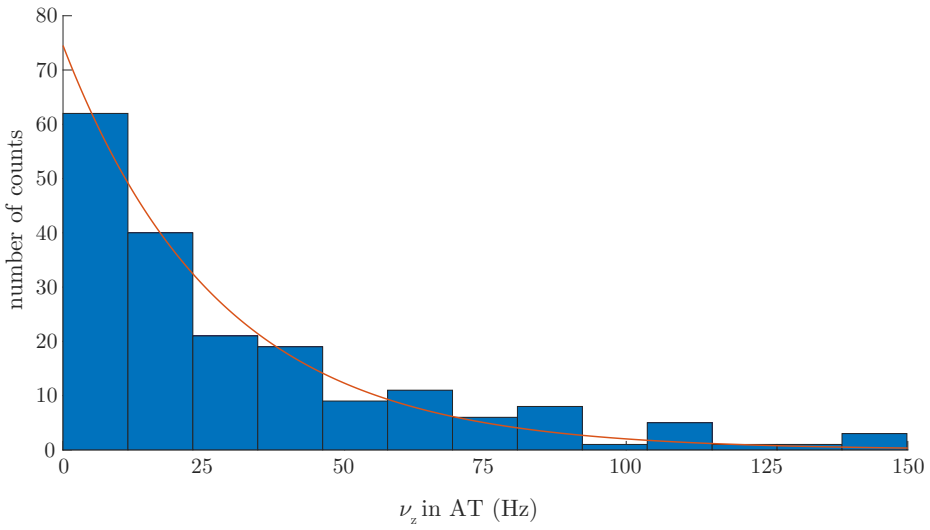

Fig. 6.11: Boltzmann distribution of the ion's axial energy E_z, yielding a temperature of $T_\mathrm{z}^\mathrm{PT} = 5.70(82)\,\mathrm{K}$. The modified cyclotron mode is coupled to the axial mode before the ion is transported to the AT. There the axial frequency shifts as shown here. From this, the axial temperature of the ion can be deduced. For details, see text.

According to equation (3.17), a change in the axial energy E_z would not induce an axial frequency shift assuming that shifts due to electric field imperfections and relativistic mass increase are insignificant in the presence of a large magnetic inhomogeneity B_2. Instead, a modification in the energy of the radial modes causes a shift in the axial frequency. Hence, by measuring the modified cyclotron energy E_+, the axial temperature T_z is extracted by use of equations (4.19) and (4.21).

The modified cyclotron mode is coupled to the axial mode in the precision trap for several cooling time constants, until both modes are thermalised with the detection system. That way the modified cyclotron mode also becomes Boltzmann distributed,

as discussed in section 4.4. Subsequently the ion is adiabatically transported to the analysis trap, where the axial frequency shifts according to equation (3.17):

$$\Delta\nu_z^{AT} = \frac{B_2^{AT}}{B_0^{AT} m 4\pi^2 \nu_z^{AT}} E_+^{AT}. \tag{6.22}$$

Then the ion is adiabatically transported back to the precision trap and the measurement cycle is repeated several times. To finally extract the axial frequency of the ion in the precision trap the adiabatic invariant due to conservation of angular momentum is considered: the magnetic moment of the modified cyclotron mode

$$\mu_+ = \frac{m v_+^2}{2B_0} = \frac{E_+}{B_0} \approx \frac{E_+}{\omega_+}, \tag{6.23}$$

which leads to

$$T_+^{PT} = \frac{\nu_+^{PT}}{\nu_+^{AT}} T_+^{AT}. \tag{6.24}$$

Combining equations (4.21) and (6.24) the axial frequency in the precision trap is determined to be

$$T_z^{PT} = \frac{\nu_z^{PT}}{\nu_+^{AT}} T_+^{AT} = 5.70(82)\,\mathrm{K}. \tag{6.25}$$

Here the uncertainty is estimated by considering both the statistical uncertainty of the measurement as well as the uncertainty of the magnetic bottle in the analysis trap B_2^{AT}.

7 The g-factor of boronlike argon $^{40}Ar^{13+}$

The previously discussed techniques and preparatory measurements have been employed in the course of this thesis in order to measure the g-factor of the $1s^2 2s^2 2p_{1/2}$ ground state of boronlike argon $^{40}Ar^{13+}$. The final result is obtained after two resonances were recorded using the measurement procedure described in section 7.1. The corresponding g-factor resonance that is discussed in section 7.2, is obtained by fitting the data with a Lorentzian line shape using the maximum likelihood estimation. Besides the statistical uncertainty, which is discussed in section 7.2.3, the experimental result largely depends on the systematic uncertainty, which is detailed in section 7.3. Finally, the determination of the g-factor as well as its comparison to the theoretical prediction are discussed in sections 7.4 and 7.5, respectively.

The results obtained here together with a theoretical calculation of the boronlike argon g-factor with an improved precision by collaborating teams is accepted for publication in Phys. Rev. Lett. [27].

7.1 Measurement procedure

After the trap tower has been studied carefully and a single ion was prepared, the g-factor measurement can be implemented. The measurement procedure is fully automated using Matlab and it includes online checks during each measurement cycle which ensure that crucial information (such as, for instance, the spin-state determination) are successfully extracted. The measurement cycle of the g-factor measurement is schematically depicted in Fig. 7.1 and is detailed in the following.

The measurement cycle starts with the ion in the analysis trap (AT). There, the spin state of the boronlike argon $^{40}Ar^{13+}$ ion is determined. That is achieved by, firstly, measuring the ion's axial frequency in the AT twice before mm-wave irradiation. The two measurements are averaged to deduce the axial frequency in the AT. That way changes of the frequency due to the unknown cyclotron energy or the effect of long-term voltage drift can be excluded. Secondly, after mm-wave injection two more consecutive axial frequency measurements take place. By comparing the average axial frequency before and after the mm-wave irradiation, it is established whether a spin flip occurred in the AT or not. If the axial frequency did not shift by more that $170\,\mathrm{mHz}$, the latter being the threshold for the online check for a spin flip which has an expected shift of $312(6)\,\mathrm{mHz}$ (see sections 4.5 and 6.5), the ion is irradiated with mm-waves again and two more measurements of the axial frequency are obtained. In case the spin-flip attempt was successful, the spin state is now determined and the ion is adiabatically transported to the PT where the frequency ratio $\Gamma = \nu_{\mathrm{mmW}}/\nu_{\mathrm{c}}$

is determined. There, the ion's magnetron mode is sideband cooled[1] as described in section 4.4. Then the cryogenic switch is switched on and remains in this state throughout the whole part of the measurement cycle in the PT, to avoid affecting the frequencies when the switch is operated. Then the first axial frequency dip is recorded for an averaging time of $85\,\mathrm{s}$, after which ν_+ is measured by means of the double-dip technique. While the mode coupling for ν_+ determination is on, the ion is irradiated with mm-waves. The frequency of the injected mm-waves is randomly chosen from the predefined frequency range that has been determined using the adiabatic rapid passage technique as described in sections 4.6.4 and 4.6.5 and includes the Larmor frequency[2]. The mm-wave injection is then turned off as well as the mode coupling. Another axial dip measurement takes place, after which the switch is turned off and the ion is transported back to the AT. There, the spin state of the ion is established anew. The spin state before it was transported to the PT and the spin state which the ion had when it arrived back to the AT are compared. Repeating this measurement cycle several times and mapping the spin-flip attemp to the applied mm-wave frequency, a g-factor resonance is obtained.

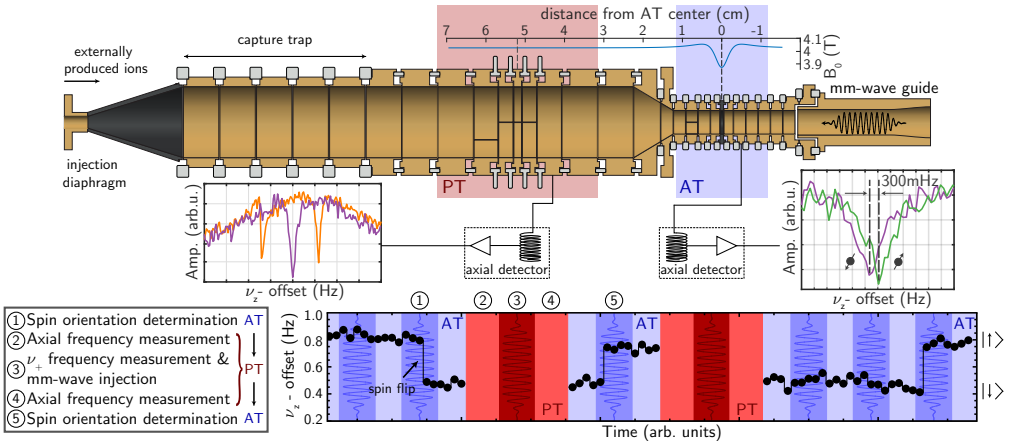

Fig. 7.1: The ALPHATRAP double-trap setup as well as the different measurements taking place within each trap is shown in the upper part of the figure. The frequency ratio $\nu_{\mathrm{mmW}}/\nu_{\mathrm{c}}$ is determined in the precision trap (PT) and the spin state information is obtained within the magnetic bottle of the analysis trap (AT). In the lower part of the figure a schematic representation of the measurement cycle is shown [27].

[1] Unlike in the case of ν_+ and ν_z, the magnetron frequency ν_- is only determined once before the g-factor measurement and once after the measurement is over, which is sufficient for the required precision of ν_- and will be discussed in section 7.3.6.

[2] In fact, the center of the frequency range is adjusted on-line after measuring ν_z and ν_+. The magnetic field is re-calculated using the invariance theorem which is then used to estimate the expected Larmor frequency ν_{L}.

7.2 g-factor resonance

During this measurement campaign two resonances were recorded (Res. A and Res. B) one of which is shown in Fig. 7.2. Each data point that is obtained during the measurement corresponds to either a successful (1) or an unsuccessful (0) spin flip for the corresponding frequency ratio Γ.

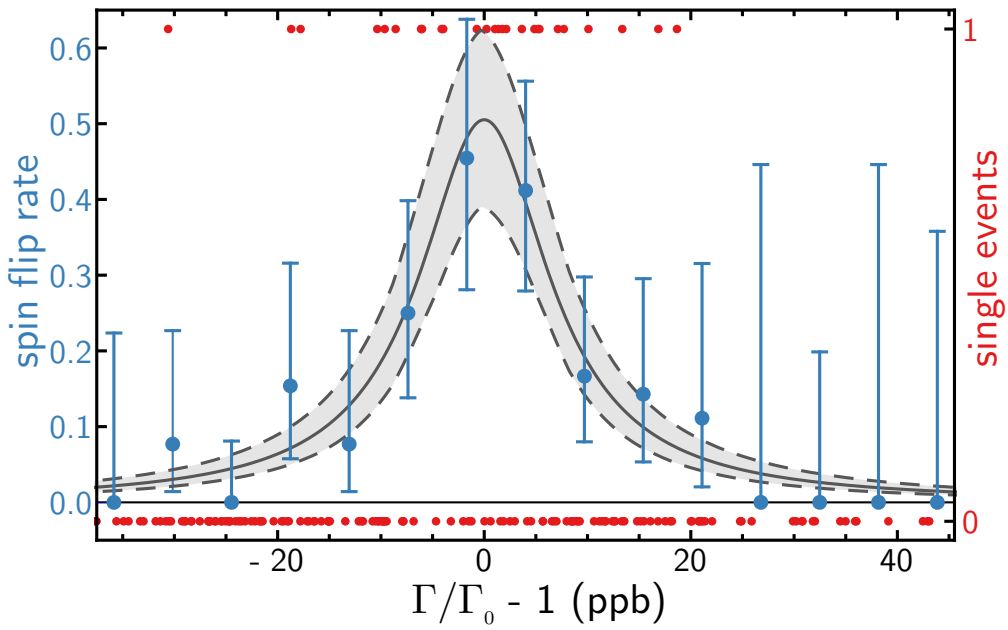

Fig. 7.2: Γ resonance (Res. B), depicting the spin-flip probability as a function of the frequency ratio $\Gamma = \nu_{\mathrm{mmW}}/\nu_{\mathrm{c}}$. The data is fitted with a Lorentzian (solid line) using the maximum likelihood method. The dashed lines indicate the 1-σ confidence interval of the fit. The blue points represent the binned data with binomial error bars and are included in the plot only as a guide for the eye. The red dots represent the single spin-flip events with 1 being a successful spin flip and 0 being an unsuccessful one.

The obtained data is then fitted with a Lorentzian using the maximum-likelihood estimation and is discussed in section 7.2.2.

7.2.1 Line shape of the Γ resonance

The dynamics of the spin under the influence of an oscillating magnetic field has been discussed in detail in section 4.6. There the probability of a spin flip with respect to the mm-wave frequency is given by a Lorentzian probability distribution. Equation (4.56) in terms of Γ is given by

$$P(\Gamma) = \frac{1}{2}\frac{w_0^2}{w_0^2 + (\Gamma_0 - \Gamma)^2}, \tag{7.1}$$

with

$$w_0 = \frac{\omega_\mathrm{R}}{\omega_\mathrm{c}} = \frac{\gamma m B_\mathrm{mmW}}{q B_0}. \tag{7.2}$$

Here w_0 is the half width at half maximum (HWHM) of this distribution which linearly depends on the strength of the driving field. When additionally considering the normally distributed magnetic field fluctuations the resulting probability distribution is described by a Voigt profile, which is a convolution of a Lorentzian and a normal probability distribution. That means that in the limit of low mm-wave power the probability distribution is predominantly Gaussian and the maximum spin-flip rate is well below 0.5. However, during the here presented measurement campaign the mm-wave power was sufficiently large to dominate the magnetic field fluctuations leading to a distribution best described by a Lorentzian with a maximum spin-flip rate close to 0.5. The analysis described below has also been performed using a pseudo-Voigt profile, which confirmed that the contribution of the Gaussian distribution is insignificant.

7.2.2 Maximum-likelihood estimation

The maximum-likelihood estimation (MLE) is advantageous over the least-squares fitting for two crucial reasons. Firstly, no binning of the data is required for the MLE and secondly, the MLE does not assume normally distributed errors.

Performing n measurements for a given Γ the probability of observing k successful events is given by a binomial distribution

$$p = P(\Gamma)^k (1 - P(\Gamma))^{n-k}. \tag{7.3}$$

To obtain the overall probability from the whole data set, we multiply the individual probabilities of the uncorrelated single events. That leads to the maximum likelihood function which is defined as

$$L(\Gamma_0, w_0, R_0) = \prod_i P(\Gamma)^{k_i} (1 - P(\Gamma)^{1-k_i}), \text{ with } k_i = \begin{cases} 1, & \text{spin flip,} \\ 0, & \text{no spin flip,} \end{cases} \tag{7.4}$$

with $P(\Gamma)$ being a Lorentzian distribution, with the maximum spin-flip rate R_0 as a free parameter:

$$P(\Gamma|\Gamma_0, w_0, R_0) = R_0 \frac{w_0^2}{w_0^2 + (\Gamma_0 - \Gamma)^2}, \tag{7.5}$$

with the parameters Γ_0 being the center of the distribution. The maximum likelihood function $L(\Gamma_0, w_0, R_0)$ is not trivial to differentiate[3] therefore it is almost always simplified by using the natural logarithm of L. This yields

[3] The small numbers involved in the product would make the differentiation very challenging numerically.

$$\mathscr{L} = log(L) = \sum ln(P(\Gamma_i)^{k_i} \cdot (1 - P(\Gamma_i))^{1-k_i}), \tag{7.6}$$

which is often referred to as the "log likelihood". For the maximum likelihood estimation we are maximising $\mathscr{L}$ in equation (7.6) with (Γ_i, k_i) being the measured set of single events. Here, k_i is a logical array and it denotes successful spin flips as 1 and the unsuccessful ones with 0 at their corresponding frequency ratios Γ_i. The fitting parameters are the Larmor to cyclotron frequency ratio Γ_0, the HWHM of the distribution w_0 and the maximum spin-flip rate R_0. From the MLE we obtain the optimum values of the fitting parameters for both resonances A and B, which are given in Tab. 7.1. The estimation of the statistical error of those values is discussed in section 7.2.3. In Fig. 7.2 the single-event data is shown in red with respect to $\Gamma/\Gamma_0 - 1$ for Res. B. In the same figure the best fit is plotted with a solid grey line.

Tab. 7.1: Optimised values for the fitting parameters of both recorded resonance obtained via the MLE, with their corresponding relative statistical uncertainties.

parameter	**Res. A**	**Res. B**
Γ_0	1859.082871	1859.082881
$\delta\Gamma/\Gamma_0$(ppb)	$+1.72$ -1.72	$+1.76$ -1.72
w_0	0.000019	0.000019
$\delta w/w_0(\%)$	$+25.8$ -19.2	$+29.4$ -21.0
R_0	0.442	0.505
$\delta R/R_0(\%)$	$+19.6$ -18.4	$+23.4$ -22.2

7.2.3 Statistical uncertainty estimation

To estimate the uncertainty for the three fitting parameters, naively we could vary one parameter while the other two are kept constant at their optimum values. The 1-σ uncertainties are estimated by calculating the value of $\mathscr{L}$ (given in equation 7.6) when it is decreased by 1/2 compared to its optimum value. Similarly, the 2-σ and 3-σ uncertainties correspond to the points where $\mathscr{L}$ is reduced by 2 and 4.5, respectively. That way we can check how the errors behave at a range of 3-σ and probe the symmetry of the error of the fitting parameters as well as exclude the possibility of a local maximum instead of the global maximum.

The results obtained with this approach are plotted in Fig. 7.3, where $\mathscr{L}$ is shown as a function of one of the three fitting parameters individually with the other two kept constant at their respective optimum values.

That approach would have been sufficient if all the parameters were uncorrelated, meaning that the optimum value of every parameter would be independent of the

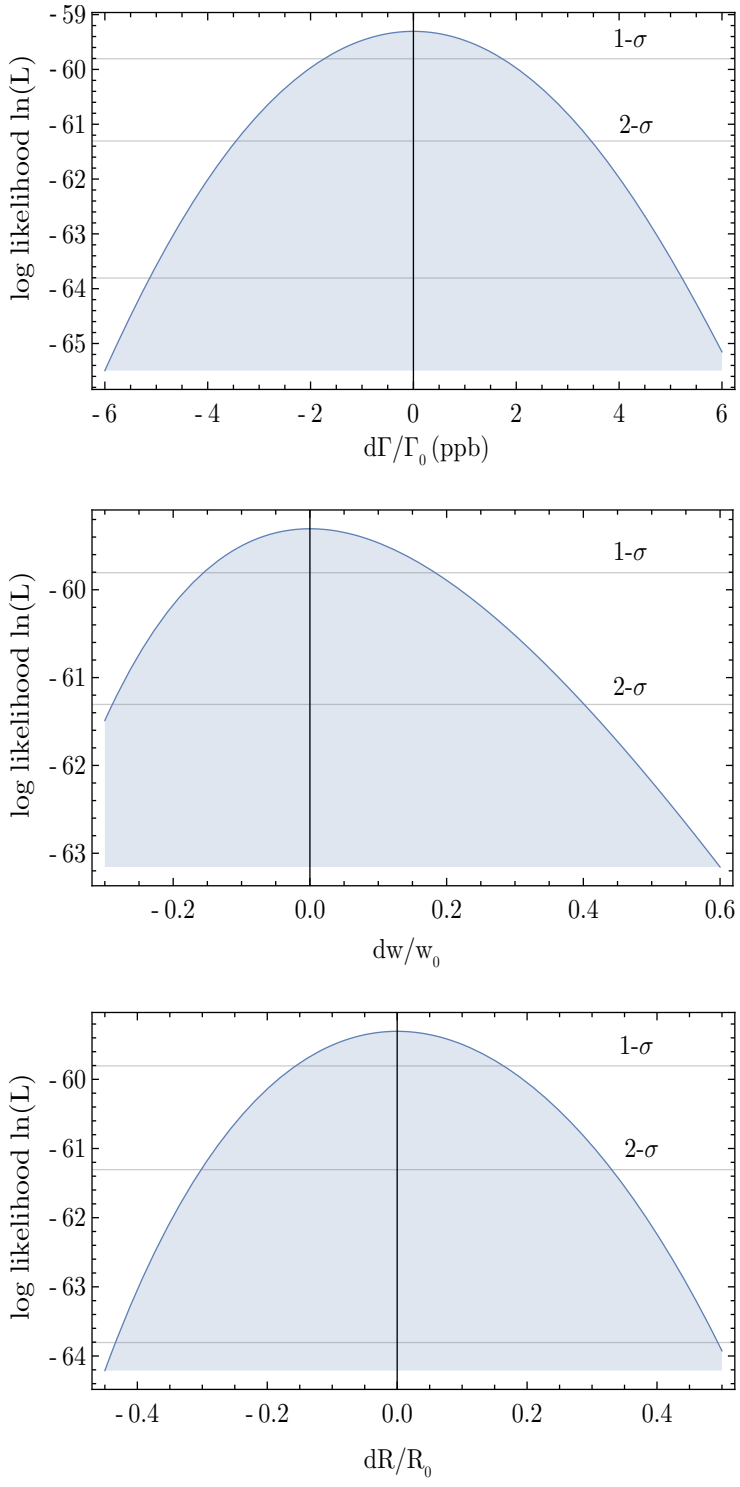

Fig. 7.3: Estimation of the statistical uncertainty of all 3 fitting parameters. Each time, the linear cut of the parameter space is plotted for each of the parameters, while the other 2 remain constant at their optimised values given by the MLE.

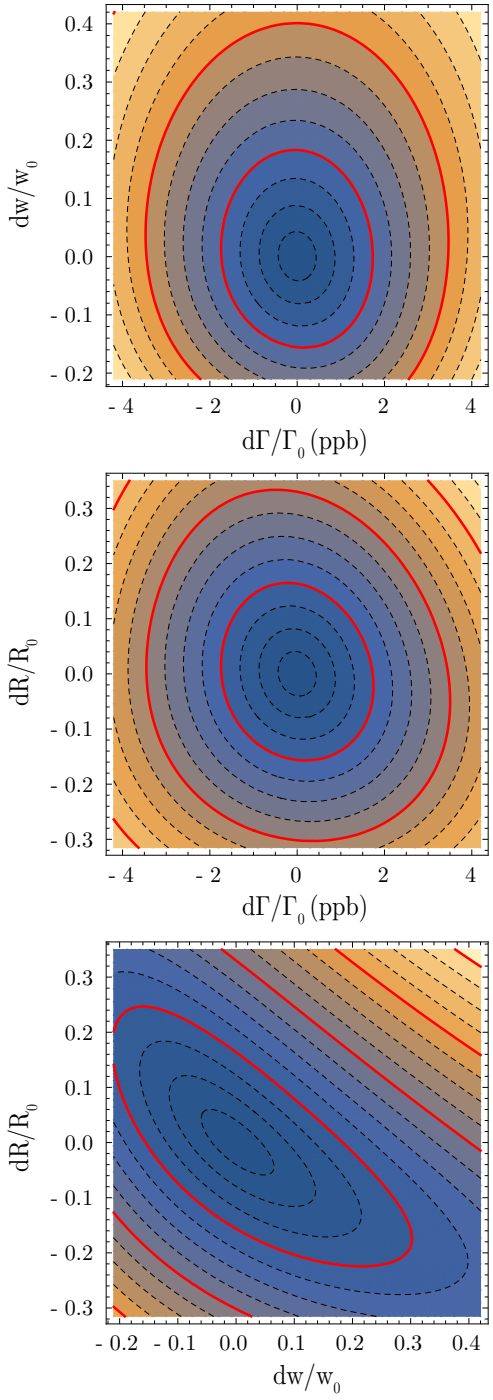

Fig. 7.4: Estimation of the statistical uncertainty of all three fitting parameters. Each subfigure shows $\mathscr{L}$ as a function of 2 fit parameters with 0 corresponding to the optimum values (where $\mathscr{L} = \mathscr{L}_{\max}$). Each contour represents a value of $\mathscr{L}$ with the red contours highlighting the values within the 1-σ, 2-σ and 3-σ ranges. Every one of the three parameters is varied up to the 3-σ range while the other two parameters are re-optimised. That way the existence of close-by secondary minima can be excluded.

other two. This is not the case, as can be seen in the 2D cuts of $\mathscr{L}$ in Fig. 7.4. As can be seen in the dR with respect to dw plot, the shape of the contour lines indicate a coupling of the two parameters. Increasing the value of dR, the optimum value of dw (where $\mathscr{L} = \mathscr{L}_{\max}$) is shifted to a lower value and *vice versa*. Therefore, it is not sufficient to evaluate the uncertainties from the linear cut that was discussed previously.

Instead the entire parameter space fulfilling the condition $\mathscr{L} > \mathscr{L}_{\max} - 0.5$ has to be considered. For this, each of the fitting parameters is varied while the remaining two parameters are re-optimised. This treatment results in a slightly larger, more conservative uncertainty estimation.

The relative statistical uncertainties for all fitting parameters for both resonances are given in Tab. 7.1. The 1-σ confidence interval plotted in Fig. 7.2 is obtained by estimating the worst values for the fitting parameters within the 1-σ range where $\mathscr{L} > \mathscr{L}_{\max} - 0.5$.

In the case of asymmetric errors special care needs to be taken when estimating the final error of the parameter at hand. However, the very small asymmetry in the statistical error of Γ_0 obtained from Res. B is not taken into account in our statistical uncertainty estimation because the error is virtually symmetric. Therefore, the error is treated as symmetric and we select conservatively the larger uncertainty, in this particular case $\delta\Gamma/\Gamma_0 = \pm 1.76(\mathrm{ppb})$.

The weighted average between the two values of Γ_0 for each of the obtained resonances yields

$$\Gamma_0' = 1859.082\,876\,9(23), \tag{7.7}$$

with a relative statistical uncertainty of 1.26×10^{-9}. The value of Γ_0' needs to be corrected for systematic shifts. An important remark concerning the weighted average that results in Γ_0', is that the weights include the systematic uncertainty caused by the axial frequency drift during the Γ measurement. Additionally, the above value has been already corrected for the corresponding systematic shift of this effect. This drift is discussed in section 7.3.1.

7.3 Sources of systematic shifts and uncertainties

In order to obtain the final result for the *g*-factor determination, several effects need to be evaluated that could possibly influence the result. For the current precision level of 10^{-9} combined with our highly optimised setup most of the effects that were in previous experiments prominent now become insignificant. All systematic shifts and their uncertainties are discussed in this section and are summarised in Tab. 7.2.

7.3.1 Drift of the axial potential

During ion transport the potential on the transport electrodes is modified so that the potential trap is adiabatically shifted from one electrode to the next. While

the voltages are applied to the corresponding transport electrode, the rest of the electrode stack is set to $0\,\mathrm{V}$. That means that the nominal trapping voltages in the precision trap are set anew after every time the ion arrives in the trap after being transported from the analysis trap. The slow thermalisation of the power supply after the voltages are set causes a drift in the ion's axial frequency during the measurement. This effect proved to be the most prominent systematic effect during this first measurement campaign of ALPHATRAP, the drift of the axial frequency during the Larmor-to-cyclotron frequency-ratio measurement.

The axial frequency ν_z can't be determined at the same time as the modified cyclotron frequency when the double-dip technique is employed, therefore the effect was estimated independently after the first resonance of the *g*-factor measurement campaign was finished. During this "check" measurement the scheme of a "dip-dip-dip" instead of the "dip-doubledip-dip" was employed. As shown in figure 7.5, the axial frequency drift is not linear and non-negligible. Therefore, in order to determine the axial frequency ν_z during the double-dip time, the observed shift is removed from the actual data. For the first resonance the observed shift with respect to $\tilde{\nu}_{\mathrm{z}2}$ amounts to

$$\tilde{\nu}_{\mathrm{z}1} = -0.2249(94)\,\mathrm{Hz}, \tag{7.8}$$
$$\tilde{\nu}_{\mathrm{z}2} = 0\,\mathrm{Hz}, \tag{7.9}$$
$$\tilde{\nu}_{\mathrm{z}3} = 0.0891(96)\,\mathrm{Hz}, \tag{7.10}$$

where $\tilde{\nu}_{\mathrm{z}1}$, $\tilde{\nu}_{\mathrm{z}2}$ and $\tilde{\nu}_{\mathrm{z}3}$ are the first, second and third axial frequency measurement during the "dip-dip-dip" check measurement. The above shifts with respect to the axial frequency during the Γ determination is removed accordingly from the ν_z data.

Because increasing the waiting time before the PT part of the measurement cycle begins would make the measurement time unacceptably longer, instead the effect was reduced by minimising the time that the voltages of the PT electrodes are set to $0\,\mathrm{V}$. Essentially, while the ion is transported to the analysis trap the voltages in the precision trap are set back to their nominal value decreasing the thermalisation time for the power supply. Employing this technique during the second resonance, Res. B, reduced the shift to

$$\tilde{\nu}_{\mathrm{z}1} = -0.0762(58)\,\mathrm{Hz}, \tag{7.11}$$
$$\tilde{\nu}_{\mathrm{z}2} = 0\,\mathrm{Hz}, \tag{7.12}$$
$$\tilde{\nu}_{\mathrm{z}3} = 0.0145(63)\,\mathrm{Hz}. \tag{7.13}$$

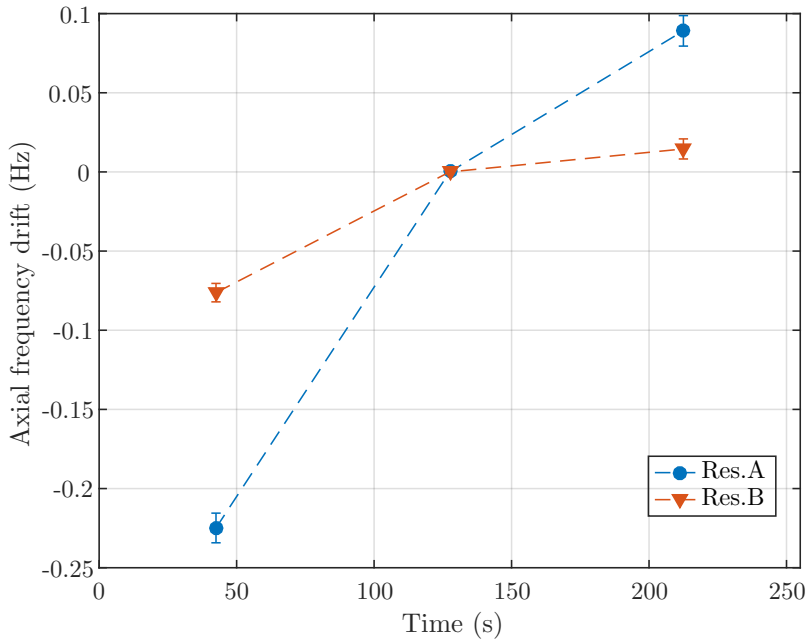

Fig. 7.5: Axial frequency drift during the measurement cycle taking place in the precision trap. The plotted data was obtained during a check measurement after the g-factor data for each of the resonances was obtained. Note that the effect was significantly reduced for Res. B by a more suitable choice of transport voltages. For details see text.

To correct for this drift, we shift the axial frequency before and after the double-dip during the g-factor measurement accordingly as follows:

$$\nu_{\mathrm{z1}} = \nu_{\mathrm{z1}} + \tilde{\nu}_{\mathrm{z1}}, \tag{7.14}$$

$$\nu_{\mathrm{z3}} = \nu_{\mathrm{z3}} - \tilde{\nu}_{\mathrm{z3}}, \tag{7.15}$$

$$\nu_{\mathrm{z2guess}} = \frac{\nu_{\mathrm{z1}} + \nu_{\mathrm{z3}}}{2}, \tag{7.16}$$

where ν_{z2guess} is finally the determined axial frequency ν_{z} during the Γ ratio determination. The uncertainty for this shift is given by the distribution of the data obtained during the "check" measurement for each of the resonances, yielding

$$\delta\nu_{\mathrm{z,ResA}} = 17\,\mathrm{mHz}, \tag{7.17}$$

$$\delta\nu_{\mathrm{z,ResB}} = 7\,\mathrm{mHz}, \tag{7.18}$$

which in the case of employing a measurement technique for ν_+ that measures ν_+ not as a shift with respect to ν_{z} (for instance PnA), would be further reduced by a factor of $\nu_{\mathrm{z}}^2/\nu_+^2$. Since the measurement of the reduced cyclotron frequency is done via the double-dip technique, the above shift has to be taken into account during the estimation of the systematic shift of the free cyclotron frequency. The shift of ν_{c} considering the shift of the axial frequency can be written as

$$\Delta\nu_c \approx \sqrt{\nu_c^2 + 2\Delta\nu_z(\nu_+ + \nu_z)} - \nu_c, \tag{7.19}$$

which amounts to a relative systematic uncertainty of the free cyclotron frequency ν_c:

$$\left(\frac{\delta\nu_c}{\nu_c}\right)_{\mathrm{ResA}} = 8.7 \cdot 10^{-10}, \tag{7.20}$$

$$\left(\frac{\delta\nu_c}{\nu_c}\right)_{\mathrm{ResB}} = 3.6 \cdot 10^{-10}. \tag{7.21}$$

It is important to point out that the frequency shifts given in equations (7.8), (7.10) for Res. A and (7.11), (7.13) for Res. B, have been applied during the data evaluation. That means that the value of Γ_0' given in equation (7.7) has already been shifted for the drift of the axial potential during the frequency ratio measurement.

The resulting systematic uncertainties are different for the two resonances and are included in the weights when determining the value of Γ_0' given in equation (7.7). Those originate from the determination of the effect during this dedicated measurements after each of the resonances was recorded. The corresponding systematic uncertainties due to the axial potential drift are assumed to be uncorrelated because they are dominated by the statistical uncertainty of the measurement.

7.3.2 Image charge shift

The effect of the image charge shift that has been discussed in section 4.2, has been calculated using COMSOL. For this calculation the geometry of the ALPHA-TRAP precision trap has been slightly simplified but it takes into account all existing slits, including all radial ones (i.e. the quarter- and half-split electrodes). From this numerical simulation the linear field gradient of the radial component has been obtained:

$$\mathcal{E}_r = 1964.3(98.2)\,\mu\mathrm{V/m}^2. \tag{7.22}$$

Estimating the shift of ν_+ and ν_- (the shift of ν_z is negligible) using the invariance theorem we obtain the effect on ν_c. From equation (4.14) we thus obtain the relative systematic shift of ν_c for $^{40}Ar^{13+}$:

$$\frac{\Delta\nu_c}{\nu_c} \approx -5.03(25) \times 10^{-11}. \tag{7.23}$$

Note that the shift needs to be added to the measured frequency in order to obtain ν_c without the effect of the image charges.

In the past a semi-analytical model has been used to estimate the effect and it is given in Ref. [60]. There an infinitely long cylinder has been assumed without any split electrodes. Also, a model that accounts for the slits in first order has been presented in Ref. [13]. Furthermore, a numerical calculation has been performed

for calculating the effect using COMSOL for the LIONTRAP experiment [61] which has a similar geometry to that of the ALPHATRAP precision trap.

In order to estimate the uncertainty of the image charge shift in ALPHATRAP, we additionally: (i) calculated the effect using the semi-analytical model and (ii) scaled the numerical results obtained for LIONTRAP to our trap's dimensions. By comparing our numerical result given in equation (7.22) to the two other methods we used for estimating the image-charge effect, we find agreement at the $\sim 1\%$ level. Finally we assign a more conservative uncertainty of $\sim 5\%$ which can be reduced with a more rigorous calculation if necessary.

7.3.3 Relativistic mass increase

The relativistic corrections that has been discussed in section 3.2.3 leads to a shift of both the free-space cyclotron frequency ν_c and the Larmor frequency ν_L but not by the same amount. For a $^{40}Ar^{13+}$ ion the systematic shift of ν_c due to the relativistic mass increase is given by equation (3.20) and it amounts to

$$\frac{\Delta\nu_c}{\nu_c} \approx -0.43(6) \times 10^{-12}. \tag{7.24}$$

The corresponding relative systematic shift of the Larmor frequency due to the relativistic shift of the precession frequency is given by equation (3.21) and it is calculated to be in the order of 10^{-16}.

7.3.4 Line shape of dip-fit

Using the maximum likelihood estimation, the effect of the centre frequency of the resonator on the fitted axial frequency dip of the ion was investigated. The parameters seem to be well behaved. Assuming a shift of the resonator's frequency by 1-σ, that would mean a shift of the fitted axial frequency by $5.2\,\mathrm{mHz}$. That corresponds to a systematic uncertainty of the free cyclotron frequency in the order of

$$\frac{\delta\nu_c}{\nu_c} \simeq 2.7 \cdot 10^{-10}. \tag{7.25}$$

7.3.5 Frequency pulling

The image current shift, or frequency pulling, has been discussed in section 4.2. In Fig. 7.6 the effect is demonstrated for a range of $200\,\mathrm{kHz}$, using equation (4.15). This estimation is based on a set of parameters for the cyclotron resonator that have been experimentally obtained. A more accurate knowledge of those parameters requires additional measurements. For now, and since at this level of precision the effect is negligibly small, we treat the effect as follows: We do not account for a systematic shift, but instead we give a very conservative uncertainty of 25% of the maximum possible shift. That leads to an upper estimation of the systematic uncertainty:

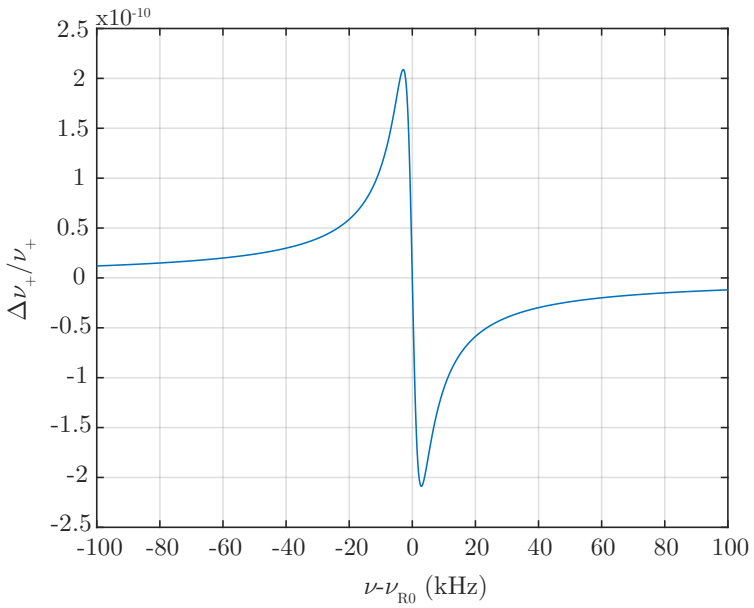

Fig. 7.6: Relative modified cyclotron frequency shift due to the frequency pulling effect caused by the cyclotron resonator with respect to the frequency difference $\nu - \nu_{\mathrm{R0}}$. The shift is zero exactly at resonance and minimised when ν_+ is far from the resonance frequency of the cyclotron resonator.

$$\frac{\delta\nu_{\mathrm{c}}}{\nu_{\mathrm{c}}} \leq 5 \cdot 10^{-11}. \tag{7.26}$$

7.3.6 Magnetron frequency ν_- measurement

During a g-factor measurement campaign the magnetron frequency is typically measured using the double-dip technique once before the resonance is recorded and once after, which is sufficient for the current relative uncertainty of 10^{-9}. According to equation (3.11), for 10^{-9} relative uncertainty ν_- needs to be determined with an uncertainty of $10^{-9}\nu_{\mathrm{c}}^2/\nu_- = 40\,\mathrm{Hz}$. That leads to a relative uncertainty of only 10^{-3}.

The largest shift of the magnetron frequency that was observed before and after resonances A and B was $\Delta\nu_- = 0.13\,\mathrm{Hz}$. That corresponds to a systematic uncertainty of

$$\frac{\delta\nu_{\mathrm{c}}}{\nu_{\mathrm{c}}} = 3.4 \times 10^{-12}. \tag{7.27}$$

7.3.7 Elevated E_+ during the axial frequency measurement

In section 6.6 a source of heating of the modified cyclotron mode has been observed, that has not been conclusively identified yet. Nevertheless, this effect needs to be estimated for the evaluation of the g-factor.

During the double-dip measurement the heating effect on ν_+ is dominated by the stronger cooling effect of the axial detection system. However, that is not the case during the axial frequency measurements before and after the double-dip. During the g-factor measurement an axial temperature of about $6\,\mathrm{K}$ has been obtained. Assuming that this elevated temperature by about $2\,\mathrm{K}$ is caused by this heating effect in the precision trap, we assume as a worst-case-scenario that during one dip measurement the axial temperature increases by $2\,\mathrm{K}$. That means that T_z during the first dip measurement (that is before the double-dip) is increased by about $4\,\mathrm{K}$. For simplicity, in the following the waiting times before and after the double-dip measurement are assumed to be equal which leads to the assumption that the temperature T_z during both dip measurements is elevated by $T_\mathrm{z}^\mathrm{PT} = 4\,\mathrm{K}$.

The corresponding axial frequency shift is given by equations (3.17) and (4.21) as

$$\frac{\Delta\nu_\mathrm{z}}{\nu_\mathrm{z}} = \frac{B_2^\mathrm{PT} k_B T_\mathrm{z}^\mathrm{PT}}{B_0 m (2\pi\nu_\mathrm{z})^2}\left(\frac{\nu_+ - \nu_-}{\nu_\mathrm{z}}\right) \approx 2.5 \times 10^{-11} \tag{7.28}$$

and leads to a relative systematic uncertainty of ν_c of

$$\frac{\delta\nu_\mathrm{c}}{\nu_\mathrm{c}} = 8.2 \times 10^{-13}. \tag{7.29}$$

7.3.8 Electric field anharmonicity

The trapping potential can be tuned to minimise the anharmonicities, as discussed in section 6.2. After the optimisation of the electric field, the applied tuning ratio is known with a 10^{-5} uncertainty. If we assume a detuning of 1×10^{-5}, the leading order anharmonicity that is described by the coefficient C_4 would be $10^{-5} \cdot D_4^\mathrm{comb}$. The corresponding modified cyclotron and axial frequency shift according to equation (3.15) are

$$\frac{\Delta\nu_+}{\nu_+} \approx 3.8 \times 10^{-14}, \tag{7.30}$$

$$\frac{\Delta\nu_\mathrm{z}}{\nu_\mathrm{z}} \approx -1.8 \times 10^{-11}, \tag{7.31}$$

respectively, for a temperature $T_\mathrm{z} = 6\,\mathrm{K}$. Due to the fact that the double-dip is employed for the measurement, the shift of ν_z is taken into account. Using equation (7.19) we obtain

$$\frac{\delta\nu_\mathrm{c}}{\nu_\mathrm{c}} = 5.9 \times 10^{-13}. \tag{7.32}$$

7.3.9 Line shape of the Γ resonance

For the determination of the g-factor, ν_c is measured during the mm-wave irradiation. However, the free-cyclotron frequency is measured at every measurement cycle while

the Larmor frequency is extracted from fitting all the recorded data. That gives rise to a systematic shift of ν_L , because the presence of B_2 is not accounted for in the line shape, which in turn leads to a shift of the obtained Γ.

The line shape that is used to fit the experimental data of the spin-flip probability with respect to the frequency ratio Γ is a Lorentzian. The presence of a magnetic bottle inhomogeneity B_2 combined with the non-vanishing axial temperature of the ion, leads to a slight asymmetry as well as a shift of the maximum of the probability distribution function. The asymmetric line shape has been thoroughly studied for the hydrogenlike oxygen *g*-factor [85, 86] where it was an effect of significant magnitude. However, this effect is negligible for ALPHATRAP, given the low temperatures and the highly reduced B_2^PT of $B_2^\mathrm{PT} = 0.0643(32)\,\mathrm{T/m^2}$.

Following the argument in Refs. [85, 86], a Lorentzian line shape convoluted with a Boltzman distribution due to the B_2 inhomogeneity has been studied. Comparing the results obtained using the slightly asymmetric convoluted line shape to the one obtained using a Lorentzian line shape the relative systematic shift of Γ is estimated. For an axial temperature of $T_\mathrm{z} = 6\,\mathrm{K}$ it amounts to

$$\frac{\delta\Gamma}{\Gamma} = 2.1 \times 10^{-14}. \tag{7.33}$$

7.3.10 Residual magnetic field imperfections

During the frequency-ratio measurement $\Gamma = \nu_\mathrm{L}/\nu_\mathrm{c}$, both frequencies are measured simultaneously. That means that in the presence of inhomogeneities of the magnetic field both frequencies shift, but they shift by almost exactly the same amount. Considering the typically low motional amplitudes of the ion as well as the minimisation of the B_1 and B_2 in our precision trap, the effect of the magnetic field inhomogeneities on both ν_c and ν_L is highly suppressed. However, since both radial modes are thermalised to the axial resonator by means of the double-dip technique, the effect of B_2 on the axial frequency needs to be taken into account.

In the following the shift of Γ due to B_1 is estimated followed by the shift of ν_L and ν_c due to the B_2 inhomogeneity are addressed individually. Finally, the corresponding shift of Γ is estimated.

The first-order inhomogeneity of the magnetic field in the precision trap has been measured to be $B_1 = 2.638(24)\,\mathrm{mT/mm}$ and it has been discussed in section 6.4. That induces a relative shift of both the free-cyclotron frequency ν_c and the Larmor frequency ν_L in the order of 1×10^{-15}, for typical radii and axial temperatures of $r_+ = 2.2\,\mu\mathrm{m}$ and $T_\mathrm{z} = 6\,\mathrm{K}$, respectively.

The residual B_2 in the precision trap has been measured to be $B_2^\mathrm{PT} = 0.0643(32)\,\mathrm{T/m^2}$ (see section 6.3). The corresponding shift of the Larmor frequency is given by equation (3.17), and it amounts to a relative shift of

$$\frac{\Delta\nu_\mathrm{L}}{\nu_\mathrm{L}} \approx 1.11 \times 10^{-12} \tag{7.34}$$

for an axial temperature of $T_z = 6\,\mathrm{K}$. Additionally, the residual magnetic bottle inhomogeneity causes a shift of the free-space cyclotron frequency according to equations (3.17) or equivalently according to Ref. [53], leading to a shift of

$$\frac{\Delta\nu_c}{\nu_c} \approx 1.15 \times 10^{-12} \tag{7.35}$$

with $T_z = 6\,\mathrm{K}$. The corresponding relative shift in the frequency ratio Γ is

$$\frac{\Delta\Gamma}{\Gamma} = 0.02(13) \times 10^{-15}, \tag{7.36}$$

where in the estimation of the uncertainty given in equation (7.36) the uncertainties of T_z, B_2^{AT}, B_2^{PT} and the uncertainty of the axial frequency shift are taken into account.

7.4 Final experimental result for the g-factor of $^{40}Ar^{13+}$

The experimental result Γ_0' in (7.7) needs to be corrected for the systematic effects that have been discussed in the previous section. All the systematic shifts and their corresponding uncertainties are summarised in Tab. 7.2. The corrected final frequency ratio Γ_0 reads:

$$\Gamma_0 = 1859.082\,876\,8(23), \tag{7.37}$$

with the number in the parenthesis being the statistical uncertainty.

Tab. 7.2: Relative systematic corrections $((\Gamma_0 - \Gamma_0')/\Gamma_0')$ and their uncertainties for each of the obtained Γ resonances.

Effect	**Res. A(ppt)**	**Res. B(ppt)**
Drift of axial potential	0(870)	0(360)
Image charge	−50.3(2.5)	
Relativistic mass increase	−0.43(6)	
line shape of dip fit	0(270)	
Frequency pulling ν_+	0(50)	
ν_- measurement	0.0(3.4)	
Elevated E_+ during ν_z meas.	0.00(82)	
Electric field anharmonicity	0.00(60)	
line shape of Γ resonance	0.00(2)	
Magnetic field inhomogeneity	$\ll 10^{-2}$	
Total systematic uncertainty	6.4×10^{-10}	

An important note concerning the systematic shift due to the drift of the axial potential and its uncertainty, should be pointed out once more for clarity. The systematic shift caused by this effect has been considered during data evaluation.

Therefore, Γ_0' in equation (7.7) has already been corrected for the drift of the axial potential. Hence, the systematic shift is given as zero in Tab. 7.2. The systematic uncertainties of the shift are different for the individual resonances. Nevertheless, we quote a total systematic uncertainty which is the result of a weighted average of the systematic uncertainties of the two resonances. The weights used for the average are the same ones that were used for the determination of Γ_0'. These include not only the statistical uncertainty of the resonances but also the systematic uncertainty of the dominant systematic effect, i.e. the drift of the axial potential.

The *g*-factor is determined using

$$g = 2\Gamma_0 \frac{q}{e} \frac{m_\mathrm{e}}{M}, \tag{7.38}$$

with the electron mass $m_\mathrm{e} = 5.485\,799\,090\,70(16) \times 10^{-4}\,\mathrm{u}$ as given by CODATA [87] and $M(^{40}\mathrm{Ar}^{13+}) = 39.955\,255\,154\,5(26)\,\mathrm{u}$. The latter is deduced after correcting the atomic mass $M(^{40}\mathrm{Ar}) = 39.962\,383\,123\,8(24)\,\mathrm{u}$ [88] for the mass and binding energies of the missing electrons [89]. Our experimental result for the *g*-factor when using Γ_0 from equation (7.37) is

$$g_\mathrm{exp} \;=\; 0.663\,648\,456\,29(83)(42)(5), \tag{7.39}$$

where the number in the first bracket represents the statistical uncertainty, the second the systematic uncertainty and the third one accounts for the uncertainty of the electron and the argon atomic[4] masses.

In $^{40}\mathrm{Ar}^{13+}$, mixing of the closely spaced $2p_{1/2}$ and $2p_{3/2}$ levels leads to nonlinear contributions to the Zeeman splitting. However, the quadratic Zeeman shift is identical for both $m = \pm 1/2$ sublevels, therefore, its contribution to the Zeeman splitting vanishes for the ground state. The lowest non-zero nonlinear term is the cubic one, $\sim B^3$. Its contribution to the *g*-factor has been evaluated in Refs. [90, 26] and amounts to $6.0 \times 10^{-11}\ (B/\mathrm{T})^2$. For the magnetic field of $B_0 \approx 4.023\,\mathrm{T}$ of ALPHATRAP this results in an absolute shift of 9.7×10^{-10}. Based on [90, 26] and given our experimental *g*-factor uncertainty, the uncertainty of the cubic Zeeman shift is negligible. Taking the effect into account, we finally obtain for $B_0 = 0\,\mathrm{T}$:

$$g \;=\; 0.663\,648\,455\,32(83)(42)(5). \tag{7.40}$$

This result corresponds to the first high-precision measurement of a boronlike ion's *g*-factor and it is here obtained with a fractional uncertainty of 1.4×10^{-9} for $^{40}\mathrm{Ar}^{13+}$.

[4] The uncertainty of the atomic mass of of argon is dominated by the uncertainties of the binding energies of the removed electrons.

7.5 Comparison with theory

The presented level of precision of the g-factor of $^{40}Ar^{13+}$ gives access, for the first time, to the individual contributions to the g-factor of a boronlike ion. This result is not only sufficient to test the theoretical results for the interelectronic interaction, QED, and nuclear-recoil effects, but also to test the foreseen developments in this field, including higher-order (two-loop and many-electron) QED contributions. The currently available individual contributions to the theoretical g-factor of boronlike argon are given in Tab. 2.1 and are discussed in section 2.3.

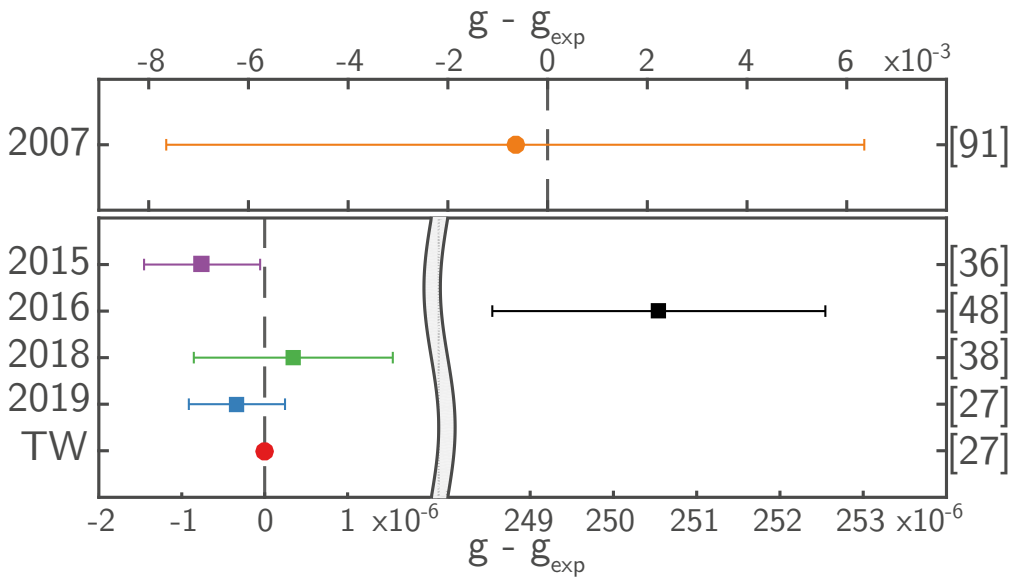

Fig. 7.7: Comparison of the experimental (circles) and theoretical (squares) g-factors obtained in this work (TW) with previously calculated values as well as the previous experimental result with 1×10^{-2} relative uncertainty (note axis label above). The fractional uncertainty of 1.4×10^{-9} of this work's experimental g-factor is not visible in this plot [27].

In collaboration with this experimental campaign theoretical calculations were performed and the results have been also included in the same Letter [27]. Those theoretical calculations improved the one-loop QED contributions by a factor of 3, resulting in a total relative uncertainty of 9×10^{-7}. The agreement between theory and experiment represents one of the most accurate tests of many-electron QED contributions in strong fields, and paves the way towards an independent determination of the fine-structure constant. The current experimental result compared to previous calculations as well as the improved value obtained for [27] can be seen in Fig. 7.7. Our measured value also disproves the theoretical predictions of Marques et al. [48] and Verdebout et al. [49]. The predicted value obtained in the latter is not plotted in Fig. 7.7, as it is given without errorbars.

Comparing the experimental and the theoretical g-factor values demonstrates an excellent agreement at a 10^{-7} level. Further improvement of the theory towards the experimental precision level will constitute a more precise test of the relativistic and QED many-electron effects.

Conclusion and outlook

8

During the course of this thesis a measurement of the ground-state g-factor of boronlike argon $^{40}Ar^{13+}$ has been performed, yielding:

$$g = 0.663\,648\,455\,32(93), \tag{8.1}$$

with a fractional uncertainty of 1.4×10^{-9} [27]. This result provides the most precise g-factor measurement of a five-electron system and gives access to the currently calculated contributions of the electron-electron interaction, QED, and nuclear recoil effects. This level of experimental precision allows to perform the most accurate test of many-electron QED contributions of a boronlike ion in strong fields. It is in excellent agreement with the currently most precise theoretical prediction, which exhibits an uncertainty of 9×10^{-7}. Since our experimental result is almost three orders of magnitude more precise than the current theoretical prediction, it imposes a challenge to theory for an improved uncertainty which would lead to a more sensitive test of the many-electron contributions. Furthermore, this experimental result settles the discrepancy between theoretical predictions [27, 38, 36, 48].

This measurement was made possible after the complete ALPHATRAP apparatus, which is a follow-up to the Mainz g-factor experiment on highly charged ions (HCIs), has been assembled and commissioned. This included the trap tower of ALPHATRAP, which is the central tool of the experiment. This highly optimised high-precision trap tower has been developed, assembled and tested within this thesis and independently of the rest of the setup. After the traps were attached to the experiment, the final commissioning phase took place, of which the results are presented within this thesis.

Coupling the traps to external ion sources by means of a room-temperature UHV ion beam line extends the range of the experiment to virtually any element and charge state up to hydrogenlike lead $^{208}Pb^{81+}$. This is the heaviest HCI that the Heidelberg electron beam ion trap (HD-EBIT) is designed to produce. Despite the external coupling, the vacuum inside the trap chamber is estimated to be in the order of $10^{-17}\,\mathrm{mbar}$ or better. The boronlike argon ion that has been measured in this thesis, has been produced and injected from the Heidelberg compact electron beam ion trap (HC-EBIT). The ion bunch is then transported via the ion beam line to the trap tower, where the ion cloud is captured by fast switching of the potentials of the capture electrodes.

Before the experiment was conduced, the adiabatic rapid passage technique has been implemented in ALPHATRAP. This was achieved by sweeping the magnetic field through the use of a set of Helmholtz coils located externally to the superconducting magnet. This technique allowed to efficiently search for the resonance within a

large frequency range, which was indicated by the theoretical calculation of the g-factor. After the resonance was found, the resonance was recorded twice using the double-dip technique, leading to the determination of the g-factor with ppb precision. The dominant systematic uncertainty during this measurement has been the drift of the applied voltages due to the slow thermalisation of the power supply when the voltages are set after ion transport from one trap to the other. This effect will be mitigated in the near future by using a dedicated voltage source for ion transport. This measurement campaign has been the first one of the ALPHATRAP experiment and signifies the excellent performance of the experiment, and a step towards higher precision and heavier HCI up to $^{208}Pb^{81+}$.

Based on the remarkable performance demonstrated in this first measurement campaign, the precision of g-factor measurements can be improved in the near future by using more sophisticated measurement methods. Namely, implementing the PnA detection scheme [64] for measuring the modified cyclotron frequency can push the uncertainty to the 10^{-11} level in our highly harmonic trap. This technique is currently being implemented [92] and will be used for g-factor measurements of medium-Z HCI. Additionally, measurements with low-Z ions, such as $^{12}C^{5+}$, with an improved precision could lead to a more precise determination of the electron mass.

This highly versatile experimental setup can be used for a wide range of experiments. In fact, a novel laser-spectroscopy measurement scheme has been already implemented on the fine-structure transition of $^{40}Ar^{13+}$ [78, 74]. This new scheme does not rely on fluorescent detection, rather it allows detection of the laser-induced transition by means of the continuous Stern-Gerlach effect.

Furthermore, the ongoing project of sympathetic laser cooling using beryllium ions [77, 74] has the potential to boost the measurement precision by reducing the ion's initial modified cyclotron temperature prior to PnA detection. Also, the lower energies of the modified cyclotron mode, E_+, that can be achieved with sympathetic laser cooling will enable unambiguous spin-flip detection of boronlike lead $^{208}Pb^{77+}$.

After the recommissioning of the HD-EBIT resumes, high-precision g-factor measurements of heavy-Z HCI will be performed where high-precision and the strongest achievable electric fields will combine for the stringent test of QED. In this regime, the anticipated independent determination of the fine structure constant with competitive precision can be realised.

Bibliography

[1]D. Hanneke, S. Fogwell, and G. Gabrielse. “New Measurement of the Electron Magnetic Moment and the Fine Structure Constant”. In: *Phys. Rev. Lett.* 100.12 (2008), p. 120801.

[2]J. Ullmann, Z. Andelkovic, C. Brandau, A. Dax, W. Geithner, C. Geppert, C. Gorges, M. Hammen, V. Hannen, S. Kaufmann, and Others. “High precision hyperfine measurements in Bismuth challenge bound-state strong-field QED”. In: *Nat. Commun.* 8 (2017), p. 15484.

[3]A. Gumberidze, T. Stöhlker, D. Banaś, K. Beckert, P. Beller, H. F. Beyer, F. Bosch, S. Hagmann, C. Kozhuharov, D. Liesen, F. Nolden, X. Ma, P. H. Mokler, M. Steck, D. Sierpowski, and S. Tashenov. “Quantum Electrodynamics in Strong Electric Fields: The Ground-State Lamb Shift in Hydrogenlike Uranium”. In: *Phys. Rev. Lett.* 94 (22 2005), p. 223001.

[4]J. R. Crespo López-Urrutia, P. Beiersdorfer, D. W. Savin, and K. Widmann. “Direct Observation of the Spontaneous Emission of the Hyperfine Transition $F = 4$ to $F = 3$ in Ground State Hydrogenlike $^{165}Ho^{66+}$ in an Electron Beam Ion Trap”. In: *Phys. Rev. Lett.* 77 (5 1996), pp. 826–829.

[5]J. R. Crespo López-Urrutia, P. Beiersdorfer, K. Widmann, B. B. Birkett, A.-M. Mårtensson-Pendrill, and M. G. H. Gustavsson. “Nuclear magnetization distribution radii determined by hyperfine transitions in the $1s$ level of H-like ions $^{185}Re^{74+}$ and $^{187}Re^{74+}$”. In: *Phys. Rev. A* 57 (2 1998), pp. 879–887.

[6]P. Beiersdorfer, S. B. Utter, K. L. Wong, J. R. Crespo López-Urrutia, J. A. Britten, H. Chen, C. L. Harris, R. S. Thoe, D. B. Thorn, E. Träbert, M. G. H. Gustavsson, C. Forssén, and A.-M. Mårtensson-Pendrill. “Hyperfine structure of hydrogenlike thallium isotopes”. In: *Phys. Rev. A* 64 (3 2001), p. 032506.

[7]S. Sturm, F. Köhler, J. Zatorski, A. Wagner, Z. Harman, G. Werth, W. Quint, C. H. Keitel, and K. Blaum. “High-precision measurement of the atomic mass of the electron”. In: *Nature* 506.7489 (2014), pp. 467–470.

[8]F. Köhler, S. Sturm, A. Kracke, G. Werth, W. Quint, and K. Blaum. “The electron mass from g-factor measurements on hydrogen-like carbon $^{12}C^{5+}$”. In: *Journal of Physics B: Atomic, Molecular and Optical Physics* 48.14 (2015), p. 144032.

[9]V. M. Shabaev, D. A. Glazov, N. S. Oreshkina, A. V. Volotka, G. Plunien, H.-J. Kluge, and W. Quint. “g-Factor of Heavy Ions: A New Access to the Fine Structure Constant”. In: *Phys. Rev. Lett.* 96.25 (2006), p. 253002.

[10]A. V. Volotka and G. Plunien. “Nuclear Polarization Study: New Frontiers for Tests of QED in Heavy Highly Charged Ions”. In: *Phys. Rev. Lett.* 113.2 (2014), p. 23002.

[11]V. A. Yerokhin, E. Berseneva, Z. Harman, I. I. Tupitsyn, and C. H. Keitel. "g Factor of Light Ions for an Improved Determination of the Fine-Structure Constant". In: *Phys. Rev. Lett.* 116.10 (2016), p. 100801.

[12]S. Sturm, A. Wagner, B. Schabinger, J. Zatorski, Z. Harman, W. Quint, G. Werth, C. H. Keitel, and K. Blaum. "g Factor of Hydrogenlike $^{28}Si^{13+}$". In: *Phys. Rev. Lett.* 107 (2 2011), p. 023002.

[13]S. Sturm, A. Wagner, M. Kretzschmar, W. Quint, G. Werth, and K. Blaum. "g-factor measurement of hydrogenlike $^{28}Si^{13+}$ as a challenge to QED calculations". In: *Phys. Rev. A* 87 (3 2013), p. 030501.

[14]F. Köhler, K. Blaum, M. Block, S. Chenmarev, S. Eliseev, D. A. Glazov, M. Goncharov, J. Hou, A. Kracke, D. A. Nesterenko, Y. N. Novikov, W. Quint, E. Minaya Ramirez, V. M. Shabaev, S. Sturm, A. V. Volotka, and G. Werth. "Isotope dependence of the Zeeman effect in lithium-like calcium". In: *Nat. Commun.* 7 (2016), p. 10246.

[15]V. M. Shabaev, D. A. Glazov, A. V. Malyshev, and I. I. Tupitsyn. "Recoil Effect on the g Factor of Li-Like Ions". In: *Phys. Rev. Lett.* 119.26 (2017), p. 263001.

[16]A. Wagner, S. Sturm, F. Köhler, D. A. Glazov, A. V. Volotka, G. Plunien, W. Quint, G. Werth, V. M. Shabaev, and K. Blaum. "g Factor of Lithiumlike Silicon $^{28}Si^{11+}$". In: *Phys. Rev. Lett.* 110.3 (2013), p. 33003.

[17]D. A. Glazov, F. Köhler-Langes, A. V. Volotka, F. Heiße, K. Blaum, G. Plunien, W. Quint, V. M. Shabaev, S. Sturm, and G. Werth. In: *arXiv:1903.11609* (2019).

[18]R. H. Parker, C. Yu, W. Zhong, B. Estey, and H. Müller. "Measurement of the fine-structure constant as a test of the Standard Model". In: *Science (80-.).* 360.6385 (2018), pp. 191–195.

[19]P. A. M. Dirac. "The quantum theory of the electron". In: *Proc. R. Soc. Lond. A* 117.778 (1928), pp. 610–624.

[20]J. Schwinger. "On quantum-electrodynamics and the magnetic moment of the electron". In: *Phys. Rev.* 73.4 (1948), p. 416.

[21]T. Aoyama, M. Hayakawa, T. Kinoshita, and M. Nio. "Tenth-order QED contribution to the electron g- 2 and an improved value of the fine structure constant". In: *Phys. Rev. Lett.* 109.11 (2012), p. 111807.

[22]S. Laporta. "High-precision calculation of the 4-loop contribution to the electron g-2 in QED". In: *Phys. Lett. B* 772 (2017), pp. 232–238.

[23]G. Breit. "The magnetic moment of the electron". In: *Nature* 122.3078 (1928), p. 649.

[24]V. A. Yerokhin, P. Indelicato, and V. M. Shabaev. "Evaluation of the self-energy correction to the g factor of S states in H-like ions". In: *Phys. Rev. A* 69 (5 2004), p. 052503.

[25]A. V. Volotka, D. A. Glazov, V. M. Shabaev, I. I. Tupitsyn, and G. Plunien. "Many-Electron QED Corrections to the g Factor of Lithiumlike Ions". In: *Phys. Rev. Lett.* 112 (25 2014), p. 253004.

[26]A. S. Varentsova, V. A. Agababaev, D. A. Glazov, A. M. Volchkova, A. V. Volotka, V. M. Shabaev, and G. Plunien. "Interelectronic-interaction contribution to the nonlinear Zeeman effect in boronlike ions". In: *Phys. Rev. A* 97.4 (2018), p. 43402.

[27]I. Arapoglou, A. Egl, M. Hocker, T. Sailer, B. Tu, A. Weigel, R. Wolf, H. Cakir, V. A. Yerokhin, N. S. Oreshkina, V. A. Agababaev, A. V. Volotka, D. V. Zinenko, D. A. Glazov, Z. Harman, C. H. Keitel, S. Sturm, and K. Blaum. "g factor of boronlike argon $^{40}Ar^{13+}$". In: *Phys. Rev. Lett.* In print (2019).

[28]H. Cakir, V. A. Yerokhin, et al. In: To be Published (2019).

[29]S. A. Zapryagaev. In: *Opt. Spectrosc.* 47 (1979), p. 9.

[30]W. Quint and M. Vogel, eds. *Fundamental Physics in Particle Traps*. Vol. 395. Springer, 2014.

[31]V. M. Shabaev, D. A. Glazov, M. B. Shabaeva, V. A. Yerokhin, G. Plunien, and G. Soff. "g factor of high-Z lithiumlike ions". In: *Phys. Rev. A* 65.6 (2002), p. 62104.

[32]V. M. Shabaev, I. I. Tupitsyn, V. A. Yerokhin, G. Plunien, and G. Soff. "Dual Kinetic Balance Approach to Basis-Set Expansions for the Dirac Equation". In: *Phys. Rev. Lett.* 93.13 (2004), p. 130405.

[33]B. Sikora, H. Cakir, N. Michel, V. Debierre, N. S. Oreshkina, N. A. Belov, V. A. Yerokhin, C. H. Keitel, and Z. Harman. "Improving the accuracy of the muon mass and magnetic moment anomaly via the bound-muon g factor". In: *Phys. Rev. D* 97.11 (2018), p. 111301.

[34]D. A. Glazov, V. M. Shabaev, I. I. Tupitsyn, A. V. Volotka, V. A. Yerokhin, G. Plunien, and G. Soff. "Relativistic and QED corrections to the g factor of Li-like ions". In: *Phys. Rev. A* 70.6 (2004), p. 62104.

[35]D. A. Glazov, A. V. Volotka, A. A. Schepetnov, M. M. Sokolov, V. M. Shabaev, I. I. Tupitsyn, and G. Plunien. "g factor of boron-like ions: ground and excited states". In: *Phys. Scr.* 2013.T156 (2013), p. 14014.

[36]A. A. Shchepetnov, D. A. Glazov, A. V. Volotka, V. M. Shabaev, I. I. Tupitsyn, and G. Plunien. "Nuclear recoil correction to the g factor of boron-like argon". In: *J. Phys. Conf. Ser.* 583.1 (2015), p. 12001.

[37]D. E. Maison, L. V. Skripnikov, and D. A. Glazov. "Many-body study of the g factor in boronlike argon". In: *Phys. Rev. A* 99 (4 2019), p. 042506.

[38]V. A. Agababaev, D. A. Glazov, A. V. Volotka, D. V. Zinenko, V. M. Shabaev, and G. Plunien. "Ground-state g factor of middle-Z boronlike ions". In: *J. Phys. Conf. Ser.* 1138.1 (2018), p. 012003.

[39]V. A. Yerokhin and U. D. Jentschura. "Electron Self-Energy in the Presence of a Magnetic Field: Hyperfine Splitting and g Factor". In: *Phys. Rev. Lett.* 100.16 (2008), p. 163001.

[40]V. A. Yerokhin and U. D. Jentschura. "Self-energy correction to the hyperfine splitting and the electron g factor in hydrogenlike ions". In: *Phys. Rev. A* 81.1 (2010), p. 12502.

[41]V. A. Yerokhin, C. H. Keitel, and Z. Harman. "Nuclear-size self-energy and vacuum-polarization corrections to the bound-electron g factor". In: *J. Phys. B* 46.24 (2013), p. 245002.

[42]D. A. Glazov, A. V. Volotka, V. M. Shabaev, I. I. Tupitsyn, and G. Plunien. "Screened QED corrections to the g factor of Li-like ions". In: *Phys. Lett. A* 357.4 (2006), p. 330.

[43]A. V. Volotka, D. A. Glazov, G. Plunien, V. M. Shabaev, and I. I. Tupitsyn. “Radiative corrections to the magnetic-dipole transition amplitude in B-like ions”. In: *Eur. Phys. J. D* 38.2 (2006), p. 293.

[44]F. T. Köhler. “Bound-Electron g-Factor Measurements for the Determination of the Electron Mass and Isotope Shifts in Highly Charged Ions”. PhD thesis. Ruprecht-Karls-Universität Heidelberg, 2015.

[45]D. A. Glazov, A. V. Malyshev, V. M. Shabaev, and I. I. Tupitsyn. “Nuclear Recoil Effect on the g Factor of Middle-Z Boronlike Ions”. In: *Opt. Spectrosc.* 124.4 (2018), pp. 457–461.

[46]D. A. Glazov and V. M. Shabaev. “Finite nuclear size correction to the bound-electron g factor in a hydrogenlike atom”. In: *Physics Letters A* 297.5 (2002), pp. 408 –411.

[47]H. Grotch and R. Kashuba. “Magnetic Interactions of One-Electron Atoms and of Positronium”. In: *Phys. Rev. A* 7.1 (1973), pp. 78–84.

[48]J. P. Marques, P. Indelicato, F. Parente, J. M. Sampaio, and J. P. Santos. “Ground-state Landé g factors for selected ions along the boron isoelectronic sequence”. In: *Phys. Rev. A* 94.4 (2016), p. 42504.

[49]S. Verdebout, C. Nazé, P. Jönsson, P. Rynkun, M. Godefroid, and G. Gaigalas. “Hyperfine structures and Landé g_J-factors for n=2 states in beryllium-, boron-, carbon-, and nitrogen-like ions from relativistic configuration interaction calculations”. In: *At. Data Nucl. Data Tables* 100.5 (2014), pp. 1111–1155.

[50]L. S. Brown and G. Gabrielse. “Geonium theory: Physics of a single electron or ion in a Penning trap”. In: *Rev. Mod. Phys.* 58.1 (1986), pp. 233–311.

[51]L. S. Brown and G. Gabrielse. “Precision spectroscopy of a charged particle in an imperfect Penning trap”. In: *Phys. Rev. A* 25.4 (1982), pp. 2423–2425.

[52]G. Gabrielse and F. C. Mackintosh. “Cylindrical Penning traps with orthogonalized anharmonicity compensation”. In: *Int. J. Mass Spectrom. Ion Process.* 57.1 (1984), pp. 1–17.

[53]J. Ketter, T. Eronen, M. Höcker, S. Streubel, and K. Blaum. “First-order perturbative calculation of the frequency-shifts caused by static cylindrically-symmetric electric and magnetic imperfections of a Penning trap”. In: *Int. J. Mass Spectrom.* 358 (2014), pp. 1–16.

[54]J. Ketter, T. Eronen, M. Höcker, M. Schuh, S. Streubel, and K. Blaum. “Classical calculation of relativistic frequency-shifts in an ideal Penning trap”. In: *Int. J. Mass Spectrom.* 361 (2014), pp. 34–40.

[55]S. Sturm. “The g-factor of the electron bound in $^{28}Si^{13+}$: The most stringent test of bound-state quantum”. PhD thesis. Johannes Gutenberg-Universität Mainz, 2011.

[56]F. Heiße et al. “The LIONTRAP experiment - A new high-precision mass spectrometer for light ions”. In: (2019). In preparation.

[57]F. Heiße, F. Köhler-Langes, S. Rau, J. Hou, S. Junck, A. Kracke, A. Mooser, W. Quint, S. Ulmer, G. Werth, and Others. “High-Precision Measurement of the Proton’s Atomic Mass”. In: *Phys. Rev. Lett.* 119.3 (2017), p. 33001.

[58]S. Sturm, I. Arapoglou, A. Egl, M. Höcker, S. Kraemer, T. Sailer, B. Tu, A. Weigel, R. Wolf, J. Crespo López-Urrutia, and K. Blaum. “The ALPHATRAP experiment”. In: *Eur. Phys. J. Spec. Top.* 227.13 (2019), pp. 1425–1491.

[59]A. Weigel. “Detection Electronics Design and First Observation of Bound-Electron Spin Transitions at the ALPHATRAP g-Factor Experiment”. PhD thesis. Ruprecht-Karls-Universität Heidelberg, 2019.

[60]H. Häffner. “Präzisionsmessung des magnetischen Moments des Elektrons in wasserstoffähnlichem Kohlenstoff.” PhD thesis. Johannes Gutenberg-Universität Mainz, 2000.

[61]M. Schuh et al. “Image charge shift in high-precision Penning traps”. In: *Submitted* (2019).

[62]V. Natarajan. “Penning trap mass spectrometry at 0.1 ppb”. PhD Thesis. Massachusetts Institute of Technology, 1993.

[63]E. A. Cornell, R. M. Weisskoff, K. R. Boyce, and D. E. Pritchard. “Mode coupling in a Penning trap”. In: *Phys. Rev. A* 41.1 (1990), p. 312.

[64]S. Sturm, A. Wagner, B. Schabinger, and K. Blaum. “Phase-sensitive cyclotron frequency measurements at ultralow energies”. In: *Phys. Rev. Lett.* 107.14 (2011), p. 143003.

[65]W. Gerlach and O. Stern. “Der experimentelle nachweis der richtungsquantelung im magnetfeld”. In: *Zeitschrift für Phys.* 9.1 (1922), pp. 349–352.

[66]H. Dehmelt. “Continuous Stern-Gerlach effect: principle and idealized apparatus”. In: *Proc. Natl. Acad. Sci.* 83.8 (1986), pp. 2291–2294.

[67]L. D. Landau. In: *Phys. Z. Sowjetunion* 2 (1932), p. 46.

[68]C. Zener. “Non-Adiabatic Crossing of Energy Levels”. In: *Proc. R. Soc. London. Ser. A, Contain. Pap. a Math. Phys. Character* 137.833 (1932), pp. 696–702.

[69]P. Hannaford, D. T. Pegg, and G. W. Series. “Analytical expressions for the Bloch-Siegert shift”. In: *J. Phys. B At. Mol. Phys.* 6.8 (1973), pp. L222–L225.

[70]F. Ahmad and R. K. Bullough. “Theory of the Bloch-Siegert shift”. In: *J. Phys. B At. Mol. Phys.* 7.9 (1974), pp. L275–L280.

[71]Ensinger. *TECAPEEK ELS nanoblack*. Version AC. Ensinger GmbH. Rudolf-Diesel Str. 8, 71154 Nufringen Germany, 2017.

[72]K. A. Farrar. “Calculation of the electrostatic potential field for an open-endcap cylindrical penning trap”. In: *Nucl. Instruments Methods Phys. Res. Sect. A Accel. Spectrometers, Detect. Assoc. Equip.* 485.3 (2002), pp. 780–796.

[73]VACUUMSCHMELZE. *VACOFLUX50*. VACUUMSCHMELZE GmbH. Grüner Weg 37 D-63450 Hanau Germany, 2017.

[74]A. Egl. In preparation. PhD thesis. Ruprecht-Karls-Universität Heidelberg.

[75]C. Böhm, S. Sturm, A. Rischka, A. Dörr, S. Eliseev, M. Goncharov, M. Höcker, J. Ketter, F. Köhler, D. Marschall, and Others. “An ultra-stable voltage source for precision Penning-trap experiments”. In: *Nucl. Instruments Methods Phys. Res. Sect. A Accel. Spectrometers, Detect. Assoc. Equip.* 828 (2016), pp. 125–131.

[76]*UM - Series, Multichannel Precision Voltage Source*. Manual_UM_. Stahl-Electronics. Kellerweg 23 67582 Mettenheim, Germany, 2016.

[77]S. Kraemer. “Towards Laser Cooling of Beryllium Ions at the ALPHATRAP Experiment”. MA thesis. Ruprecht-Karls-Universität Heidelberg, 2017.

[78]A. Egl, I. Arapoglou, M. Höcker, K. König, T. Ratajczyk, T. Sailer, B. Tu, A. Weigel, K. Blaum, W. Nörtershäuser, and S. Sturm. “Application of the continuous Stern-Gerlach effect for laser spectroscopy of the $^{40}Ar^{13+}$ fine structure in a Penning trap”. In: *Phys. Rev. Lett.* Submitted (2019).

[79]T. Steinsberger. “Microwave injection for the ALPHATRAP experiment and developments of the multi-reflection time-of-flight technique of the ISOLTRAP experiment”. MA thesis. Ruprecht-Karls-Universität Heidelberg, 2018.

[80]C. Carlberg, H. Borgenstrand, G. Rouleau, R. Schuch, F. Söderberg, I. Bergström, R. Jertz, T. Schwarz, J. Stein, G. Bollen, and Others. “The SMILETRAP facility”. In: *Phys. Scr.* 1995.T59 (1995), p. 196.

[81]J. R. C. López-Urrutia, J. Braun, G. Brenner, H. Bruhns, C. Dimopoulou, I. N. Draganić, D. Fischer, A. J. G. Martínez, A. Lapierre, V. Mironov, et al. “Progress at the Heidelberg EBIT”. In: *J. Phys. Conf. Ser.* Vol. 2. 1. IOP Publishing. 2004, p. 42.

[82]P. Micke, S. Kühn, L. Buchauer, J. R. Harries, T. M. Bücking, K. Blaum, A. Cieluch, A. Egl, D. Hollain, S. Kraemer, T. Pfeifer, P. O. Schmidt, R. X. Schüssler, C. Schweiger, T. Stöhlker, S. Sturm, R. N. Wolf, S. Bernitt, and J. R. Crespo López-Urrutia. “The Heidelberg compact electron beam ion traps”. In: *Rev. Sci. Instrum.* 89.6 (2018), p. 63109.

[83]T. Sailer. “A Laser Ion Source for the ALPHATRAP Experiment”. MA thesis. Ruprecht-Karls-Universität Heidelberg, 2017.

[84]J. Repp. “The setup of the high-precision Penning trap mass spectrometer PENTATRAP and first production studies of highly charged ions.” PhD thesis. Ruprecht-Karls-Universität Heidelberg, 2012.

[85]J. Verdú. “Ultrapräzise Messung des elektronischen g-Faktors in wasserstoffähnlichem Sauerstoff”. PhD thesis. Johannes Gutenberg-Universität Mainz, 2004.

[86]J. Verdú, S. Djekić, S. Stahl, T. Valenzuela, M. Vogel, G. Werth, T. Beier, H.-J. Kluge, and W. Quint. “Electronic g Factor of Hydrogenlike Oxygen”. In: *Phys. Rev. Lett.* 92.9 (2004), p. 93002.

[87]P. J. Mohr, D. B. Newell, and B. N. Taylor. “CODATA recommended values of the fundamental physical constants: 2014”. In: *Rev. Mod. Phys.* 88.3 (2016), p. 35009.

[88]P. J. Mohr, D. B. Newell, B. N. Taylor, and E. Tiesinga. “Data and analysis for the CODATA 2017 special fundamental constants adjustment”. In: *Metrologia* 55.1 (2018), p. 125.

[89]A. Kramida, Y. Ralchenko, J. Reader, and NIST ASD Team. *NIST Atomic Spectra Database (ver. 5.6.1)*. NIST Atomic Spectra Database (ver. 5.6.1), [Online]. Available: https://physics.nist.gov/asd [2018, December 19]. National Institute of Standards and Technology, Gaithersburg, MD. 2018.

[90]D. von Lindenfels, M. Wiesel, D. A. Glazov, A. V. Volotka, M. M. Sokolov, V. M. Shabaev, G. Plunien, W. Quint, G. Birkl, A. Martin, and M. Vogel. “Experimental access to higher-order Zeeman effects by precision spectroscopy of highly charged ions in a Penning trap”. In: *Phys. Rev. A* 87 (2 2013), p. 023412.

[91]R. Soria Orts, J. R. Crespo López-Urrutia, H. Bruhns, A. J. González Martinez, Z. Harman, U. D. Jentschura, C. H. Keitel, A. Lapierre, H. Tawara, I. I. Tupitsyn, J. Ullrich, and A. V. Volotka. “Zeeman splitting and g factor of the $1s^22s^22p\ ^2P_{3/2}$ and $^2P_{1/2}$ levels in Ar^{13+}”. In: *Phys. Rev. A* 76.5 (2007), p. 52501.

[92]T. Sailer. In preparation. PhD thesis. Ruprecht-Karls-Universität Heidelberg.

Publications

During the course of this thesis the following articles have been published, accepted for publication and submitted for publication, respectively:

- S. Sturm, I. Arapoglou, A. Egl, M. Höcker, S. Kraemer, T. Sailer, B. Tu, A. Weigel, R. Wolf, J. C. López-Urrutia, and K. Blaum. “The ALPHATRAP experiment”. In: Eur. Phys. J. Spec. Top. 227.13 (2019), pp. 1425–1491. (Ref. [58])
- I. Arapoglou, A. Egl, M. Hocker, T. Sailer, B. Tu, A. Weigel, R. Wolf, H. Cakir, V. A. Yerokhin, N. S. Oreshkina, V. A. Agababaev, A. V. Volotka, D. V. Zinenko, D. A. Glazov, Z. Harman, C. H. Keitel, S. Sturm, and K. Blaum. “g-factor of boronlike argon $^{40}Ar^{13+}$”. In: Phys. Rev. Lett. In print (2019). (Ref. [27])
- A. Egl, I. Arapoglou, M. Höcker, K. König, T. Ratajczyk, T. Sailer, B. Tu, A. Weigel, K. Blaum, W. Nörtershäuser, and S. Sturm. “Application of the continuous Stern-Gerlach effect for laser spectroscopy of the $^{40}Ar^{13+}$ fine structure in a Penning trap”. In: Phys. Rev. Lett. Submitted (2019). (Ref. [78])

Acknowledgement

This work would not have been possible without the help and support from many people. I will try and find the words to express my gratitude.

First and foremost, I want to thank my thesis advisor Prof. Dr. Klaus Blaum. Klaus, it has been an honour for me to carry out my PhD under your supervision. It was truly a pleasure working with you on such an exciting project. Thank you for being tirelessly available anytime I needed your help. You have always been willing to provide valuable advice. Your pleasant personality and accessibility made this journey easier. Thank you for being an excellent "doctor-father" for the past four years.

I also want to thank Dr. Sven Sturm, my second advisor and the group leader of ALPHATRAP. Sven, your remarkable passion for physics and your immense knowledge on the subject are inspirational. Your insights and countless ideas lead to four years of intense work that was totally worth it. I learned so much from you and I deeply appreciate the numerous conversations we had about such a fascinating experiment. You were always there for me and supported me not only scientifically but also on personal matters, and also for that you have my gratitude.

Furthermore, I want to thank Prof. Dr. Selim Jochim the second reviewer of this thesis. Selim, thank you for undertaking the task of reviewing my work. I really hope you enjoyed reading it as much as I enjoyed writing it.

Also, I want to thank Dr. Zoltán Harman. Zoltán, thank you for always finding the time to answer my questions. Your endless patience in explaining complicated theoretical calculations to me, helped me learn a lot about QED.

I would like to thank the ALPHATRAP postdocs, Robert Wolf, Martin Höcker and Bingsheng Tu. Robert, working with you the first years of my PhD was valuable and a lot of fun! It has been a real joy being your student and your friend. Martin, thank you for all your MATLAB advice and lab work! Bingsheng, thank you for always being available to answer my questions, it was a pleasure working with you.

Also, I want to say thank you to:

Andreas Weigel, my first office and lab mate in ALPHATRAP. Andi, thank you for all the joyful working hours we spent together! Your kindness and understanding surely made even tough days in the lab easier. Thank you for answering all my questions about the detection system and for all your creative solutions in the lab. But above all, thank you for the support and of course all the good laughs.

Alexander Egl and Tim Sailer, the next-in-line PhD students. Thank you guys for all the hard work in the lab. Our fruitful discussions and intense lab hours made all of it happen. Handing over the trap to your capable hands certainly will lead to further exciting results.

The rest of the Penning-trappers of the Blaum division. Thank you all for the nice lunch-time discussions! Every single one of you was always helpful when I needed some help. It was a pleasure learning about your experiments.

My far-away friends. Branka Vanovac and Camila de Conto, our paths crossed years ago in a very unlikely way. All the good times we spent together are unforgettable, and more of it is coming soon. Thank you for your support and encouragement! Nefeli Sotiropoulou, Rosmarie Anastasiadi, Sofia Kostaki and Dimitra Mazaraki, thank you for your friendship over the years.

My friends Christina Dimitropoulou and Christos Nikolaou. All these years I know you, made me who I am today. The countless priceless moments I spent with you cannot be expressed in words. Your unconditional love and support means the world to me and I am truly grateful to have you in my life. I can't wait for more adventurous times with you! We might be geographically apart but you have always been my reference point. You are more than friends to me, you are family.

Bastian, thank you for being you. You have made this hard-working period of time so much easier for me. You make my days brighter. Your thoughtfulness and understanding leave me speechless...So thank you with all my heart! For bearing with me all this time, for all your love and support.

Τους γονείς μου, Κατερίνα και Χρήστο Αράπογλου. Η απεριόριστη αγάπη και η υποστήριξη που μου προσφερατε όλα αυτά τα χρόνια, μου επέτρεψε να είμαι εκεί που είμαι σημερα. Πάντα *πιστεύατε σε μένα και ενθαρρύνατε κάθε μου βήμα. Χωρίς εσάς το μονοπάτι θα ήταν σίγουρα πιο δύσκολο, και για αυτό σας ευχαριστώ. Αυτή η διατριβή είναι για σας.*